RED-EMITTING III-NITRIDE SELF-ASSEMBLED QUANTUM DOT LASERS

by

Thomas A. Frost

A dissertation submitted in partial fulfillment
of the requirements for the degree of
Doctor of Philosophy
(Electrical Engineering)
in The University of Michigan
2016

Doctoral Committee:

Professor Pallab K. Bhattacharya, Chair
Professor Rachel S. Goldman
Associate Professor Pei-Cheng Ku
Professor Jamie D. Phillips

© Thomas A. Frost 2016

To my parents

ACKNOWLEDGMENTS

As I reflect back on the seven years that I've spent in Ann Arbor, I think most about the people I've met and how they've all contributed to my success here. I would like to first thank my doctoral advisor, Professor Pallab Bhattacharya, for his unwavering support and motivation through this whole process from when I started as a summer student following the freshmen year of undergrad through the completion of my Ph. D. work. He has given me the opportunity to work on cutting edge research and challenging projects and has supported me in executing them, and for that I am eternally grateful. His dedication to those around him, determination for accomplishing his goals, and willingness to share his immense knowledge are attributes that I strive to follow.

I would also like to thank my committee members, Prof. Jamie Phillips, Prof. Pei-Cheng Ku, and Prof. Rachel Goldman for their time, valuable comments, and insightful discussions. In particular, I'd like to thank Prof. Goldman for her collaboration in understanding the material through scanning tunneling microscopy. I would like to thank Prof. Joanna Mirecki-Millunchik for her valuable comments and discussions. I am also grateful Prof. Shun Lien Chuang and Prof. John Dallesasse at the University of Illinois, Urbana-Champaign for their help in modeling and discussions.

I am grateful for the help of our current and former group members: Dr. Debashish Basu, Dr. Wei Guo, Dr. Meng Zhang, Dr. Junseok Heo, Dr. Chi-Sen Lee, Dr. Hyun Kum, Dr. Ayan Das, Dr. Sishir Bhowmick, Dr. Animesh Banerjee, Dr. Shafat

Jahangir, Dr. Saniya Deshpande, Md. Zunaid Baten, Arnab Hazari, Aniruddha Bhattacharya and Anthony Aiello. In particular, I am grateful to Dr. Chi-Sen Lee who introduced me to the research and who I worked with throughout my undergrad after that fateful summer. He is immensely knowledgeable and helpful even to this day long after he graduated. I am also grateful to Dr. Animesh Banerjee who got me acquainted with epitaxial growth, fabrication, and characterization. He contributed greatly to my success and was a great friend outside the lab as well. I am also particularly grateful to Sishir Bhowmick, Shafat Jahangir, Saniya Deshpande, Zunaid Baten, and Arnab Hazari for their discussions and contributions, as well Dr. Jimmy Chen and Alan Teran for their discussions in our office. I would like to especially thank my mentee, Arnab Hazari, for his collaboration and friendship over the last two years.

The support of the Lurie Nanofabrication facility. Special thanks to Dennis Schweiger for his generous support and willingness to always help on problems big and small. I am also grateful to the staff of the LNF: Greg Allion, Katherine Beach, Pilar Herrera-Fierro, Rob Hower, Tom Latowski, Sandrine Martin, Matthew Oonk, Kevin Owen, Anthony Sebastian, David Sebastian, Steve Sostrom, Nadine Wang, and Shawn Wright for their mentorship and help in device fabrication.

I am grateful to Lisa Vogel, Melanie Caughey, Laura Jarels, Jim Kozich, Deb Swartz, Beth Stalnaker, and Steve Pejuan for their administrative support throughout my degree. I am also grateful to the National Science Foundation which awarded me a graduate research fellowship and helped fund my research, along with Denso corporation and KAUST. Finally, I am grateful to my family, near and far, who contributed to my success. My parents, Karen and Gary Frost whose unconditional love and

encouragement, were instrumental in my accomplishments and have always supported me. My twin brother, Chris, and little brother, Nick, have driven me to always do my best and this would not have been possible without them.

TABLE OF CONTENTS

DEDICATION ii

ACKNOWLEDGMENTS iii

LIST OF FIGURES ix

LIST OF TABLES xvii

LIST OF APPENDICES xviii

ABSTRACT xix

CHAPTER

I. INTODUCTION 1

1.1 III-Nitride Based Optoelectronics and Motivation 1
1.2 The Need for Solid State lighting 3
1.3 Challenges Facing III-Nitride Research 5
1.3.1 Challenge in p-Doping Gallium Nitride 6
1.3.2 Droop in Light Output Efficiency 7
1.3.3 Wurtzite Crystal Structure and Built-In Polarization Field 9
1.3.4 Substrate Choice for Growth of Gallium Nitride 11
1.3.5 Large Threshold Current Density in InGaN/GaN Quantum Well Lasers 13
1.4 A Different Approach: Use of Quantum Dots 13
1.5 Dissertation Overview 14

II. PLASMA ASSISTED MOLECULAR BEAM EPITAXY OF SELF-ASSEMBLED INGAN/GAN QUANTUM DOTS 17

2.1 Introduction 17
2.2 Crystal Growth of III-Nitride Based Materials 18
2.3 Strasnki-Krastanow Growth of InGaN Islands 21
2.4 Growth and Characterization of Multiple InGaN Quantum Dot Layers 23
2.5 Photoluminescence Characterization of Red-Emitting InGaN Quantum Dots 33

2.6 Time Resolved Photoluminescence 36
2.7 Structural Characterization of Red-Emitting InGaN/GaN Quantum Dots 41
2.8 Summary 44

III. INCORPORATION OF INALN CLADDING LAYERS IN THE DESIGN OF RED-EMITING INGAN/GAN QUANTUM DOT LASERS..45

3.1 Introduction..45
3.2 Growth of $In_xAl_{1-x}N$ 46
3.3 InGaN/GaN Quantum Dot Laser Growth and Fabrication 50
3.4 DC Laser Characteristization..54
3.5 Temperature Dependent Laser Characteristics 58
3.6 Gain and Differential Gain Measurement..59
3.7 Far Field Imaging of the Laser Output 63
3.8 Summary 63

IV. OPTIMIZATION OF INGAN/GAN QUANTUM DOT LASER HETEROSTRUCTURE..65

4.1 Introduction..65
4.2 Motivation for Optimizing InGaN/GaN Quantum Dots and Laser Heterostructure..66
4.3 Optimization of p-doping with Metal Modulated Epitaxy 69
4.4 Laser Heterostructure with all InAlN Cladding..77
4.5 Optimization of Red-Emitting InGaN/GaN Quantum Dots 80
4.5.1 Optimization of InGaN Thickness for Each Dot Layer 80
4.5.2 Optimization of N_2 Interruption During Each Dot Layer 81
4.5.3 Optimization of GaN Barrier Layer Thickness...................................84
4.5.4 Use of InGaN Barriers Between Quantum Dot Layers 85
4.5.4 Generation of Defects During the Quantum Dot Growth....................88
4.5 Summary 90

V. HIGH PERFORMANCE INGAN/GAN QUANTUM DOT RED-EMITTING (λ=630 NM) LASERS 91

5.1 Introduction..91
5.2 Optimized Quantum Dot Laser Heterostructure 92
5.3 DC Laser Characterization..96
5.4 Length Dependent Characterization and Differential Gain 99
5.5 Variation of Spacer Layer Thickness..102
5.6 Summary 103

VI. BIAS MODULATION OF INGAN/GAN QUANTUM DOT LASERS AND MEASUREMENT OF AUGER RECOMBINATION 105

6.1 Introduction……………..105
6.2 Small Signal Modulation of InGaN/GaN Quantum Dot Laser Diodes ...106
6.3 Differential Gain and Gain Compression in Red-Emitting Quantum Dots 110
6.4 Large Signal Modulation of InGaN/GaN Quantum Dot Lasers 113
6.5 Measurement of Auger Recombination Coefficient in InGaN/GaN Quantum Dots...115
6.6 Variation of Auger Recombination Coefficient with Temperature 119
6.7 Comparison of Auger Recombination Coefficient with other Reported Values in the III-Nitride System..120
6.8 Summary 122

VII. SUMMARY AND SUGGESTIONS FOR FUTURE WORK 124

7.1 Summary of the Present Work 124
7.2 Suggestions for the Future Work 127
7.2.1 Heads-Up Displays Incorporating Red-Emitting InGaN/GaN Quantum Dot Lasers 127
7.2.2 Graded Index Separate Confinement Heterostructures......................128

APPENDICES 131

BIBLIOGRAPHY 158

LIST OF FIGURES

<u>Figure</u>

1.1: Bandgap vs. lattice constant for common semiconductors. The III-nitrides are all direct bandgap, shown with a solid line and can be used for devices across the visible spectrum [26]. 3

1.2: Variation of efficiency with wavelength in InGaN and AlGaInP based visible light emitting diodes [27]....4

1.3: Lifetime and necessary electrical power to generate 800~900 lumens of light output along with the product lifetime of three common light sources [28]. 5

1.4: Efficiency droop of a blue-emitting quantum well light emitting diode [43].. 7

1.5: Crystal structure of wurtzite gallium nitride [45]....8

1.6: Band diagram of an InGaN/GaN quantum well LED. The dashed line shows the band structure in absence of the large built in polarization field [46]. 9

1.7: Threshold current density in blue-green based laser diodes [43, adopted from 27]..…12

2.1: (a) Veeco Gen II and (b) Veeco Gen 930 systems used for epitaxial growth in the present study..…20

2.2: Schematic of different growth modes: (a) Frank-van der Merwe, (b) Volmer Weber, and (c) Stranski-Krastanow.. 22

2.3: Quantum dot heterostructure used for characterization of the quantum dot layers. The growth was terminated following the growth of N periods of the active region for N varying from one to five.…....23

2.4: Atomic force microscopy images of uncapped layers of quantum dots. The heterostructure is shown schematically in Fig. 2.3. The values of N are (a) 1, (b) 2, (c) 3, and (d) 4. 25

2.5: InGaN island height and aerial density from the AFM imaging on the samples described in Fig. 2.3. 26

2.6: Schematic of compositional variation of the dot growth along the c-axis plotted alongside the intended distribution (dashed line)....................27

2.7: Schematic of a single photon source using a single layer of the low density InGaN/GaN quantum dots. With an aerial dot density of $<10^8$ cm^2 and an aperture ~1μm^2 (which can be defined with standard photolithography) emission from a single dot can be collected [73].. 28

2.8: Atomic force microscopy images of the single dots in Fig. 2.4(a). The dots generally form a truncated hexagonal pyramid. In some of the dots (a), the island may be elongated and not a regular hexagon....................29

2.9: Distribution of InGaN island heights for typical red-emitting quantum dots. The solid line is the best fit of the scaling function to the measured AFM data. 30

2.10: Scaling functions showing the best fit to this data is i=5 at a growth temperature of 545°C. Note that a higher value of i means higher uniformity.. 31

2.11: Quantum dot laser heterostructure used for photoluminescence measurements... 32

2.12: Typical photoluminescence of red-emitting InGaN/GaN quantum dots as a function of temperature. 32

2.13: Variation of peak emission energy from the red-emitting $In_{0.4}Ga_{0.6}N$/GaN quantum dots as a function of temperature. The red line is a fit to the data with the Varshni relation for the given values of α and β....................33

2.14: Normalized integrated photoluminescence intensity as a function of excitation power and temperature. The quantum efficiency of 35.9% is derived by taking the ratio of the intensities under saturation.. 34

2.15: Photoluminescence decay transient at room temperature. 35

2.16: Change of carrier lifetimes in $In_{04}Ga_{0.6}N$ quantum dots as a function of temperature. 37

2.17: Spectrally resolved photoluminescence transients showing a distinct delay between the GaN and InGaN emission (at 98 K). 38

2.18: Variation of the time delay between the GaN and InGaN emission as a function of temperature, determined by time resolved photoluminescence.........39

2.19: Electron states are discrete and may be separated by energies unobtainable from phonons. Scattering with cold holes is required for electrons to relax into the ground state. This process becomes less efficient at higher temperatures as the supply of cold holes is reduced.. 40

2.20: Quantum dot heterosturcture used for structural characterization in section 2.7 40

2.21: AFM from the uncapped seventh layer of $In_{0.4}Ga_{0.6}N$ quantum dots....41

2.22: Annular dark field image showing seven layers of $In_{04}Ga_{0.6}N$ quantum dots.... 42

2.23: Annular bright field image of a single $In_{04}Ga_{0.6}N$ quantum dot....42

2.24: Variation in the In and Ga compositions measured by energy dispersive x-ray spectroscopy. The underlying image is the annual dark field image of the dot from Fig. 2.22... 43

3.1: Quantum dot laser heterostructure. 46

3.2: Optical mode profile of the laser heterostructure shown in Fig. 3.1 with and without the incorporation of the $In_{0.18}Al_{0.82}N$ cladding layer. 47

3.3: X-ray diffraction rocking curves for InAlN with growth conditions described in table 3.1. 49

3.4: Atomic force microscopy image of lattice matched $In_{0.18}Al_{0.82}N$ on GaN....50

3.5: X-ray diffraction rocking curve from the laser heterostructure. 51

3.6: Schematic showing the etched laser heterostructure. The first mesa is etched to the cladding/waveguide heterointerface to minimize scattering....52

3.7: Scanning electron microscopy images of (a) the ridge-waveguide laser facet and (b) overview of the fabricated device.. 53

3.8: Electroluminescence spectrum below threshold and at 1.1 times threshold. 54

3.9: Variation of the peak emission energy and dominant peak linewidth with injection. 55

3.10: Typical light-current characteristics from the low-reflectivity facet of the laser. 56

3.11: Output polarization of the laser showing a TE threshold at 2.5 kA/cm^2. 57

3.12: Variation of threshold current density with temperature. 58

3.13: Gain spectrum of the red-emitting quantum dots measured using the Hakki-Paoli technique. 60

3.14: Variation of the differential quantum efficiency with laser cavity length. 61

3.15: Variation of the threshold current density with inverse cavity length. 62

3.16: Far field mode profile measured from the low reflectivity laser facet. 63

4.1: Quantum dot laser heterostructure. 66

4.2: Laser light-current-voltage characteristics... 67

4.3: Measured modal gain (points) and calculated modal gain (solid curves) for varying injections. 69

4.4: Heterostructure used for testing diode characteristics of the p-GaN layers grown under various conditions. 72

4.5: Diode I-V characteristics for devices grown with standard p-GaN and MME p-GaN, as described in Table 5.1. The multiple curves on each plot are from different devise on the same chip. 73

4.6: Heterostructure used for measured of electrical characteristics of the p-dopde GaN layers. 74

4.7: Current-Voltage characteristics of the best device on each sample from the diodes with varying p-GaN growth conditions, described in tables 4.1 and 4.3... 76

4.8: InAlN diode heterostructure. The thin p+GaN on top is to reduce the contact resistance. 77

4.9: Diode I-V characteristics with the $In_{0.18}Al_{0.82}N$ grown at 497ºC, and 480ºC. 78

4.10: Quantum dot heterostructure used for optimizing the quantum dot efficiency. The InGaN thickness, GaN barrier thickness, and nitrogen interruption time were optimized. 81

4.11: Variation of (a) optical properties, (b) structural properties, and (c) carrier lifetimes with change in deposited InGaN thickness. 82

4.12: Variation of (a) optical properties, (b) structural properties, and (c) carrier lifetimes with change ininteruption time. 83

4.13: Variation of (a) optical properties, (b) structural properties, and (c) carrier lifetimes with change in the barrier thickness. 85

4.14: Optimized Laser heterostructure with $In_{0.04}Ga_{0.96}N$ waveguide layers and $In_{0.08}Ga_{0.92}N$ barriers. 86

4.15: Room temperature and 30 K temperature emission from which an internal quantum efficiency of 51% is derived.. 87

4.16: Quantum dot sample etched to expose defects. The dark hexagonal pits correspond to dislocations.. 88

4.17: Etch pit dislocation experiment on GaN on sapphire templates.. 89

5.1: Quantum dot laser heterostructure. 93

5.2: Light-current characteristics for a 5 mm x 1 mm laser without high reflectivity facet coating. 95

5.3: Electroluminescence spectrum from one of the uncoated facets of the optimized laser. 96

5.4: Light-current characteristics from the low reflectivity of a DBR coated laser at room temperature under pulsed bias. 97

5.5: Temperature dependence of the threshold current density of a laser with DBR coating. 98

5.6: Variation of inverse differential quantum efficiency with cavity length. 99

5.7: Variation of threshold current density with inverse cavity length. 100

5.8: Variation of threshold current density and maximum output power from lasers with no facet coating as a function of spacer thickness. 101

5.9: Light current characteristics of a laser (LED) with no electron blocking layer showing no threshold...102

6.1: Laser heterostructure used for small and large signal modulation measurements described in chapter 4, grown by molecular beam epitaxy. The lasers are fabricated into ridge geometry lasers, using the process outlined in Appendix B. 107

6.2: Light-current characteristics of a typical laser fabricated with the heterostructure shown in Fig. 6.1. The output spectral characteristics are shown at 2.7 kA/cm^2 (1.1J_{th}). 108

6.3: Small signal modulation response of the $In_{0.4}Ga_{0.6}N$/GaN quantum dot laser diodes (points) and fit of the measured response curves (solid lines)...............109

6.4: Variation of the laser resonant frequency with the square root of the injection current above threshold. The plotted resonant frequencies are fit using the damped oscillator model to the measured response curves in Fig. 6.3. 111

6.5: Variation of the laser resonant frequency with the square root of the injection current above threshold. The plotted resonant frequencies are the values fit using the damped oscillator model to the measured response curves in Fig. 6.3. 112

6.6: Measured electrical and optical signals showing the laser diode response to a large signal current pulse driving the laser above threshold. The time delay, τ_d, is indicated in the plot...115

6.7: Variation in the measured values of the delay time with current injection at room temperature. The solid line indicates the calculated delay time with injection. 116

6.8: Variation in the time delay with temperature at a current bias of 100 mA. The small increase in delay with temperature is likely due to electron-hole scattering in the quantum dots, as described in chapter 2 and section 6.5. 117

6.9: Variation of the Auger coefficient with temperature from the measured time delays shown in Fig. 6.7...119

6.10: Variation of Auger coefficient with bandap: expected (dashed grey lines) and measured (points). The red, blue, and green circles were measured in quantum dot or nanowire heterostructures where defects play a reduced role in recombination [adapted from 137, 140]. 121

7.1: Heads-up display where visible lasers are used to project the drivers speed and directions on the windshield [143]. 127

7.2: Calculated optical confinement factor of the laser heterostructure as a function of maimum composition in the graded $In_{0->x}Ga_{1->x}N$ cladding. The defect densites were measured in samples grown up to the active region. 128

7.3: Proposed graded separate confinement heterostructure. 129

B.1: Laser heterostructure post-growth.. 134

B.2: Laser heterostructure after ridge etch... 135

B.3: Laser heterostructure after mesa etch... 136

B.4: Laser heterostructure after deposition of n-metal........137

B.5: Laser heterostructure after oxide deposition.. 138

B.6: Laser heterostructure after via hole etch.. 139

B.7: Laser heterostructure after p-metal deposition.. 140

C.1: Shchematic of steady state photoluminescence setup for measuring ultra-violet and visible photoluminescence. The PMT can be replaced with a Ge detector for measuring near infrared extending the measurement range from 325 nm to 1700 nm... 141

C.2: Schematic of voltage-current characterization setup........142

C.3: Schmetaic of the small signal modulation characteriation setup. This is used for measuring the modulation bandwidth, differential gain, and gain compression. This setup can also be used for measuring differentail carrier lifetime in light emitting diodes 143

C.4: Measurement setup for measuring chirp and linewdith enhancement with small signal biasing 144

C.5: Measurement setup for testing laser diode reliability over long periods of time.... 145

C.6: Measurement setup for analyzing far field and near field patterns of laser diodes. A standard charged coupled device (CCD) detector may be substituted for the 7290 Microviewer 146

C.7: Measurement setup for characterizing light-current-voltage characteristics of the lasers 147

C.8: Setup for measuring spectral characteristics of the laser or light emitting diodes 148

C.9: Setup for measuring photoluminescence and carrier lifetimes in materials with visible emission. 149

LIST OF TABLES

Table

1.1: Typical substrates used for the growth of GaN. The corresponding lattice mismatch and typical dislocation densities (in cm^{-2}) in GaN on these substrates are also listed. 11

3.1: Variation in the growth conditions of InAlN layers. 48

4.1: Growth conditions for standard p-doped GaN and recipe for metal modulated epitaxy p-doped GaN.. 71

4.2: Comparison of hole concentration, mobility and resistivity of p-doped GaN layers.... 74

4.3: Growth conditions of the MME p-GaN for testing the diode characteristics. The description column lists the changes in each device from table 4.1. 75

4.2: Electrical characteristics from the diodes described in table 4.3. 76

6.1: Characteristics of deep level traps in GaN, grown by plasma-assisted molecular beam epitaxy, obtained from transient capacitance measurements. 118

LIST OF APPENDICES

APPENDIX

A: Substrate Preparation Prior to MBE Growth. 132

B: Quantum Dot Ridge Waveguide Laser Processing...133

C: Measurement Setup Schematics.. 141

D: Transfer Matrix Method Simulations...150

ABSTRACT

Visible and ultra-violet (UV) light sources have numerous applications in the fields of solid state lighting, optical data storage, plastic fiber communications, heads-up displays in automobiles, and in quantum cryptography and communications. Most research and development into such sources is being done using III-nitride materials where the emission can be tuned from the deep UV in AlN to the near infrared in InN. However due to material limitations including large strain, piezoelectric polarization, and the unavailability of cheap native substrates, most visible devices are restricted to emission near GaN at 365 nm up to around 530 nm. Self-assembled InGaN/GaN quantum dots (QDs) can be epitaxially grown in the Stranski-Krastanow growth mode. These dots are formed by the relaxation of strain, and it has been shown both theoretically and experimentally that the piezoelectric field and the resultant quantum confined stark effect are significantly lower than those values reported in comparable quantum wells (QWs). As a result, the radiative carrier lifetimes in such dots are typically around 10-100 times smaller than those in equivalent QWs. Furthermore, the quasi-three dimensional confinement of carriers in the InGaN islands that form the dots can reduce carrier migration to (and therefore recombination at) dislocations and other defects.

In the present study, molecular beam epitaxial growth and the properties of InGaN/GaN self-assembled quantum dots have been investigated in detail. The quantum dots, emitting at 630 nm, have been studied optically through temperature dependent,

excitation dependent, and time-resolved photoluminescence. A radiative lifetime of ~2 ns has been measured in these samples, which agrees well with theoretically predicted values. Samples with varying number of dot layers were grown and characterized structurally by atomic force microscopy. The density of the quantum dots is found to increase from 7×10^{7} cm^{-2} on the first layer to ~5×10^{10} cm^{-2} on subsequent layers. The dot height follows a similar trend increasing from 3 to 5 nm while the base width of the quantum dots is relatively fixed. The growth conditions of the dots have been optimized including the InGaN and GaN thickness and the nitrogen interruption time. The optimized dots have been incorporated into edge-emitting laser heterostructures. Other optimizations including the novel use of an all $In_{0.18}Al_{0.82}N$ cladding are incorporated into the laser heterostructure to optimize the output power and reduce loss.

The first red emitting quantum dot lasers, emitting at up to 630 nm have been realized in the present study. These lasers show good performance compared with other material systems, including InGaAlP/GaAs and AlGaAs based red lasers. They are characterized by relatively low threshold current densities (1.6 kA/cm^2) and high temperature stability (T_0~240 K). The maximum measured output power is 30 mW, making them suitable for the application discussed above. The lasers have also been characterized by a maximum modal gain of 35 cm^{-1} and differential gain of 9.0×10^{-17} cm^2. Dynamic characterization of the lasers has also been performed from which a maximum small signal modulation bandwidth of 2.4 GHz has been measured.

Chapter I

Introduction

1.1 III-Nitride Based Optoelectronics and Motivation

Recent demand for visible and ultra-violet light emitting diodes and lasers is immense due to their numerous applications in the fields of solid state lighting, optical data storage, plastic fiber communication, full color mobile projectors, heads-up displays, and in quantum cryptography and computing [1,2]. Most research and development into these light sources is being done using nitride- based materials where the emission can be tuned from deep UV in AlN (~6 eV) to the near infrared by using InN (~0.7 eV). Since the first report of a blue-emitting InGaN/GaN quantum well (QW) LED in 1995 [3], much progress has been made in extending the emission to longer wavelengths through the incorporation of more indium in the InGaN QWs [4-11]. While the first blue-emitting laser was demonstrated by Nakamura in 1996 [12], it has since become increasingly difficult to grow and fabricate lasers at longer wavelengths. It was only as recently as 2009 that the first green-emitting laser was demonstrated using InGaN/GaN QWs [13], and red-emission has yet to be shown with such QWs. To fully realize the potential of these nitride based lasers, it is necessary to further extend the emission wavelength of these devices beyond green into the red which will allow for the production of solid state projectors and white light sources from a single material system.

The large indium composition and associated strain in the ternary InGaN QWs lead to clustering effects and a large piezoelectric polarization field, especially in c-plane heterostructures, both of which are detrimental in laser performance. The threshold current density of these lasers is generally very large due to reduced electron-hole (e-h) wavefunction overlap in the QWs [4-9, 14-15]. Additionally, a large blue shift of the emission peak with injection is observed due to the quantum confined Stark effect (QCSE) associated with the polarization field [13]. It has been shown that material inhomogeneities and the piezoelectric field increase in InGaN/GaN QWs with increasing indium content. Further, a wider well width that is needed for emission at longer wavelengths is not an option since the band bending due to a strong polarization field reduces e-h wavefunction overlap significantly. It is for these reasons that red-emitting lasers with InGaN/GaN QWs have not yet been demonstrated. InGaP/InGaAlP double-heterostructure and QW lasers lattice matched to GaAs and emitting in the red wavelength region of 650-670 nm have been reported [16-18]. However, these devices are characterized by very large values (5-10 kA/cm^2) and strong temperature dependence (T_0 ~ 50–100 K) of the threshold current density. Both of these characteristics are detrimental in real high-performance applications.

Self-assembled InGaN/GaN quantum dots (QDs) can be epitaxially grown in the Stranski- Krastanow growth mode [19-23]. These dots are formed by the relaxation of strain, and it has been shown both theoretically [24-25] and experimentally [19-23] that the piezoelectric field and the resultant QCSE are significantly lower than those values reported in comparable QWs. As a result, the radiative carrier lifetimes in such dots are typically around 10-100 times smaller than those in equivalent QWs [21]. Furthermore,

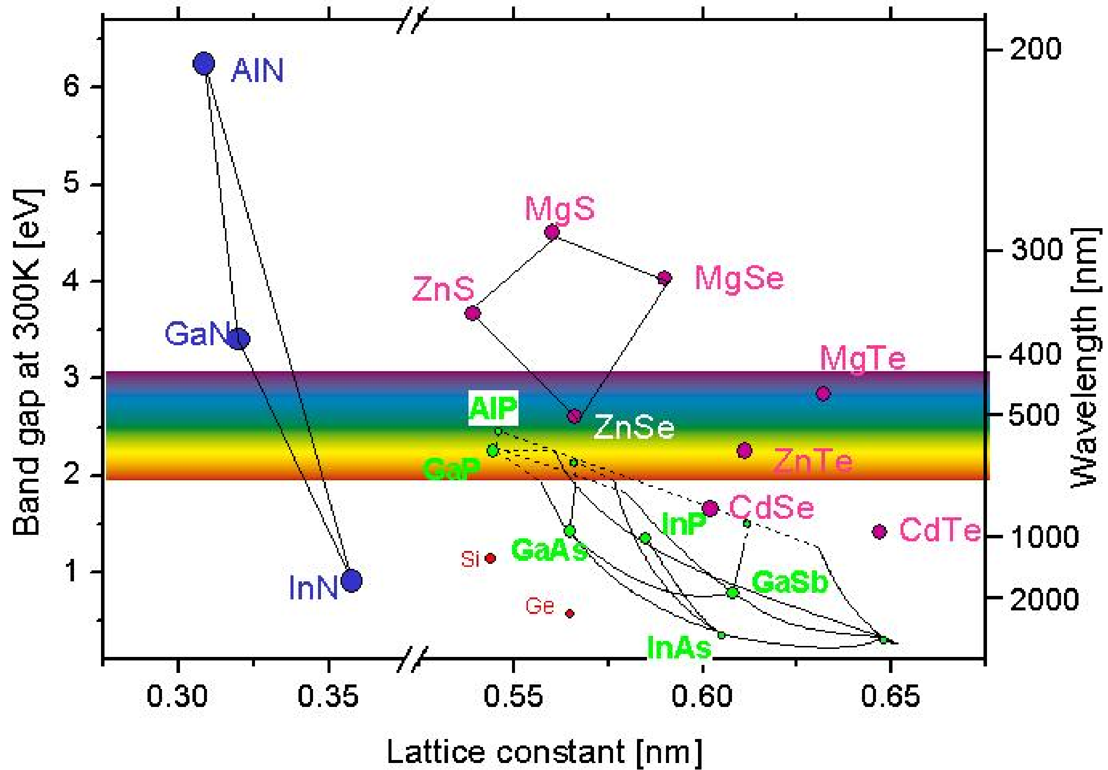

Fig. 1.1 Bandgap vs. lattice constant for common semiconductors. The III-nitrides are all direct bandgap, shown with a solid line and can be used for devices across the visible spectrum [26].

the quasi-three dimensional confinement of carriers in the InGaN islands that form the dots can reduce carrier migration to (and therefore recombination at) dislocations and other defects.

1.2 The Need for Solid State Lighting

Electrical light sources, going back to the original incandescent light bulb, have revolutionized the way people live their lives, enabling lighting of any space at any time. Such early electrical lighting sources produce light through the heating of a thin filament and the emission of black body radiation. A large portion of this light is emitted in the infrared, beyond human vision. Fluorescent lighting reduces the wasteful infrared light and have increased efficiencies. However, parasitic energy losses are still significant.

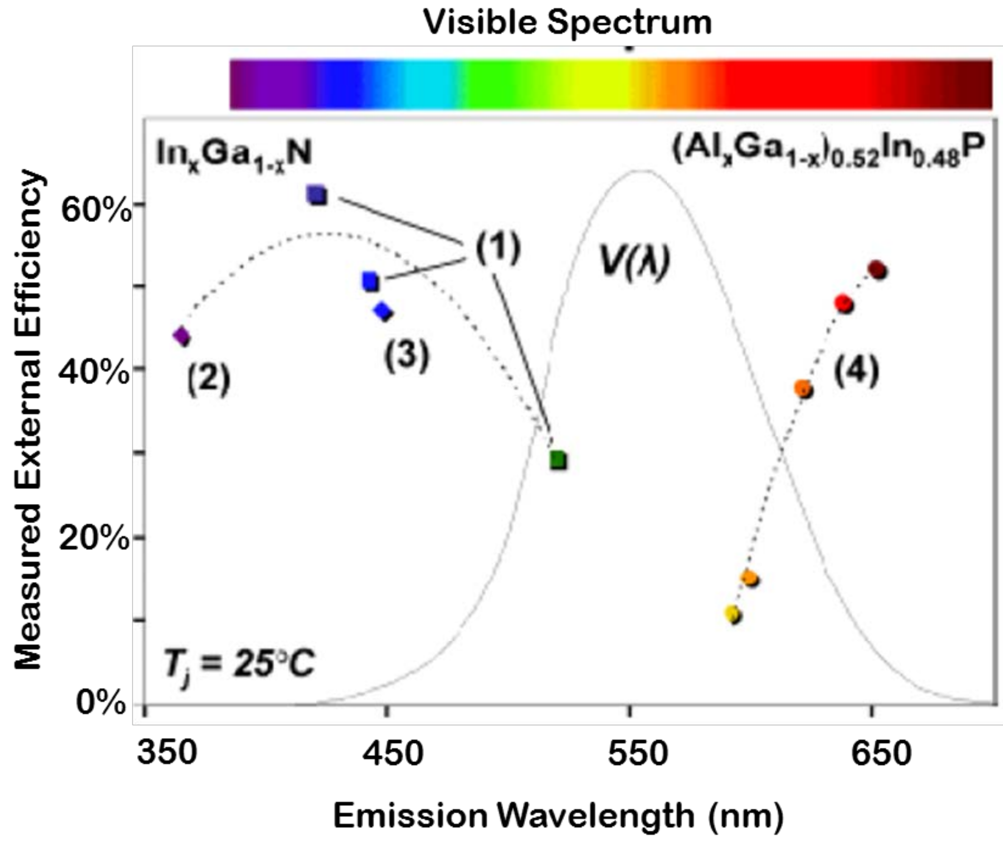

Fig. 1.2 Variation of efficiency with wavelength in InGaN and AlGaInP based visible light emitting diodes [27].

Additionally, these light sources require mercury and require special disposal procedures after use. Semiconductor based solid-state lighting further reduces loss by converting electricity directly into visible light through the recombination of electron-hole pairs. In particular, nitride based materials are direct bandgap with emission across the visible spectrum, as shown in Fig. 1.1 [27].

Challenges in the production of nitride-based devices emitting across the visible spectrum are described in more detail in section 1.3. As the indium composition in InGaN quantum wells is increased, a reduction in the light output efficiency is typically reported, leading to very high efficiency devices emitting in the blue and reduced efficiencies in

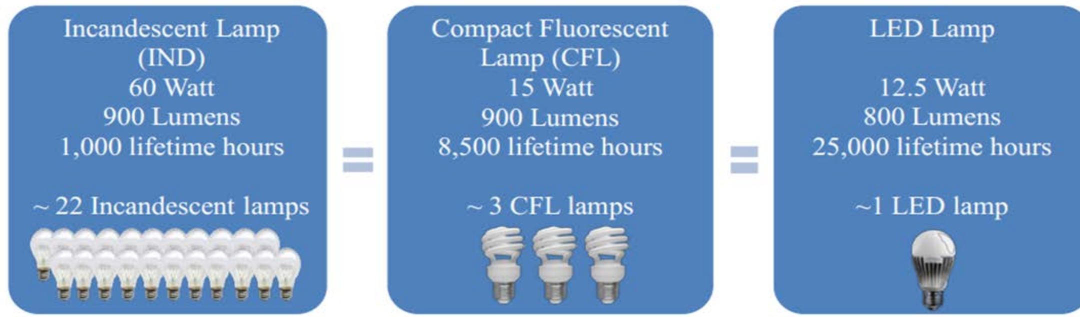

Fig. 1.3 Lifetime and necessary electrical power to generate 800~900 lumens of light output along with the product lifetime of three common light sources [28].

the green with no red-emitting quantum well lasers yet reported. Alternatively, InGalAlP based devices, with can be used for longer wavelength emission, down to ~650 nm [16-17, 27], with a rapid drop off in efficiency at shorter wavelengths, shown in Fig. 1.2. The lack of efficient emitters ~500-550 nm is known as the "green gap." InGaN/GaN quantum dots as an alternative, can be used to extend the emission wavelength and bridge this green gap, allowing for red-blue-green emission from a single material system [20-22].

Alternatively, a blue-emitting InGaN/GaN quantum well light emitting diode can be used to pump a phosphor with emission in the red or yellow. This is the most typical method for generation of white light from nitride based LEDs. Additionally, these light emitting diodes have very long lifetimes, shown in Fig. 1.3. An LED based light has a typical lifetime of ~25,000 hours compared with ~8,500 hours with fluorescent lighting, and 1000 hours with incandescent lighting [28].

1.3 III-Nitride Research: Challenges and Recent Progress

Several challenges exist in the development of III-nitride solid state light sources including p-doping, droop in the output efficiency, large inherent polarization field, and

the unavailability of cheap native substrates. Additionally, lasers fabricated from III-nitride heterostructures have very large threshold current densities, particularly at longer wavlengths. These issues are discussed in the following subsections of 1.3.

1.3.1 Challenge in p-Doping Gallium Nitride

Progress in the growth of III-nitride based electronics was very slow in the 1970's to early 1990s largely due to the unavailability of native substrates and the inability to p-dope GaN, necessary for electrically injected devices [29-30]. Due to the relatively large hole masses in the III-nitride system (m_{hh}~m_0), acceptor levels tend to be ~200 meV above the valence band edge, leading to very inefficient activation at room temperature (k_BT~25.8 meV), as described in more detail in section 4.3. Additionally, a high background n-type doping is typically present during the growth of GaN due to the unintentional incorporation of oxygen and the presence of nitrogen vacancies in the crystal, both of which act as compensating donors. Additionally, the presence of hydrogen during the MOCVD growth of GaN led to the formation of Mg-H complex rather than the desired substitional incorporation of a Mg atom. A post-growth thermal annealing technique was demonstrated by Nakamura in 1992 which led to the demonstration of the first electrically injected GaN diodes and light emitting diodes incorporating InGaN/GaN quantum wells [3, 12, 30]. Since then, high quality p-doping has been demonstrated through the use of group III rich growth [21, 31] by numerous groups and through growth at low substrate temperatures under N_2-rich growth by Bhattacharya, *et. al.* [32].

1.3.2 Droop in Light Output Efficiency in III-Nitride Based LEDs

While issues with p-doping of GaN have largely been alleviated through the research of a number of research groups [33-42], droop still plagues the solid state lighting industry. Ideally, in a solid state light source, each injected electron-hole (e-h) pair would recombine to produce one photon of light. However, due to non-radiative processes including Shockley Read Hall (SHR) and Auger recombination this often isn't true. Additionally, the relatively large defect density present in these substrates, discussed in section 1.3.4 and chapter 6 may further exacerbate the rate of Auger recombination.

Quantum well based diodes are typically characterized by an initial sharp rise in efficiency at low currents. Fig. 1.4 shows a typical light output efficiency vs current plot

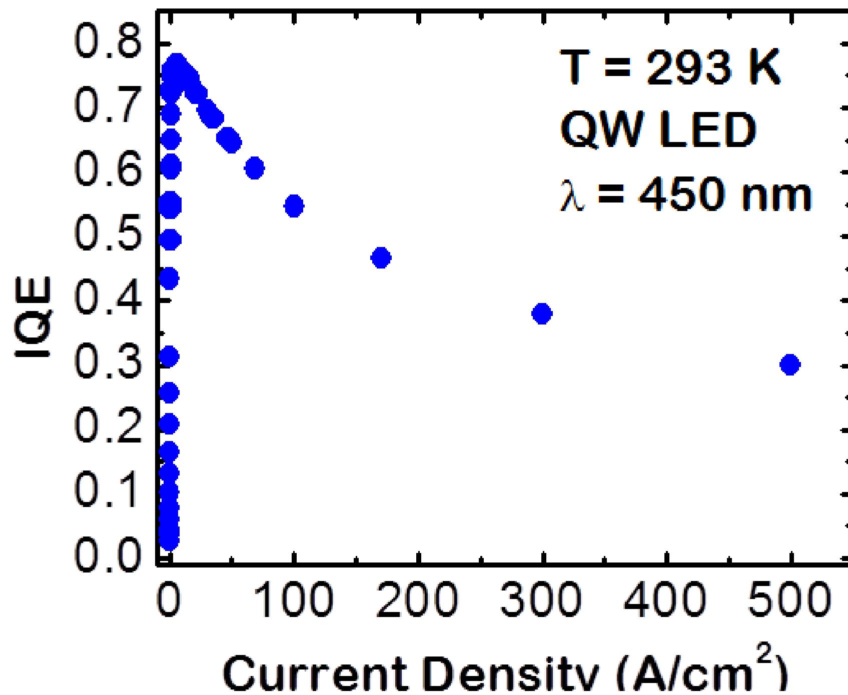

Fig. 1.4 Efficiency droop of a blue-emitting quantum well light emitting diode [43].

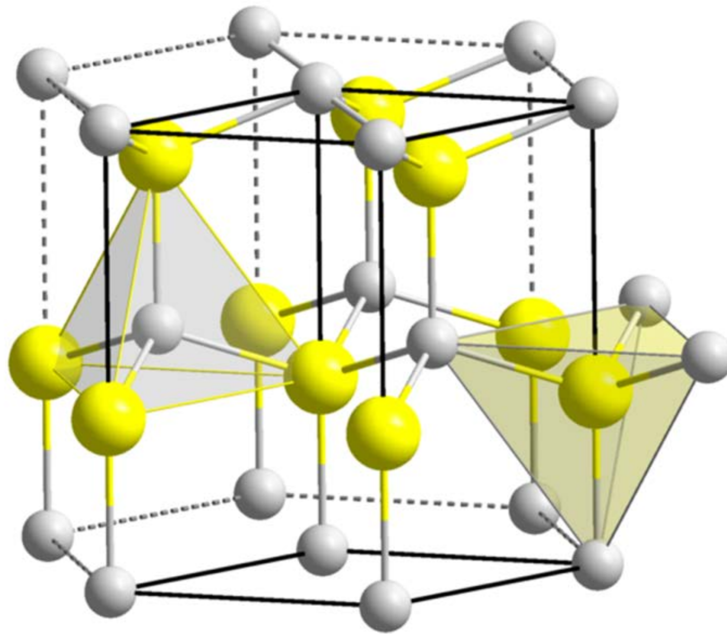

Fig. 1.5 Crystal structure of wurtzite gallium nitride [45].

in an InGaN/GaN quantum well light emitting diode [43]. At elevated current densities, a reduction in the efficiency is observed which becomes more severe for longer wavelength LEDs. Widespread research has been carried out into the origin out into the origin of the “droop” phenomenon and several solutions have been proposed to reduce it. Droop has been suggested to be due to non-radiative Auger recombination [33, 37], electron leakage from the quantum wells [34], device self-heating [35], and exciton dissociation [36]. Auger recombination as the dominant mechanism was first proposed by Krames, *et. al*. in 2008 at Phillips Lumileds [37] and several other groups have substantiated this claim including Drager, *et. al*. [38] and Bhattacharya, *et. al* [39]. This is still the most promising mechanism with much research continuing in substantiating this claim [ ].

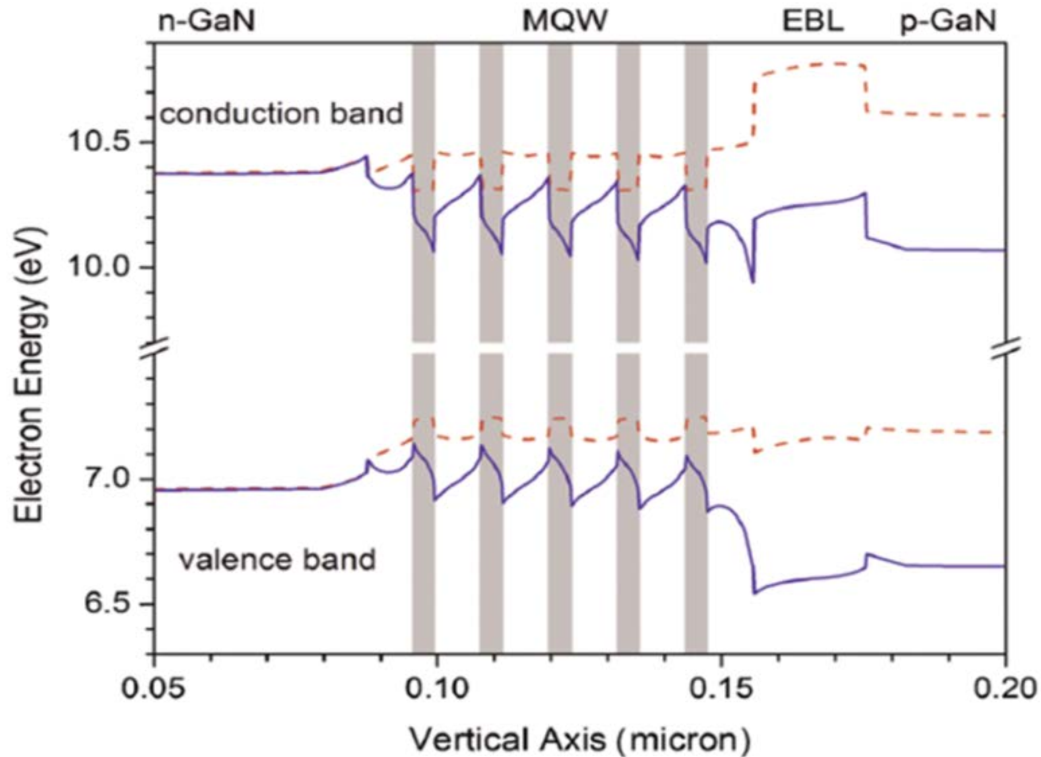

Fig. 1.6 Band diagram of an InGaN/GaN quantum well LED. The dashed line shows the band structure in absence of the large built in polarization field [46].

Elevated levels of Auger recombination due to a defect assisted or phonon assisted Auger process may also lead to larger than expected Auger recombination [44].

1.3.3 Wurtzite Crystal Structure and Built-In Polarization Field

Gallium nitride is mostly commonly grown in the wurtzite crystal form, shown schematically in Fig. 1.5 [45], unlike most other common semiconductors including silicon, gallium arsenide, and indium phosphide based material systems which grow in a cubic crystal structure. The hexagonal wurtzite crystal is not symmetric along the c-axis (0001), the most commonly used crystal plane in III-nitride devices. Due to the large difference in electronegativity between the constituent gallium and nitrogen atoms and the lack of inversion symmetry, a small dipole moment exists within the GaN unit cell.

This creates a very large spontaneous polarization field in the nitrides [15]. This field leads to accumulation of polarization charges at heterointerfaces which can be as high as 2 MV/cm in AlGaN/GaN [15]. Several designs of high electron mobility transistors take advantage of this large built in sheet charge density.

Additionally, strained heterostructures, with their distorted crystal structure have an additional piezoelectric polarization which also plays an important role in InGaN/GaN heterointerfaces due to the large lattice mismatch between these materials. Fig. 1.6 shows a typical band structure for a III-nitride based LED with (solid line) and without (dashed line) band bending. The large field in the shaded regions leads to a physical separation of electrons and holes, shown schematically in Fig. 1.6, leading to inefficient recombination. Longer wavelength devices require higher indium composition in the wells, but this leads to higher polarization fields and further electron-hole separation [4-11, 24-25]. For this reason, long wavelength (beyond green) laser have yet been demonstrated with InGaN/GaN quantum wells.

Due to the relatively small electron mass (in comparison with the hole mass), electrons may leak across the active region into the p-doped side of the diode. For this reason, an electron blocking layer [46-47], shown schematically in Fig. 1.6 is typically incorporated into the laser heterostructure. However, due to the large band bending, this is pulled down in such quantum well devices, reducing its effectiveness. Additionally, a large triangular potential is developed in the valence band which can lead to non-uniform injection of holes and pile up of holes in the first few quantum wells. Finally as carriers are injected into the device, they screen the built in polarization field leading to a reduction in the band bending and a corresponding blue-shift of the emission. This effect

Substrate	Lattice Mismatch with GaN	Typical Dislocation Density
GaN	0	$10^4 - 10^6$
Sapphire	3.4%	$10^7 - 10^8$
6H SiC	13%	$10^8 - 10^9$
Silicon	17%	10^{10}

Table 1.1 Typical substrates used for the growth of GaN. The corresponding lattice mismatch and typical dislocation densities (in cm^{-2}) in GaN on these substrates are also listed.

is known as the quantum confined Stark effect (QCSE) and can lead to large shifts in the emission wavelength (~20-30 nm) for quantum well LEDs and lasers [4-11].

Several methods [48-50] have been attempted to reduce the effects of the built in polarization field including growth on semi-polar or non-polar substrates (off the c-axis). InGaN based quantum well LEDs and lasers on these substrates emitting in the blue and green have been demonstrated. While these results are promising, these devices suffer from low peak efficiencies in LEDs and high lasing thresholds in lasers (up to 10 kA/cm^2). The use of quantum dots can also reduce the effects of the polarization field and is discussed in more depth in section 1.4.

1.3.4 Substrate Choice for Growth of Gallium Nitride

Gallium nitride is typically not grown on native substrates due to the immense time required to generate them and the cost associated with such substrates, with a typical 2" wafer of GaN costing between $5,000-$10,000, and larger substrates being commercially unavailable. An alternative is to grow III-nitrides on foreign substrates most commonly being silicon carbide, sapphire, or silicon which are cheaper and available in larger areas needed for mass scale applications. However, the lattice mismatch in these substrates,

Fig. 1.7 Threshold current density in blue-green based laser diodes [43, adopted from 27].

summarized in table 1.1 lead the formation of a relatively large number of dislocations, on the order of 10^8-10^{10} cm^{-2}. These defects give rise to non-radiative recombination pathways and further degrade the performance of LEDs and lasers as described in the previous sections. A defect assisted Auger process has been proposed as the source of the relatively large values of Auger coefficient compared with theoretical values. This has been discussed in more depth in chapter 6 following the measurement of Auger recombination in red-emitting quantum dots. Still, GaAs based devices having such high defect densities would not have any significant radiative characteristics and it is through the unique properties of the nitrides that high performance LEDs and laser diodes have been demonstrated.

1.3.5 Large Threshold Current Density in InGaN/GaN Quantum Well Lasers

Preliminary reports on InGaN based laser diodes were published in 1995 by Nichia on c-plane GaN with an emission wavelength at 400 nm (very short wavelength blue emission) [12]. However, as described in section 1.1, InGaN based diodes should be able to cover the entire visible spectrum into the near infrared. Despite relentless research since the first InGaN laser demonstration, it was only as recently as 2009 [13] that the first demonstration of lasers with an emission wavelength at 500 nm was reported. Due to the very large polarization field inherent in InGaN/GaN based heterostructures, the electron-hole overlap becomes significantly smaller at higher indium compositions needed for long wavelength emission. This leads to an increase in the radiative lifetime from ns to 100s ns (at low injection) [24,25]. Screening this field to increase the radiative recombination rate leads to very large lasing thresholds, shown in Fig. 1.7 for the many groups working on the demonstration of InGaN/GaN based laser diodes. Additionally, the longer wavelength devices require a lower growth temperature to incorporate sufficient indium into the quantum wells which leads to clustering and rough surface morphology. These effects can be partially reduced by incorporating InGaN/GaN quantum dots, grown by molecular beam epitaxy which can reduce the built in polarization field.

1.4 A Different Approach: Use of Quantum Dots

Many of the challenges outlined in section 1.3 can be alleviated through the use of InGaN/GaN quantum dots instead of quantum wells [19-25]. The quantum dots form by the relaxation of strain and therefore have an inherently smaller piezoelectric field. Additionally, the physical 3-dimensional confinement of carriers can reduce non-

radiative recombination at defects. This approach has been used in this dissertation. InGaN/GaN quantum dots are demonstrated at emission wavelengths into the red (630 nm) and are incorporated into laser heterostructures [21-23, 51-52]. While these advantages (reduced polarization and non-radiative recombination) are unique to nitride based quantum dots, they also have many of the same advantage of quantum dots demonstrated with other material systems. The incorporation of self-organized quantum dots in GaAs and InP based heterostructures have resulted in superior device performance [53-55]. These lasers have extremely small threshold current density, wide tunability of the output wavelength, large modulation bandwidth, and near zero chirp and linewidth enhancement factor [53]. These superior properties of quantum dots are discussed in later chapters and have also been investigated by others, although in shorter wavelength devices.

1.5 Dissertation Overview

The purpose of this research is to demonstrate the advantages of quantum dots in visible laser diodes through detailed materials characterization of such InGaN/GaN quantum dots grown by molecular beam epitaxy and through their incorporation in laser diodes. In particular, the first demonstration of red-emitting lasers from the III-nitride material system is described in this dissertation. Optimized quantum dots address many of the challenges facing the nitride industry including those described above. The strain relaxation and resultant reduced piezoelectric polarization can allow for devices at long wavelength with reduced threshold current densities. The physical confinement of carriers can reduce the mobility of carriers to travel to non-radiative centers in addition to the increase in radiative recombination.

Chapter II describes the molecular beam epitaxial growth of self-assembled InGaN/GaN quantum dots with high efficiencies and low piezoelectric polarization field, emitting at 630 nm by plastic assisted molecular beam epitaxy. The growth mode of the quantum dots is described and it is found that the density increases from the first to the third layer. The relatively low density of quantum dots on the first layer, make it ideal for use in a single photon source, but reduces the modal gain in lasers, requiring the growth of one additional layer than desired. Additionally, the dots are characterized by atomic force microscopy and transmission electron microscopy. The optical properties are measured by temperature and excitation dependent photoluminescence. From time resolved photoluminescence, a radiative lifetime of ~2 ns is measured. A carrier relaxation bottleneck is also reported.

The growth of $In_{0.18}Al_{0.82}N$ is reported and is incorporated in the laser heterostructure to increase the modal gain and reduce the cavity loss, are described in chapter III. This layer is lattice matched to GaN. This layer is incorporated into red-emitting lasers and the first nitride-based red-emitting lasers are reported. The lasers are characterized by relatively low threshold current densities (J_{th}=2.5 kA/cm^2) and high temperature stability (T_0~240 K) compared with other red-emitting lasers including InGaAlP/GaAs and AlGaAs/GaAs lasers (J_{th}~6-8 kA/cm^2, T_0=60~80 K).

Chapter IV described the growth optimization of the InGaN/GaN quantum dots and the laser heterostructure. The InGaN dot and GaN barrier thickness is optimized along with the nitrogen interruption time. The optimized dots have an efficiency of up to 51%. The laser is also redesigned with an all $In_{0.18}Al_{0.82}N$ cladding, further reducing the threshold current density and increasing the laser efficiency by increasing the modal gain

and reducing the cavity loss. Finally, the p-doping of the GaN layer is optimized by the use of metal modulated epitaxy. The growth is optimized to reduce the series resistance and reducing the leakage current.

The optimizations are incorporated into laser heterostuctures, described in chapter V. The lasers are characterized by a further reduced threshold current density (~1.6 kA/cm^2), higher output power (30 mW), and reduced cavity loss (~9 cm^{-1}) compared with the preliminary devices reported in chapter III. The lasers are characterized by length dependent light-current measurements from which a differential gain of $9x10^{-17}$ cm^2 is derived. This value is 5x larger than the value reported for shorter wavelength InGaN/GaN quantum well based lasers and comparable with shorter wavelength blue- and green-emitting quantum dot based lasers. The lasers are also characterized by high temperature stability with T_0~240 K.

The dynamic characteristics of quantum dot lasers are presented in chapter VI. The red-emitting quantum dot lasers are characterized by a maximum modulation bandwidth, f_{-3dB}=2.4 GHz, making them suitable for plastic fiber communications. From the small signal modulation, a differential gain of $5x10^{-17}$ cm^2 is derived, comparable with the values reported from the length dependent characteristics in chapter III and V. Large signal modulation of the lasers can be used to measure the Auger recombination coefficient. A value of 10^{-31} cm^6s^{-1} is found in the red-emitting InGaN/GaN quantum dots, which is comparable with expected values from material with an emission of ~1.9 eV.

Finally, chapter VII summarizes the work performed in this dissertation and suggests some future work, involving red-emitting quantum dots.

Chapter II

Plasma Assisted Molecular Beam Epitaxy of Self-Assembled InGaN/GaN Quantum Dots

2.1 Introduction

Lasers emitting in the 600 nm wavelength range have recently gained attention for a number of important application including optical information processing, plastic fiber communication systems, optical storage, and full color (RGB) laser displays and projectors [1-2]. Shorter wavelength visible lasers can be realized with GaN based heterostructures having InGaN/GaN quantum wells as the gain media [4-13]. However, the performance of these devices at longer wavelengths (into green) is currently limited by both material inhomogeneity and effects related to a large-strain induced polarization in the quantum wells [7, 25]. Furthermore, a laser emitting in the red (λ~630nm) has not been realized yet been realized with InGaN/GaN quantum wells. Strain relaxation during dot formation results in reduced polarization fields and consequently low threshold current density [24, 25], smaller blue shift of the emission peak, very weak temperature dependence of J_{th} and linearly TE polarized output.

InGaN/GaN self-organized quantum dots can be epitaxially grown in the Stranski-Krastanow growth mode [20-25]. The dots are formed by strain relaxation and therefore the piezoelectric field and resulting QCSE are significantly lower than those in

comparable quantum wells [20-25]. Consequently, radiative carrier lifetimes in the dots are 10-100 times smaller than in the wells [25]. Additionally, the quasi-three dimensional confinement of carriers in the InGaN islands that form the dots can reduce the rate of non-radiative recombination of carriers at dislocations and related defects. This chapter describes the growth mode of these InGaN islands, and additionally detailed optical and structural characterization of such quantum dots are discussed.

2.2 Crystal Growth of III-Nitride Based Materials

High quality nitrides have been demonstrated using a variety of growth techniques including metal organic chemical vapor epitaxy (MOCVD) [56], hydride vapor phase epitaxy (HVPE) [57], and molecular beam epitaxy (MBE) [11, 20-25]. HVPE is widely used for the growth of bulk GaN layers due to the very large growth rate (~ 50 μm/hr), while quantum confined heterostructures are typically grown by MOCVD [4-10]. As an alternative to these two techniques, MBE provides several important advantages. First, typical growth temperatures are 100-200°C lower than those in MOCVD growths, which is favorable for increasing the indium incorporation in epitaxy layers. This is particularly useful for long wavelength lasers (beyond 530 nm) where $In_xGa_{1-x}N$ with $x \geq 0.4$ is required. Additionally, this allows for the growth of high quality $In_{0.18}Al_{0.82}N$ layers, improving the optical confinement in such long wavelength lasers [21]. A second inherent advantage is the relatively high vacuum environment which suppresses defects in epitaxial layers. Third, the growth rate in MBE can be precisely controlled at the submonolayer level, allowing for the precise control needed for the growth of quantum dots. Finally, in situ monitoring including reflective high energy electron diffraction allow for improved control during the growth.

Epitaxial growths for this work were carried out in a Veeco Gen II plasma assisted molecular beam epitaxy (PA-MBE) system or Veeco Gen 930 PA-MBE system, shown in Figs. 2.1 (a) and (b), respectively. In contrast to MOCVD where group III alkyls (TMGa, TMIn, TMAl) [56] are brought into the growth chamber through heated bubblers by carrier gasses, group III elements (Ga, In, Al) are thermally generated and impinge on the sample surfaces [58]. Additionally, unlike MOCVD and ammonia based MBE, high purity nitrogen gas (N_2) is used as to generate the active N species.

In ammonia-based MBE, active nitrogen are obtained when the ammonia (NH_3) molecules are cracked on the growth surface. While the cracking efficiency increases with substrate temperature, it remains low (4%) even at 800°C, requiring a large NH_3 flow rate during growth. This gas can be highly corrosive leading the necessity of large capacity pumps and special corrosion resistant source cells and chamber walls. Alternatively, active nitrogen species can be generated in a plasma tube in radio frequency (RF) PA-MBE. In contrast to ammonia based MBE, the amount of active nitrogen species is independent of growth temperature and depends on the flow rate of nitrogen into the plasma source and RF power. The plasma source used in the experiments presented in this work is a Veeco UNI-bulb source and operates with a 13.6 MHz RF source with a maximum output power of 600 W. Nitrogen purity is carefully controlled at 99.99999 purity. After excitation, ionized species in the plasma include N_2^+, N, and N^+, which all contribute to the formation of GaN [59].

Unlike HVPE which a thermodynamically driven process, MBE operates under a surface kinetic limited regime [60]. Adatom surface diffusion and desorption are important parameters during growth and are largely controlled by adjusting the substrate

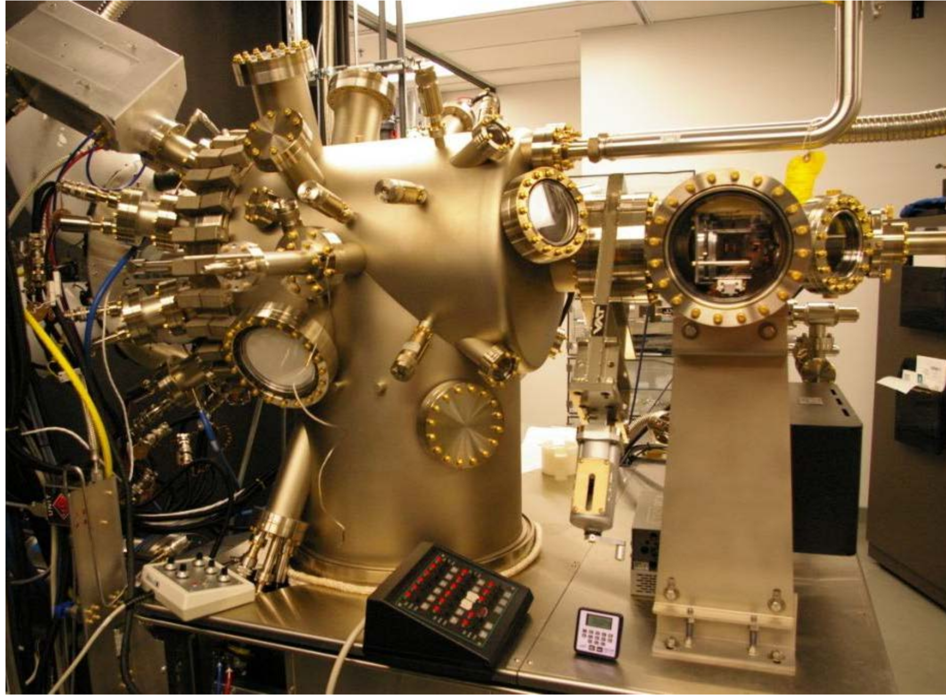

(a)

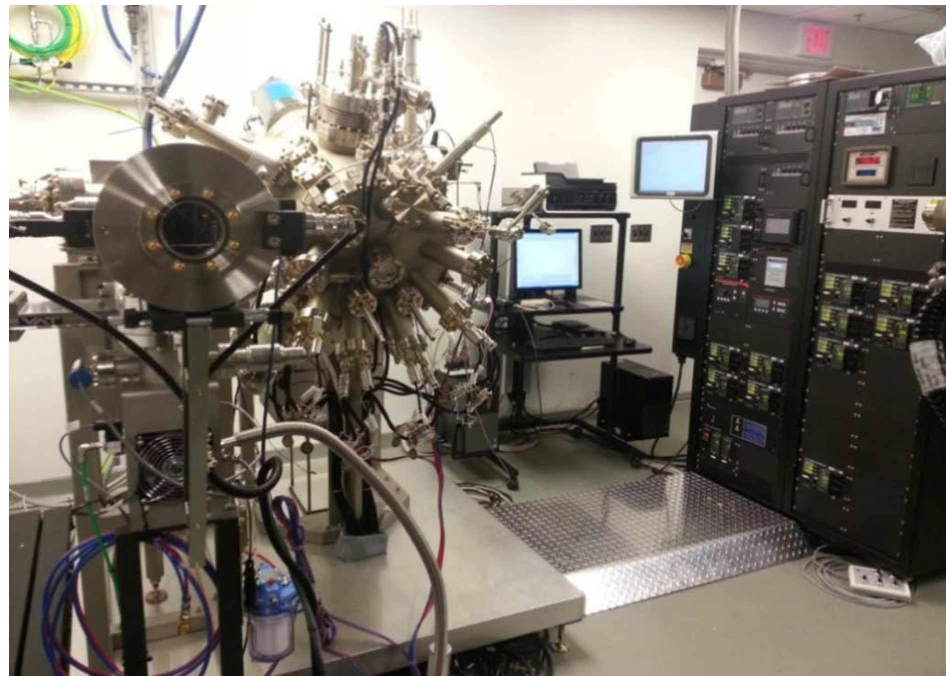

(b)

Fig. 2.1 (a) Veeco Gen II and (b) Veeco Gen 930 systems used for epitaxial growth in the present study.

temperature. It is therefore extremely important to determine the growth temperature accurately. During the low temperature (~500°C) growth of $In_{0.4}Ga_{0.6}N$ and $In_{0.18}Al_{0.82}N$ used in the red-emitting lasers, this becomes more important with the reduced growth window. For the experiments in this work, the substrate temperature is measured with an infrared pyrometer, calibrated by the RHEED transition in Si (111). The RHEED pattern remains 7x7 below 850°C and changes to 1x1 above this temperature. Thermocouple temperatures are calibrated according to this transition. Quoted temperatures throughout this work are calculated through this calibration.

2.3 Stranski-Krastanow Growth of InGaN Islands

InGaN/GaN self-assembled quantum dots have been theoretically predicted and experimentally demonstrated to have superior optical properties compared with InGaN/GaN quantum wells due to their stronger electron-hole (e-h) overlap [19-25]. This results in shorter radiative recombination lifetimes and allows for longer wavelength emission with higher indium composition in the InGaN layer [4-11, 19-25]. These dots form via strain relaxation and have therefor have reduced piezoelectric polarization. Additionally, the physical confinement of carriers in space can prevent carrier leakage and escape to dislocations present in the InGaN layer.

InGaN/Gan quantum dots have been experimentally demonstrated using the Stranski-Krastanow (S-K) growth mode which has been used for the experiments in this work [20-25]. Additionally, they have been demonstrated by low temperature passivation [61], the use of anti-surfactants [62], and post-growth fabrication including quantum size controlled photoelectrochemical (QSC-PEC) etching and site controlled etching [63, 64]. Growth of InGaN/GaN quantum dots has been demonstrated in plasma-

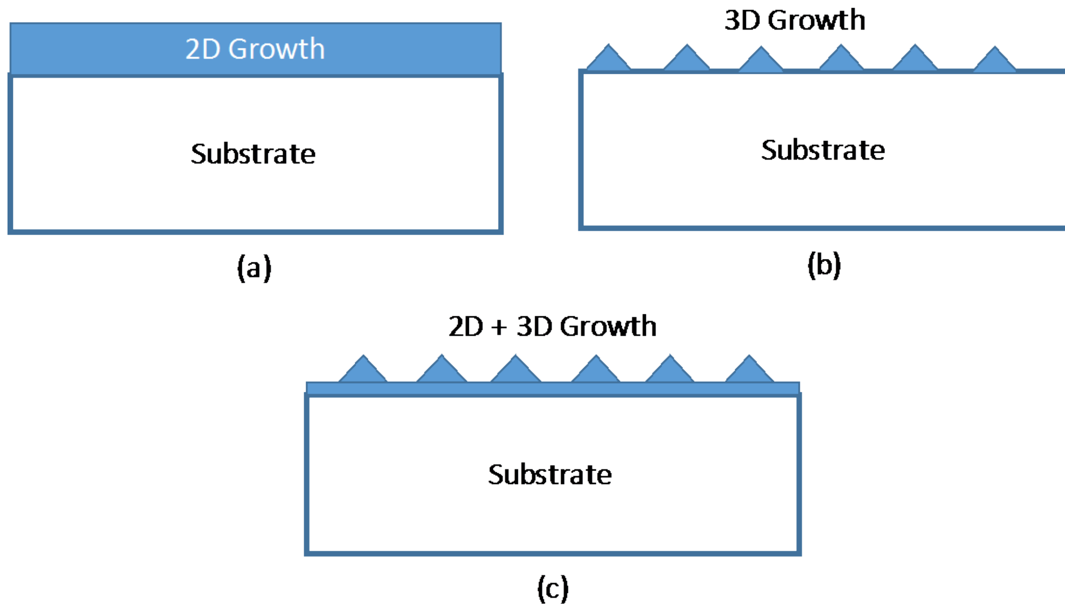

Fig. 2.2 Schematic of different growth modes: (a) Frank-van der Merwe, (b) Volmer Weber, and (c) Stranski-Krastanow.

assited molecular beam epitaxy [20-25, 65], ammonia based MBE [66], and MOCVD [67]. In this work, high performance red-emitting quantum dots are demonstrated by precisely controlling and studying the growth in ultra-high vacuum PA-MBE.

Stranski-Krastanow island growth of self-assembled InGaN/GaN quantum dots can be achieved when a relatively large lattice mismatch exists between the InGaN layer and the underlying layer (usually GaN). Two other growth modes exist including Frank-van der Merwe (FM) and Volmer-Weber (V-W) [68, 69] depending on the lattice mismatch and the interaction strength of the impinging adatoms on the surface. The three growth modes are shown schematically in Fig. 2.2. The V-W growth mode results in the growth of 3-dimensional adatom clusters with the surface and usually occurs when a large lattice mismatch is present (larger than required for S-K growth). This growth mode has recently been shown as the dominant growth mode of high indium content (red-

emitting) InGaN "disks" in GaN nanowires [70]. FM growth results in a layer by layer (planar) growth and can be realized during the growth of lattice matched layers (GaN on GaN or $In_{0.18}Al_{0.82}N$ on GaN). S-K growth exists between these two extremes and is characterized by an initial 2D growth (typically referred to as a wetting layer) followed by 3D island growth.

2.4 Growth and Characterization of Multiple InGaN Quantum Dot Layers

The present study was undertaken with the objective of understanding and optimizing the epitaxy of InGaN/GaN quantum dots for their application in high performance red-emitting lasers. While the growth of In(Ga)As/GaAs quantum dots has

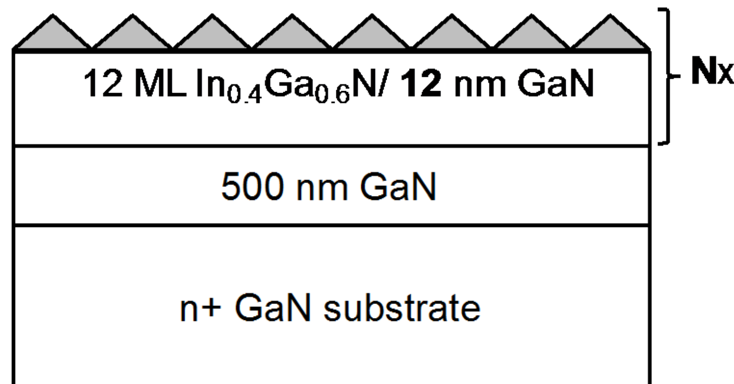

Fig. 2.3 Quantum dot heterostructure used for characterization of the quantum dot layers. The growth was terminated following the growth of N periods of the active region for N varying from one to five.

been widely reported [53-55] and while InGaN/GaN quantum dots have been reported by various groups, [19-23, 64-67], detailed characterization of their growth mode has yet to be reported. In particular, when designing the active region, multiple layers of quantum dots or wells are often incorporated into the laser waveguide. In growing the quantum dot heterostructure, it is often assumed that the layers of quantum dots are identical [19-23]. It is the goal here to determine whether this is a valid assumption.

InGaN/GaN quantum dot (QD) heterostructures were grown by plasma-assisted MBE (PA-MBE) on GaN-on-sapphire substrates. A detailed description of the sample preparation prior to their introduction into the MBE system has been described in Appendix A. An undoped GaN buffer layer of 500 nm thickness is first grown at 710°C with a Ga flux of 2.2×10^{-7} Torr and with 0.66 sccm of ultra-high purity N_2 with a plasma source power of 350W. InGaN/GaN quantum dots for this study are then grown at 540°C under nitrogen-rich conditions (1.33 sccm/420W N_2 plasma power). A variable number of dot layers with varying thickness and GaN barriers of varying thickness are grown, usually with an interruption after the growth of a dot layer. Nominal values of In and Ga fluxes for an In composition of 40% in the QD are 9×10^{-8} and 4×10^{-8} Torr, respectively. The average alloy composition in the QD along the c-axis is measured by energy dispersive X-ray spectroscopy on a suitably prepared transmission electron microscopy (TEM) sample, which shows a variation in the alloy composition along the c-axis with a maximum In content of ~40% for red-emitting QDs and has been discussed in detail in section 2.7. The composition measured by X-ray diffraction in a relaxed bulk layer with the same nominal composition is similar.

Multiple dot layers are usually grown in the active region of lasers to maximize the optical gain and mode confinement factor. We therefore investigated the growth mode of multiple dot layers. Single or multiple $In_{0.4}Ga_{0.6}N$/GaN dot layers were grown under the conditions described above with a GaN barrier thickness of 12 nm and a nominal InGaN thickness of 12 monolayers (ML), as shown schematically in Fig. 2.3. Unlike what is observed during the growth of InGaAs quantum dots [71], it is found by atomic force microscopy (AFM) that the first layer of QDs has a smaller dot density

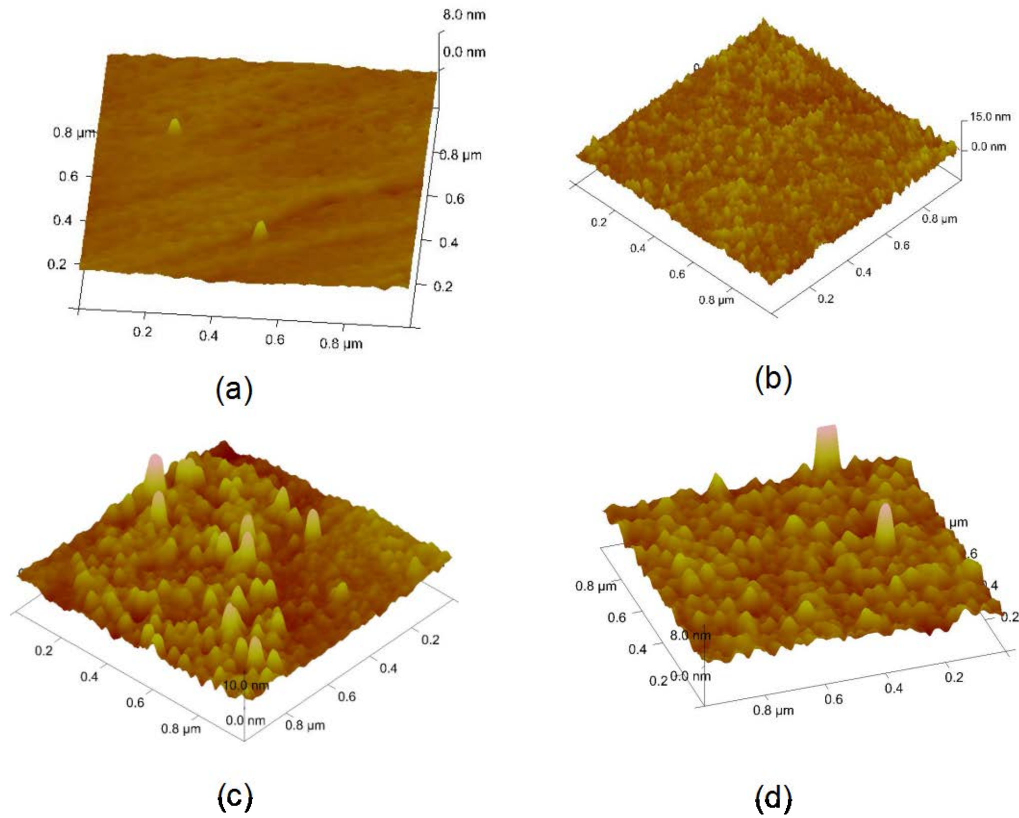

Fig. 2.4 Atomic force microscopy images of uncapped layers of quantum dots. The heterostructure is shown schematically in Fig. 2.3. The values of N are (a) 1, (b) 2, (c) 3, and (d) 4.

(~$7\text{x}10^{7}$ cm^{-2}), which increases in the second layer and remains relatively constant at $5\text{x}10^{10}$ cm^{-2} in the third and higher layers. AFM images from the first four layers are shown in Fig. 2.4. The increase in dot density can clearly be observed in these images with the lowest density in the first layer. These images have been analyzed in terms of the dot sizes and densities. The dot height and density is shown quantitatively in Fig. 2.5. The dot height follows a trend very similar to that seen in the aerial densities with an increase from the first to third layer, followed by a saturation of the height. Interestingly, the dot base width is roughly constant in all these sample. The average base width under

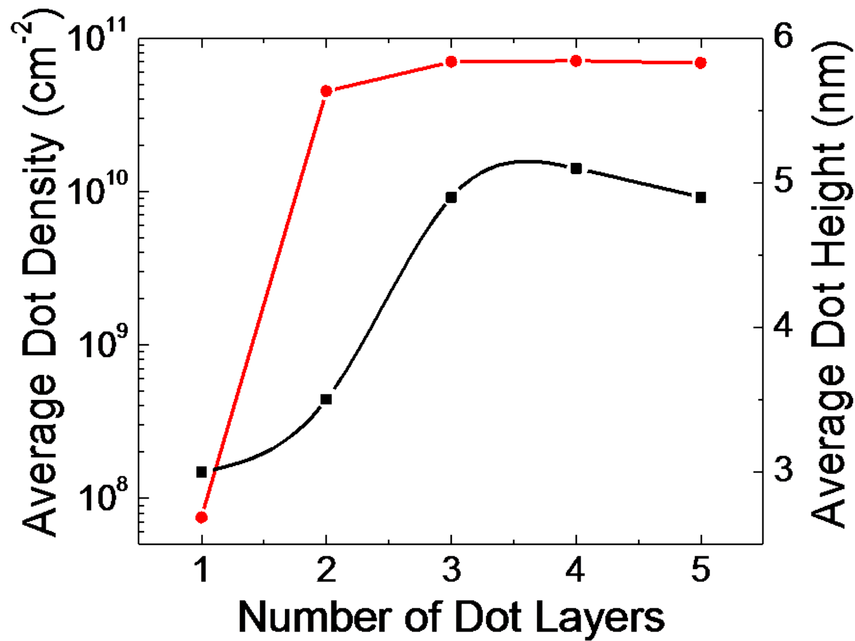

Fig. 2.5 InGaN island height and aerial density from the AFM imaging on the samples described in Fig. 2.3.

these growth conditions is 37 nm, with a variation of 5 nm. The change in island density from the first quantum dot layer to the second can be understood by considering how In surface segregation impacts the critical thickness for island nucleation in these layers. The resulting composition profile can be understood following the work of Dehaese [72], and is schematically shown in Fig. 2.6 (a) for a multi-dot layer structure. The composition increases exponentially towards the intended composition x_{max} during the growth of the quantum dot layer, and decays exponentially during the growth of the barrier layer. If the segregation energy is large, it is possible that the composition does not reach x_{max} in the first layer of dots. However, the excess In is available to be incorporated as the film continues to grow, such that x_{max} will be reached in subsequent layers. Similarly, some In incorporation is expected in the barrier layers. In general, the critical thickness is defined as the thickness of the film that grows via a layer-by-layer

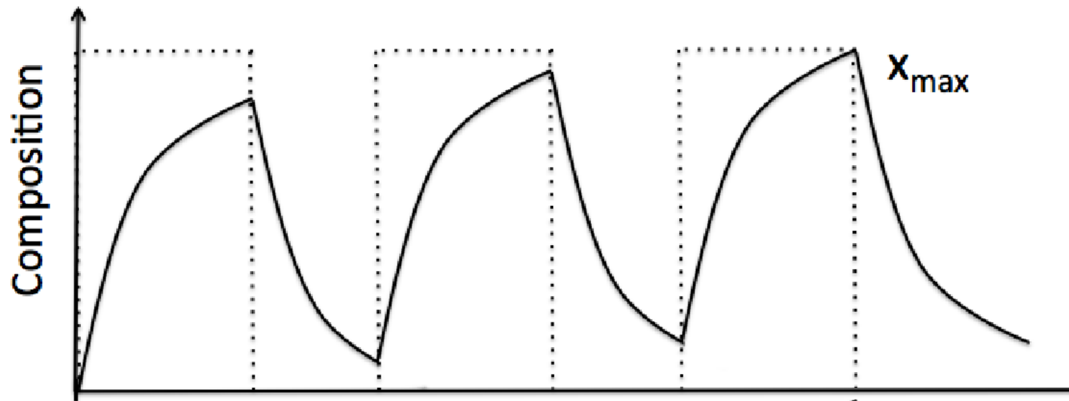

(a)

Fig. 2.6 Schematic of compositional variation of the dot growth along the c-axis plotted alongside the intended distribution (dashed line).

mode prior to the formation of 3D islands, assuming constant x. When x is not constant, as is the case here, it is more appropriate to consider the critical strain energy for island nucleation, U_{cr}. The strain energy is proportional to f^2h, where f is the misfit strain and h is the thickness of the film. Because the strain depends linearly on the composition x, the strain energy can be written as $[x(h)]^2h$, where x is now a function of h. Fig. 2.6 (b) shows a plot of the strain energy as a function of thickness for the multilayer structure. The critical thickness is greatest for the first quantum dot layer. Consequently, the first layer of dots requires more deposited material to reach U_{cr} than do subsequent layers. Since each layer is exposed to the growth flux for the same amount of time, the first layer

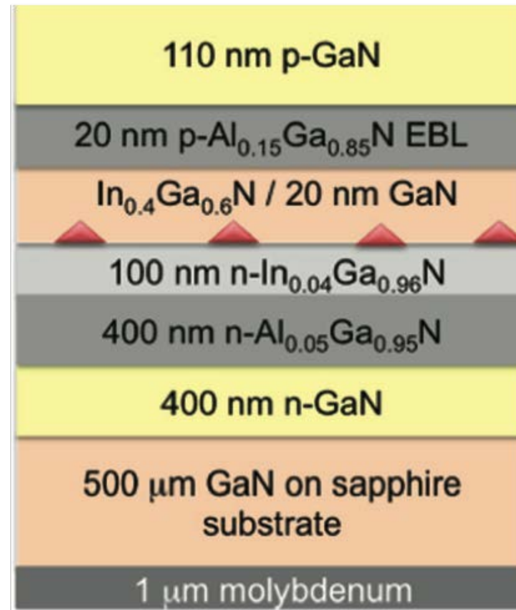

Fig. 2.7 Schematic of a single photon source using a single layer of the low density InGaN/GaN quantum dots. With an aerial dot density of $<10^8$ cm^2 and an aperture ~1μm^2 (which can be defined with standard photolithography) emission from a single dot can be collected [73].

of dots has a shorter amount of time over which the islands grow. The island density is proportional to the product of the island growth time and the nucleation rate. Thus, the first layer will have a lower island density assuming that the nucleation rate is constant.

The relatively low density of quantum dots on the first layer has several important consequences on heterostructures which incorporate these dots into the active region. First, the very low fill factor will result in negligible contribution of this first layer to the modal gain of the laser, which is a product of the material gain and the optical confinement factor. The optical confinement factor itself can be considered to be a product of the transverse confinement factor, Γ_z, and the in-plane confinement factor, Γ_{xy}. Due to the relatively large dimensions in the in-plane direction, individual modes are not considered, and instead Γ_{xy} can be taken as the physical fill factor of the active material in

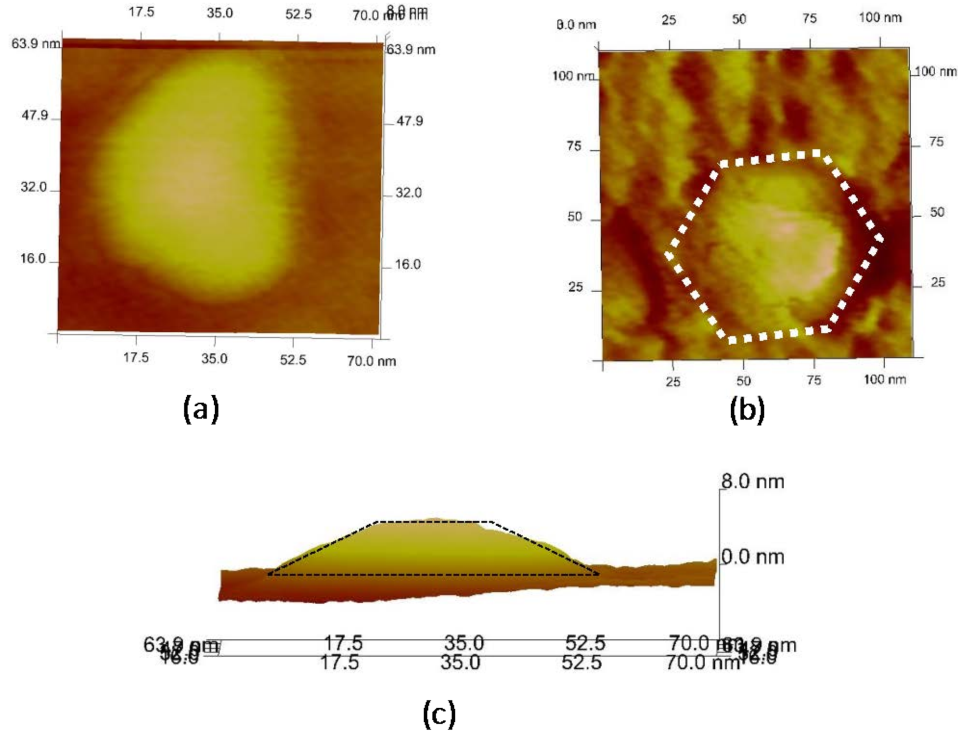

Fig. 2.8 Atomic force microscopy images of the single dots in Fig. 2.4(a). The dots generally form a truncated hexagonal pyramid. In some of the dots (a), the island may be elongated and not a regular hexagon.

plane. Calculation of optical modes and Γ along can be accomplished using the transfer matrix method, shown in Appendix D.

While the first layer provides minimal contribution to the modal gain, it can be used in other applications including in single photon sources which have recently been reported [73], and shown schematically in Fig. 2.7. With the low density of quantum dots in the first layer, a single dot can be optically isolated with an aperture of ~ 1 μm^2, easily defined by standard photolithography. Additionally, due to the low density, individual dots can be imaged by AFM, which are shown in Fig. 2.8. Fig 2.8 (a) and (b) show plan view image of the two dots in Fig. 2.4 (a). Clear hexagonal symmetry can be observed in these dots. However, the dots are sometimes elongated in 1 direction. Further analysis

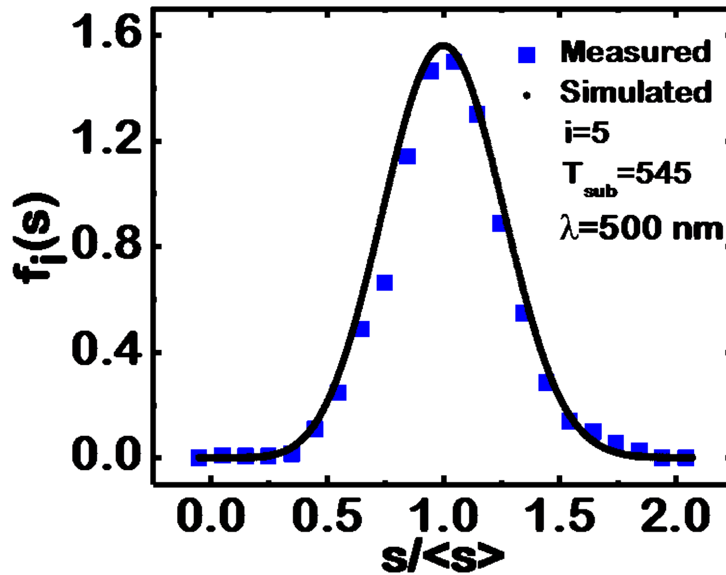

Fig. 2.9 Distribution of InGaN island heights for typical red-emitting quantum dots. The solid line is the best fit of the scaling function to the measured AFM data.

will need to be done to determine the facets of these dots and the direction of the elongation. A side view of an InGaN island is shown in Fig. 2.8(c), revealing the dots grow into a truncated pyramid.

It is also observed that growth of the QDs follows a kinetics driven scaling law, in accordance with the observations made by Amar *et. al.* [60]. Under this kinetically driven growth model, adatoms on the surface may not reach their thermodynamically favored state and instead are limited by the amount of kinetic energy and mobility they have on the surface to be incorporated into the lattice. Under this model, island formation and stability will be determined by the size of the island. Smaller islands will be relatively unstable with fewer bonds. At some critical island size, given by i, dots will be typically stable. Figure 2.9 shows the lineshape, or scaling, function of the size (height) distribution for InGaN/GaN dots grown at 545°C, measured by AFM. The data obtained

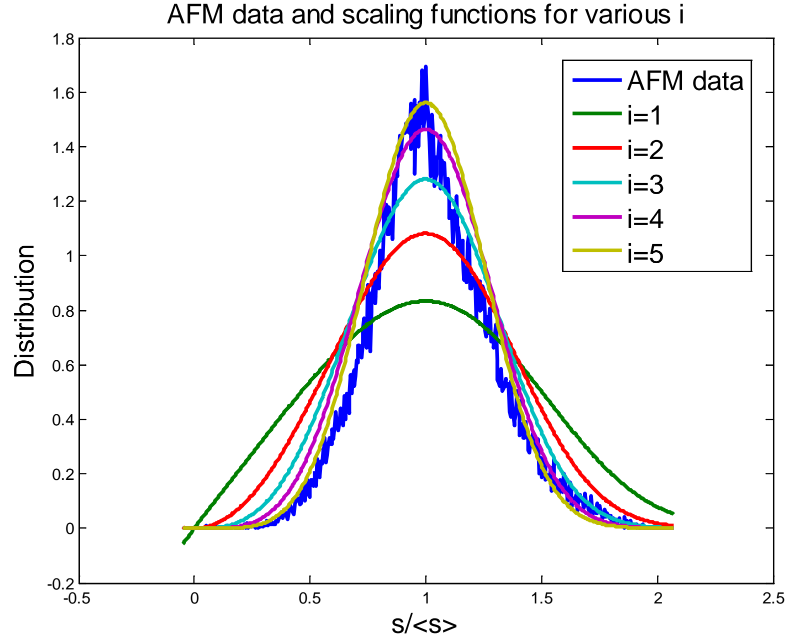

Fig. 2.10 Scaling functions showing the best fit to this data is i=5 at a growth temperature of 545ºC. Note that a higher value of i means higher uniformity.

from the top layer of a 7-layer stack have been analyzed with the scaling function $f_i\left(u=\frac{s}{<s>}\right)=\frac{N_s(\theta)<s>}{\theta}=C_i u^i \exp\left(-i a_i u^{\frac{1}{a_i}}\right)$, where N_s is the size distribution, s is the island size, θ is the coverage. It is found that the value of i increases from 3 to 5 with increase of substrate temperature from 440ºC to 545ºC [17,]. For comparison, AFM data in relation to several of these scaling functions is shown in Fig. 2.10. A lower value

of 'i' also implies a less uniform distribution of quantum dots. This may be one limitation on longer wavelength quantum dot devices (beyond red). Sufficient modal gain from a single state may not be reachable unless the uniformity can be increased.

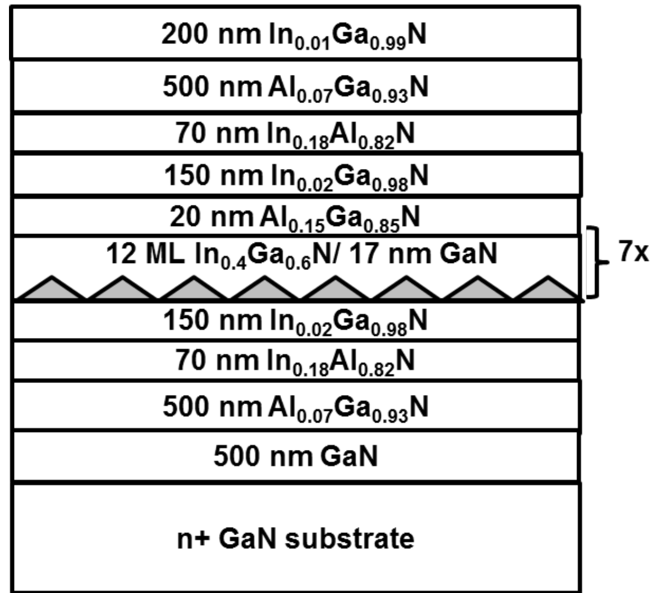

Fig. 2.11 Quantum dot laser heterostructure used for photoluminescence measurements.

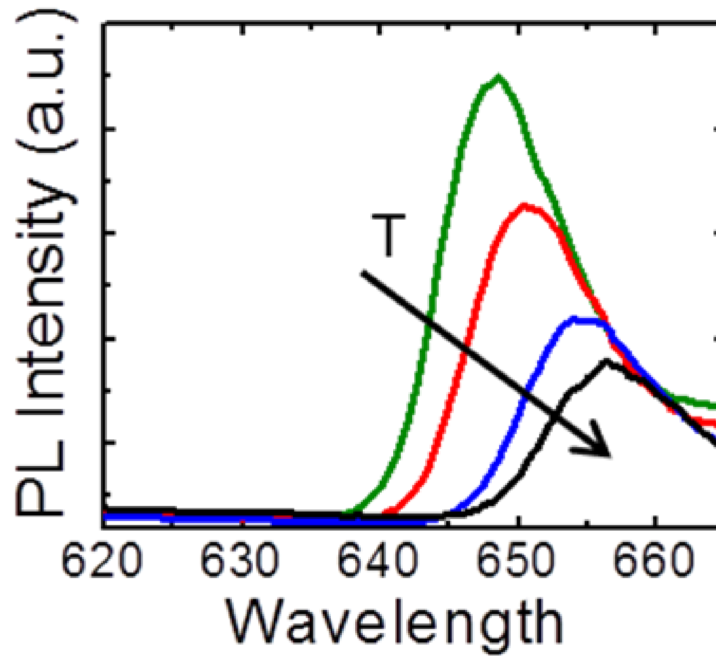

Fig. 2.12 Typical photoluminescence of red-emitting InGaN/GaN quantum dots as a function of temperature.

2.5 Photoluminescence Characterization of Red-Emitting InGaN Quantum Dots

Temperature dependent and time resolved photoluminescence (PL) measurements were made on the QD laser heterostructure, shown in Fig. 2.11, etched down to the p-InGaN waveguide. The etching process was identical to that used during the laser fabrication and is described in detail in Appendix B, step 2. The samples were mounted in a closed loop He cryostat and excited non-resonantly by a frequency tripled

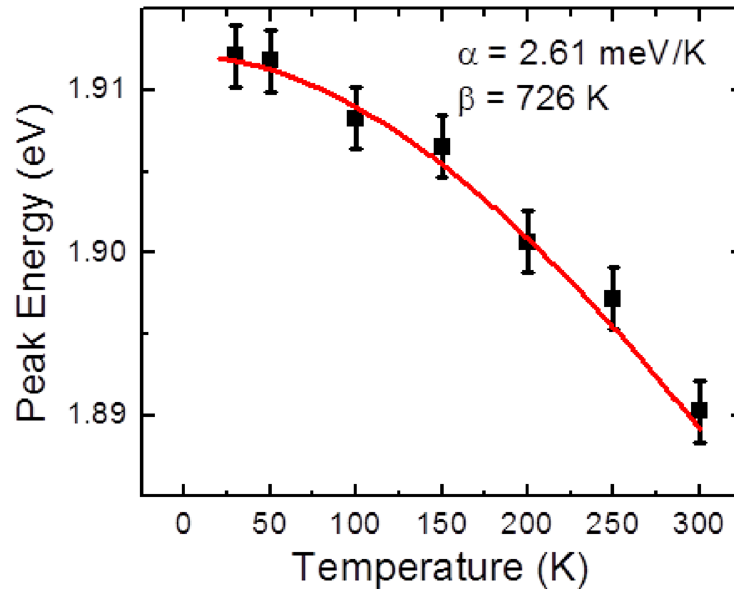

Fig. 2.13 Variation of peak emission energy from the red-emitting $In_{0.4}Ga_{0.6}N$/GaN quantum dots as a function of temperature. The red line is a fit to the data with the Varshni relation for the given values of α and β.

Ti:Sapphire laser (hυ=4.66 eV). A detailed schematic of the time-resolved and temperature dependent photoluminescence setup is shown in Appendix C. Temperature dependent PL spectra (from 30 K to 300 K) are shown in Fig. 2.12. The peak energy in the PL spectra closely follows the Varshni equation [74] with increasing temperature, shown in Fig. 2.13 where no clear "S-shaped" behavior is seen [75-76]. In quantum

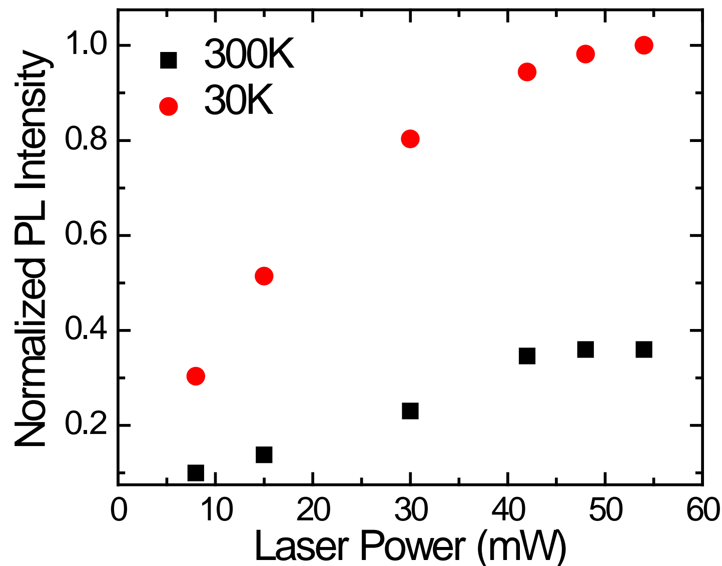

Fig. 2.14 Normalized integrated photoluminescence intensity as a function of excitation power and temperature. The quantum efficiency of 35.9% is derived by taking the ratio of the intensities under saturation.

wells, due to potential fluctuations, carriers first recombine in the lowest potential (with the highest indium concentration). As the temperature is elevated, the carriers can thermally escape into the lower indium regions leading to an initial increase of the emission energy. As the temperature is further raised, a typical shrinkage of the material bandgap in accordance with the Varshni relation is observed. This “S-shaped” behavior is therefore typically associated with indium clustering and non-uniformity. The quantum dots, lacking this behavior, are likely free of indium clustering.

The temperature-dependent measurements were made as a function of the incident excitation power and the variation of integrated intensity with excitation power is shown in Fig. 2.13. In the nitride material system, due to the large polarization field for c-plane growth, it becomes essential to measure η_i at high injection for which the dots (or wells)

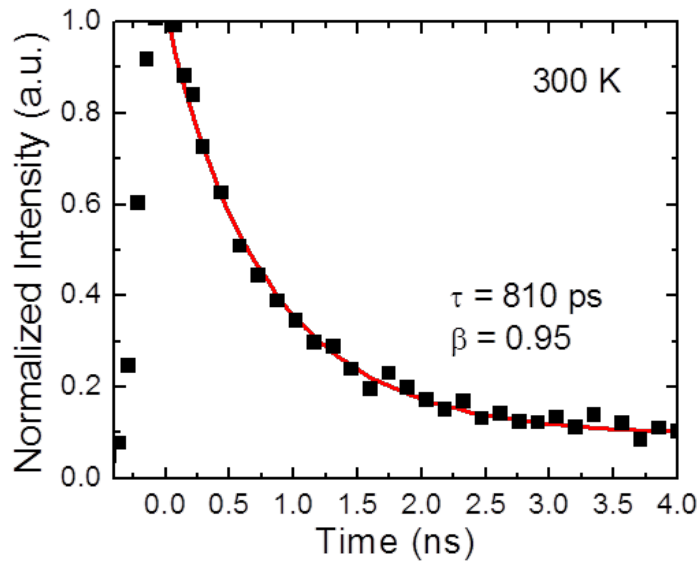

Fig. 2.15 Photoluminescence decay transient at room temperature.

reach flat band condition and the polarization field is screened. As reported in the literature [77-79], at low temperatures injected carriers are confined in the localization potential of the quantum dots or in the potentials due to compositional fluctuations (in quantum wells). With increasing temperature, the carriers acquire sufficient energy to overcome the potential barriers and recombine at non-radiative centers in the barrier and wetting layer regions. Then the ratio of the saturated peak PL intensity at 30 and 300 K at high excitation powers is an approximate measure of the internal quantum efficiency, η_{i} - (at room temperature). The thermionic emission of carriers and recombination in other layers at elevated temperatures may result in an underestimation of η_i. However, by measuring the dots at high excitation where the dots are saturated with carriers, this effect should be minimized. From the data shown in Fig. 2.14 a value of η_i = 35.9% is derived. This value of ~36% is typical across red-emitting quantum dot samples with similar growth conditions.

2.6 Time Resolved Photoluminescence

In order to determine the radiative and non-radiative lifetime of carriers in the dots at room temperature, we have performed time-resolved PL (TRPL) measurements using a single-photon detector and a high-resolution monochromator schematically shown in Appendix C. The transient data at room temperature, shown in Fig. 2.15, was analyzed with the stretched exponential model:

$$I = I_0 \exp\left(-\left(\frac{t}{\tau}\right)^{\beta}\right) \tag{2.1}$$

where τ is the lifetime and β is the stretching parameter. Values of τ and β = 810 ps and 0.95, respectively, are derived. This value of β suggests a small polarization field and non-uniformity in the dots. A large polarization field in quantum wells leads to a reduction in the electron/hole (e/h) wavefunction overlap at elevated temperatures leading to a reduction in the carrier lifetime at high injections. As the carriers deplete, the lifetime gradually becomes longer, leading to a value of β less than 1. Similarly, non-uniformity of the indium composition would lead to a changing lifetime as the carriers first deplete the regions with shorter lifetime (larger e/h overlap). From the measured τ and η_i, values of the radiative and non-radiative lifetimes are calculated to be 2.2 ns and 1.3 ns respectively at room temperature using:

$$\frac{1}{\tau} = \frac{1}{\tau_r} + \frac{1}{\tau_{nr}} \tag{2.2}$$

$$\eta_{IQE} = \frac{I(T)}{I(30K)} = \frac{1/\tau_r}{1/\tau_r + 1/\tau_{nr}} \tag{2.3}$$

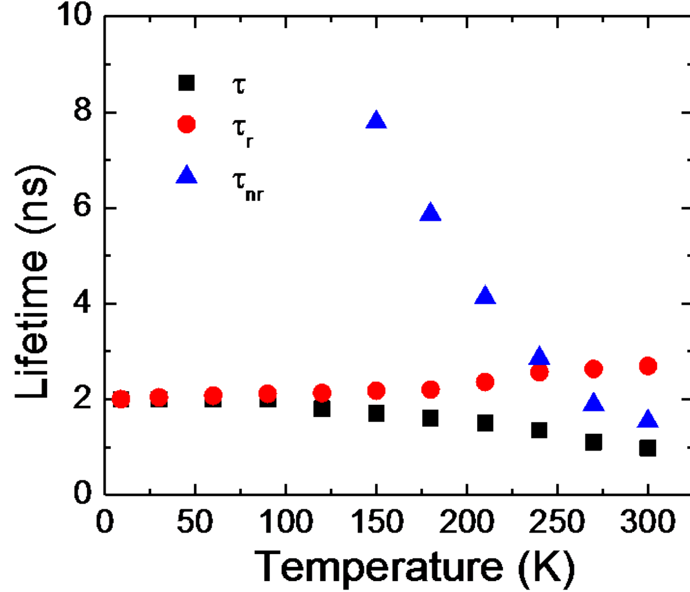

Fig. 2.16 Change of carrier lifetimes in $In_{04}Ga_{0.6}N$ quantum dots as a function of temperature.

While these are favorable characteristics of the quantum dots, their internal quantum efficiency is still relatively low. A detailed investigation is necessary to establish the non-radiative recombination pathways, which could be sub-bandgap defect states from edge dislocations, screw dislocations causing preferential localization of one carrier type, and trap states resulting from point or QD heterointeface defects. Optimization of the quantum dots to improve the efficiency are discussed in chapter 4.

The temperature dependence of the lifetimes is shown in Fig. 2.16. Interestingly, an increase in the radiative lifetime is observed with temperature. This is similar to the trends in In(Ga)As/GaAs quantum dots [80]. Additionally, the carrier transients can be spectrally resolved, shown in Fig. 2.17 by measuring the transients as a function of energy. Several features of note are evident in these spectra. First, any yellow band in the spectra occur in tandem with the GaN recombination, suggesting deep levels

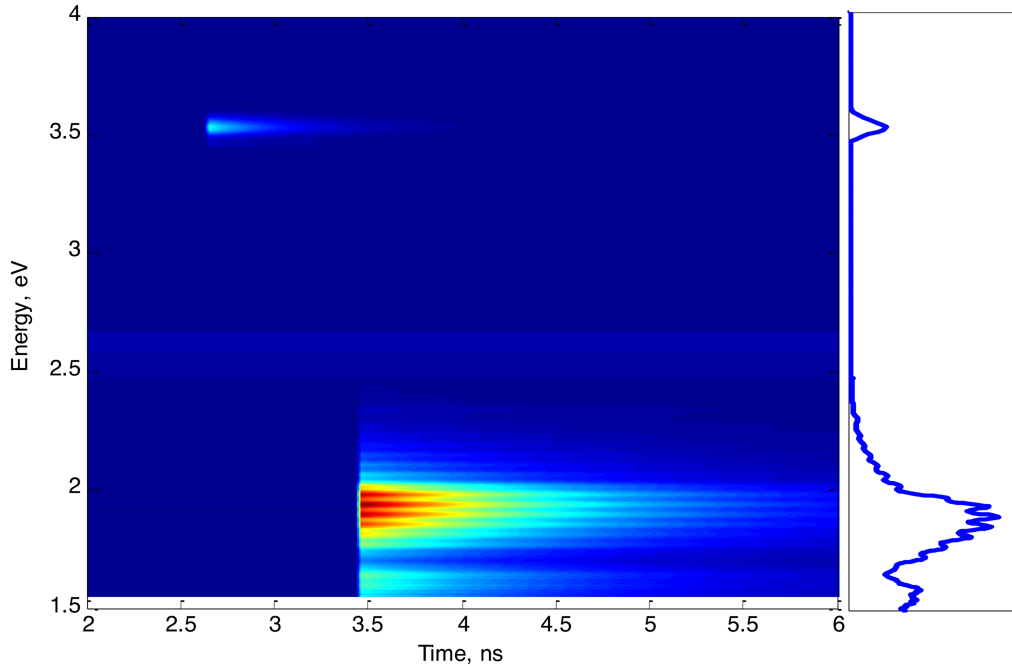

Fig. 2.17 Spectrally resolved photoluminescence transients showing a distinct delay between the GaN and InGaN emission (at 98 K).

corresponding to this state occur in the GaN barrier and substrate and not in the active quantum dots. This may be why yellow band emission is not typically observed in an electrically injected device where the carriers may be trapped in the deep potential barriers of the InGaN layers. Second, the InGaN emission occurs following the GaN emission by a distinctive delay. The variation in this delay with temperature are shown in Fig. 2.18. The increase of radiative lifetime with increasing temperature has been previously observed in InGaAs/GaAs self-organized QDs. The anomalous behavior was explained by invoking electron-hole scattering, instead of phonon scattering, as the dominant mechanism to cool high energy electrons to the ground state [80]. The electron states in the QDs are discrete in contrast to other systems, and the separation between them can exceed the LO phonon energy (phonon energies of InN : 86 meV and GaN : 91

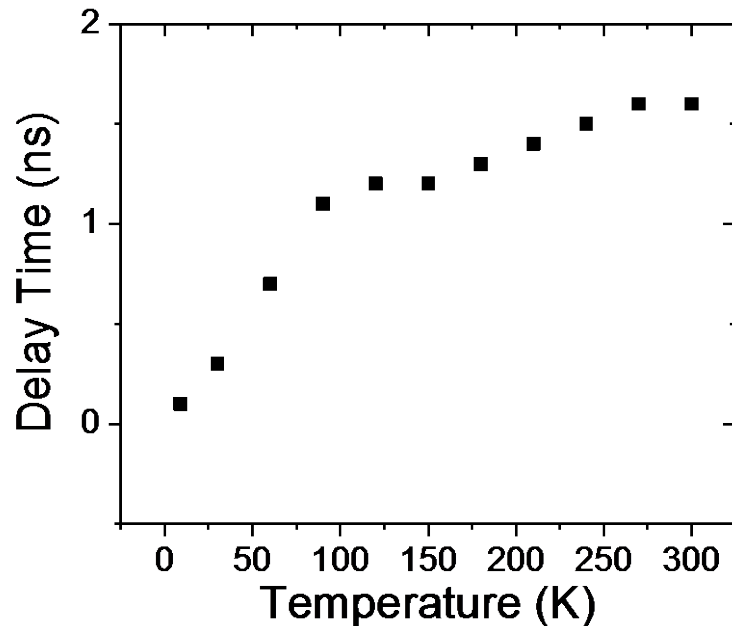

Fig. 2.18 Variation of the time delay between the GaN and InGaN emission as a function of temperature, determined by time resolved photoluminescence.

meV), presenting a phonon bottleneck. In contrast, there is a continuum of hole states due to degeneracy and band mixing. Occupation of the low-lying electron states, which participate in the luminescence process, depends on electron-hole scattering and hole occupation of the ground state. In electron-hole scattering (shown schematically in Fig. 2.19) at low temperatures, hot electrons scatter with cold ground state holes and relax to the ground state. The energy gained by the holes excites them to higher levels, from which they can relax rapidly by multi-phonon emission. With increase of temperature the thermal excitation of cold holes from the ground state will leave fewer holes to scatter with hot electrons and the rate of electron-hole scattering and electron relaxation to the ground state decreases. This results in an increase of the radiative lifetime. The same processes are likely operative in the InGaN/GaN self-organized QDs and in the InGaN/GaN DINWs wherein quantum dot-like self-organized islands are formed.

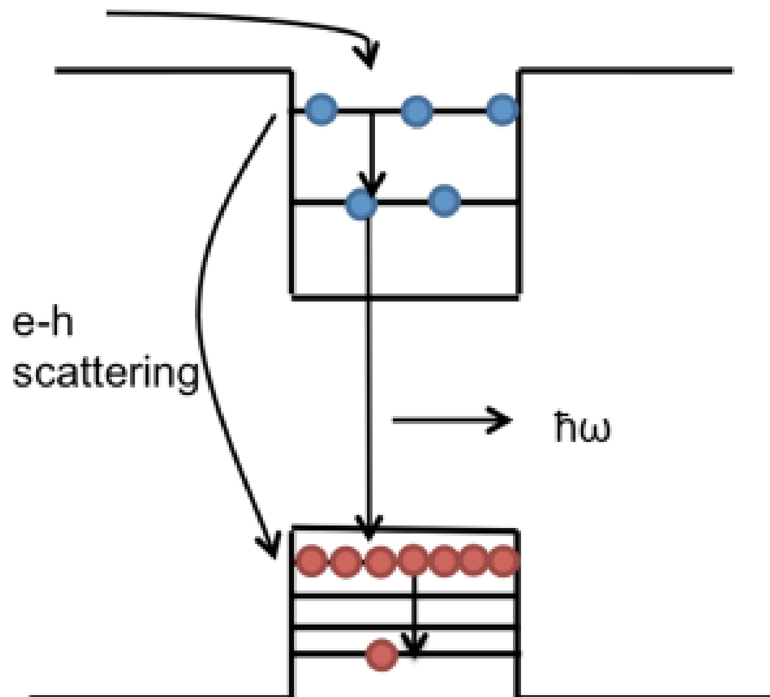

Fig. 2.19 Electron states are discrete and may be separated by energies unobtainable from phonons. Scattering with cold holes is required for electrons to relax into the ground state. This process becomes less efficient at higher temperatures as the supply of cold holes is reduced.

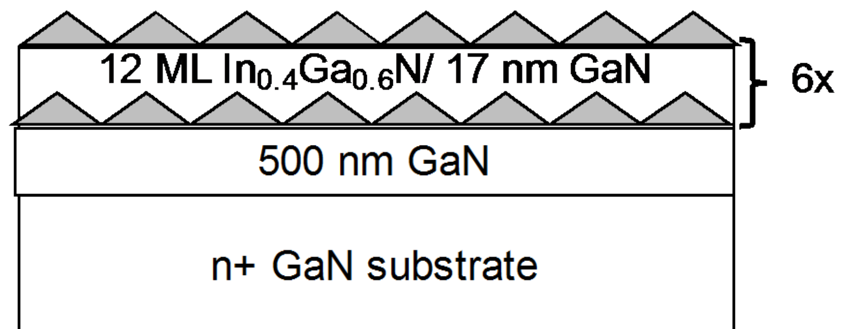

Fig. 2.20 Quantum dot heterosturcture used for structural characterization in section 2.7.

2.7 Structural Characterization of Red-Emitting InGaN/GaN Quantum Dots

The quantum dot heterostructures for structural characterization were grown on bulk c-plane n-GaN substrates (grown by HVPE), shown schematically in Fig. 2.18. A 300 nm thick n-doped (5 x 10^{18} cm^{-3}) GaN buffer layer was grown at 710°C at a flux of 4.5 nm/min. The growth was done under metal rich conditions with periodic (every 10 minute) growth interruptions to prevent metal build up on the surface. The growth temperature was calibrated by the (1x1) to (7x7) RHEED transition in silicon. Seven periods of $In_{0.4}Ga_{0.6}N$ quantum dots/ GaN barrier layers, emitting at at λ=630 nm were grown at a substrate temperature of 540°C under nitrogen rich conditions at equivalent pressures of Φ_{Ga}: Φ_{In} ~ 1:2 and at a growth rate of 0.5 Å/s. An AFM image from an uncapped quantum dot layer (layer 7), is shown in Fig. 2.21, showing the InGaN QD surface morphology. From this data the average dot diameter and height are estimated to be 37 nm and 5 nm, respectively, showing that the final layers follow the size of the 3rd

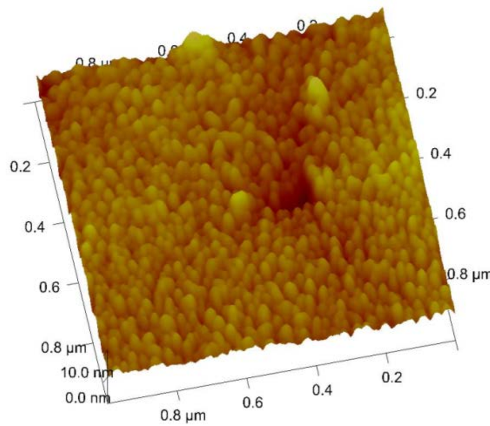

Fig. 2.21 AFM from the uncapped seventh layer of $In_{0.4}Ga_{0.6}N$ quantum dots.

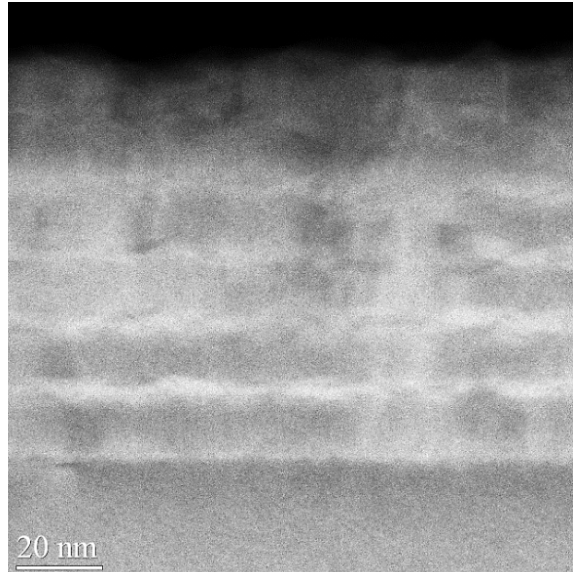

Fig. 2.22 Annular dark field image showing seven layers of $In_{04}Ga_{0.6}N$ quantum dots.

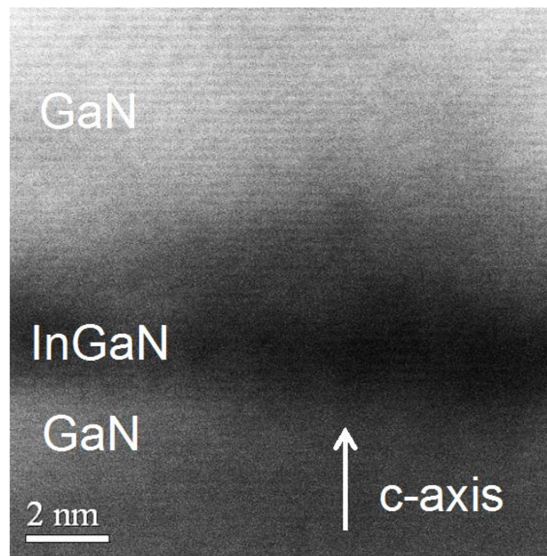

Fig. 2.23 Annular bright field image of a single $In_{04}Ga_{0.6}N$ quantum dot.

and 4th layer. To estimate the fill factor of the quantum dots, the pyramidal dots with base width of 37 nm and height of 5 nm are modeled as equivalent flattened cubes of the same volume and base width and with a 3.55 nm effective height. Comparing the volume of an array of the dots with the volume of the nominal thickness of the deposited InGaN (12 ML) given by the change in reflective high energy electron diffraction (RHEED) from

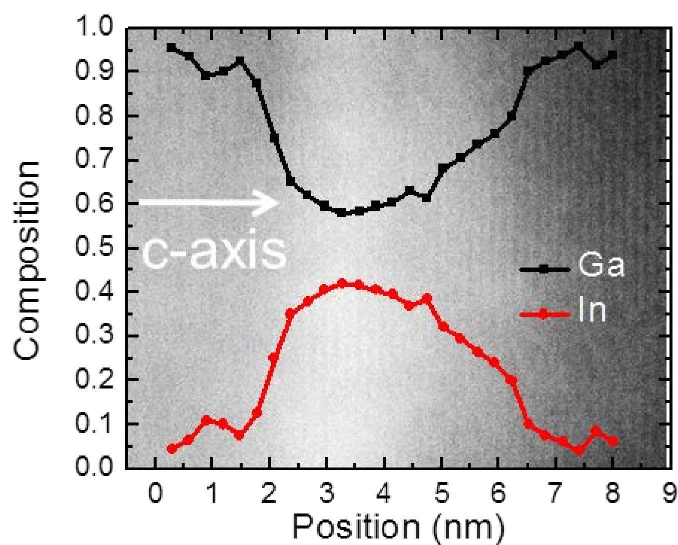

Fig. 2.24 Variation in the In and Ga compositions measured by energy dispersive x-ray spectroscopy. The underlying image is the annual dark field image of the dot from Fig. 2.22.

2D to 3D growth results in a fill factor of 0.35. More detailed structural characterization of the quantum dot layers in the laser heterostructure was undertaken by cross-sectional transmission electron microscopy (TEM). Figure 2.22 shows an annular dark-field TEM image of multiple InGaN QD layers separated by GaN barrier layers. A high resolution scanning transmission electron microscope (STEM) image of a single $In_{0.4}Ga_{0.6}N$ quantum dot with GaN barrier layers is shown in Fig. 2.23. Growth takes place along the c-axis and the perfect crystalline structure is evident. The pyramidal geometry of the dot and wetting layer are evident in this image. The InGaN/GaN interfaces are smooth and apparently free of stacking faults. The average alloy composition in the InGaN dot along the c-axis was measured by energy dispersive X-ray spectroscopy (EDX) with a resolution of 0.3 nm. The result is shown in Fig. 2.24. There is a variation in alloy composition along the c-axis with a maximum In content of 40%.

2.8 Summary

A detailed investigation into the growth of InGaN/GaN self-assembled quantum dots has been discussed. Emission into these long wavelengths, combined with previously demonstrated green- and blue-emitting quantum dots will allow for full color InGaN based displays and projectors. Indium segregation along the c-axis is found to play an important role in the formation of the InGaN islands. A relatively low density on the first quantum dot layers is useful for single photon applications, but will reduce the modal gain in lasers and require the growth of one more layer than desired. The quantum dots have been found to follow a scaling distribution, confirming the kinetically driven growth mode, typically found during MBE growth.

Optical and structural characteristics from a seven-layer stack of quantum dots have also been presented. The quantum dots have an internal quantum efficiency of 35.9% and a radiative lifetime of 2.2 nanoseconds. Temperature dependent photoluminescence follows a Varshni-like relation and the photoluminescence transient follows a nearly mono-exponential decay, indicating the dots are relatively free of clustering or other effects.

Chapter III

Incorporation of InAlN Cladding Layers in the Design of Red-Emitting InGaN/GaN Quantum Dot Lasers

3.1 Introduction

The demonstration of quantum dots with emission covering the entire visible spectrum is important for many applications including solid state lighting [1, 2]. Current white light emitting diodes typically incorporate blue-emitting InGaN/GaN quantum wells and rely on a phosphor to covert some of the blue light to yellow or red. Tuning of the white emission requires the development of new phosphors with the desired emission characteristics. Alternatively, electrically injected devices incorporating the red-emitting quantum dots described in chapter 2 could be used to directly generate red light, which is tunable by simply changing the indium composition in the dots.

Red-emitting light emitting diodes and lasers are also important for display and mobile projector applications, which require blue- , green-, and red-emitting lasers[1, 2]. InGaN based quantum dots may be used for all these wavelengths, negating the need for the use of multiple material systems in these applications. Blue- and green-emitting lasers can be realized with InGaN/GaN based single or multiple quantum wells [4-11], but red-mitting lasers are typically fabricated using other material systems [16, 17] as red-emitting InGaN/GaN quantum well lasers have yet to be reported. Alternatively,

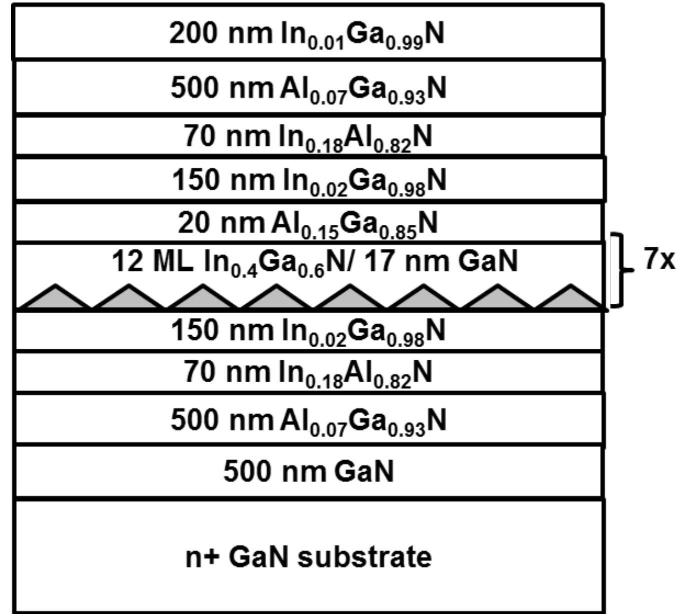

Fig. 3.1 Quantum dot laser heterostructure.

InGaP/InGaAlP double-heterostructure and MQW lasers lattice matched to GaAs and emitting in the red wavelength region of 650-670 nm have been reported [16,17 81-86]. However, these devices are characterized by very large values (5-10 kA/cm^2) and strong temperature dependence (T_0 ~ 50 – 100 K) of the threshold current density. Both of these characteristics are detrimental to real applications. To test the suitability of the red-emitting $In_{04.}Ga_{0.6}N$/GaN quantum dots for these applications, they are incorporated into edge-emitting laser heterostructures. The design, growth, fabrication, and DC characterization of these devices are presented in this chapter. Dynamic characterization including small-signal and large-signal modulation are presented in chapter 6.

3.2 Growth of $In_xAl_{1-x}N$

Ternary $Al_xGa_{1-x}N$ is generally used as the cladding layer in GaN-based laser heterostructures. However, at long wavelengths, due to a reduced refractive index mismatch [87], this cladding can not provide the same optical confinement found at

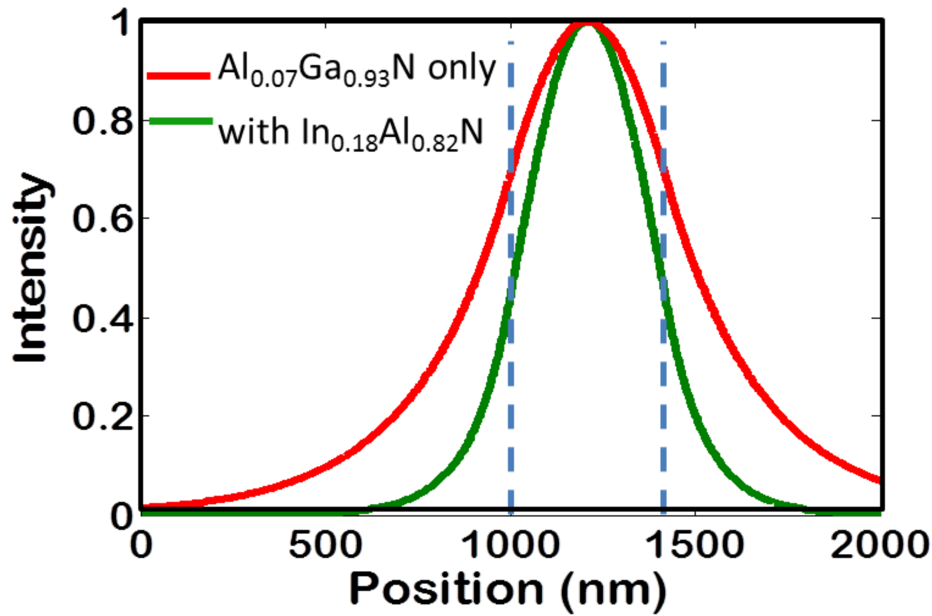

Fig. 3.2 Optical mode profile of the laser heterostructure shown in Fig. 3.1 with and without the incorporation of the $In_{0.18}Al_{0.82}N$ cladding layer.

shorter wavelengths. $Al_xGa_{1-x}N$ cannot be grown sufficiently thick or with sufficient Al composition without the formation of defects, resulting in free carrier absorption and substrate leakage of the optical mode, leading to large cavity loss [21]. To alleviate this problem, we have inserted lattice-matched $In_{0.18}Al_{0.82}N$ layers, which provide a much larger index difference, equivalent to $Al_xGa_{1-x}N$ with a composition of x=46% [21, 81]. This layer has been incorporated into the laser heterostructure, shown in Fig. 3.1, and provides better mode confinement, shown in Fig. 3.2, simulated by the transfer matrix method, as described in Appendix D. For this simulation, the position axis refers to the transverse (growth) direction (c-axis). Modal confinement in the other directions are not taken into account for this simulation. Substantially better modal confinement can be achieved with the incorporation of $In_{0.18}Al_{0.82}N$. Additionally, since it is lattice matched to GaN [20, 81], it can be grown with any desired thickness.

Sample	T (^{o}C)	φ_{In} (Torr)	φ_{Al} (Torr)	Composition (x) $In_xAl_{1-x}N$
a	469	3.50E-08	2.20E-08	0.3
b	510	2.50E-08	3.40E-08	0.14
c	497	2.50E-08	3.40E-08	0.18

Table 3.1 Variation in the growth conditions of InAlN layers.

Due to the low incorporation of indium at high temperatures, the growth must be done at a relatively low substrate temperature while ensuring that temperature is sufficiently high to prevent a rough surface morphology from high aluminum adatom sticking coefficient (~1), and low mobility at reduced temperatures. Another advantage of the relatively low growth temperatures (compared with T_{sub}~740ºC for AlGaN) is the growth of the upper cladding will be done at a temperature lower than the quantum dot growth temperature. This will reduce high temperature annealing and outdiffusion of indium which may prevent the realization of long-wavelength devices. The substrate temperature and indium and aluminum fluxes were varied, as shown in table 3.1. The temperature was varied from (a) 469 ºC, (b) 497 ºC, to (c) 510 ºC. X-ray diffraction rocking curves for the three samples are shown in Figs 3.3 (a), (b), and (c), respectively. Varying the substrate temperature over this relatively small range results in a large increase of indium composition from 14 % (at 510 ºC) to 30 % (at 469ºC). At 497 ºC, lattice matched $In_{0.18}Al_{0.82}N$ can be grown with a smooth surface morphology, shown in the

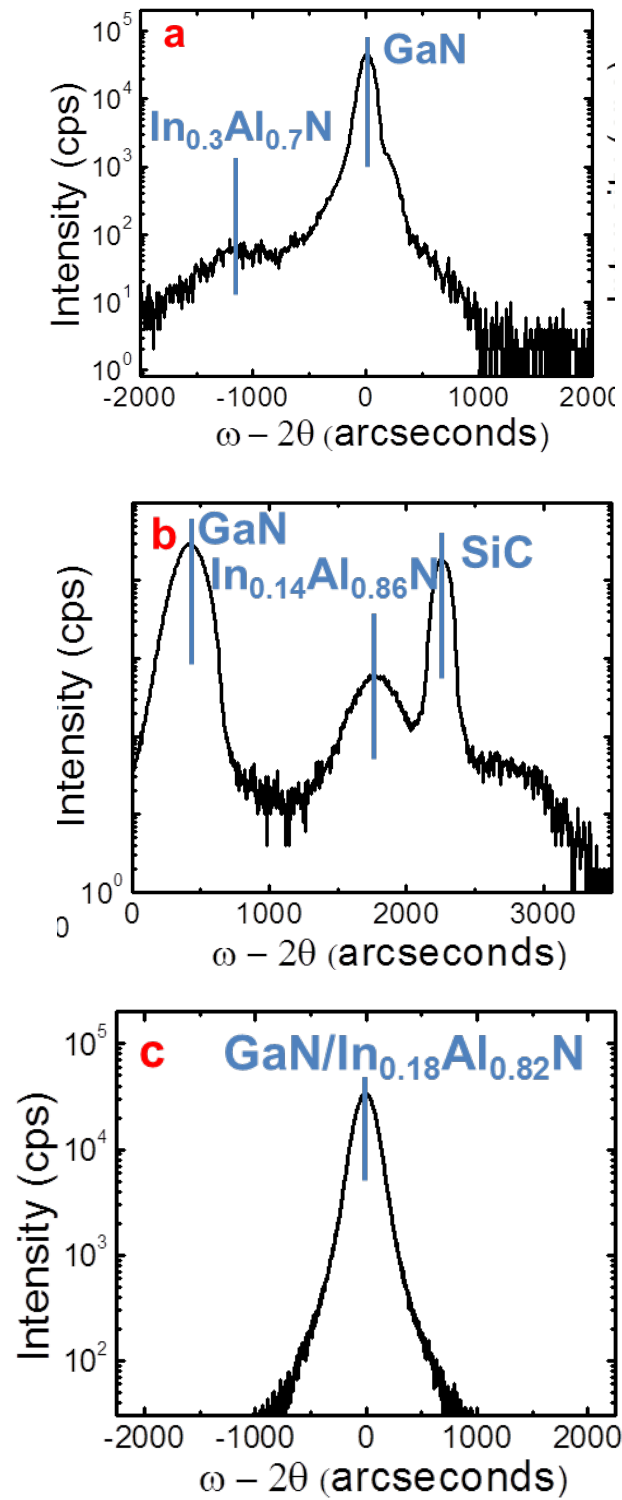

Fig. 3.3 X-ray diffraction rocking curves for InAlN with growth conditions described in table 3.1.

atomic force microscopy image in Fig. 3.4.

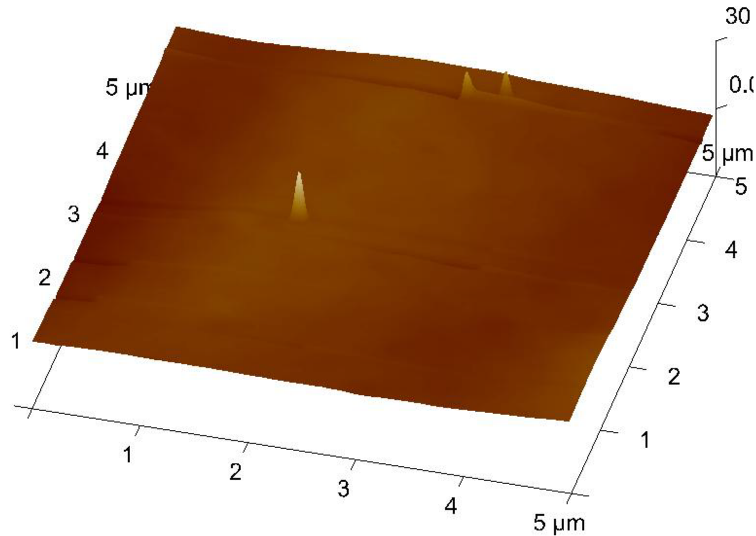

Fig. 3.4 Atomic force microscopy image of lattice matched $In_{0.18}Al_{0.82}N$ on GaN

3.3 InGaN/GaN Quantum Dot Laser Growth and Fabrication

The quantum dot laser heterostructure is shown schematically in Fig. 3.1. It is grown on free-standing c-plane hydride vapor phase epitaxy (HVPE)-grown GaN substrates (defect density ≤ 5 x 10^6 cm^{-2}) by plasma-assisted molecular beam epitaxy (PA-MBE). Description of the sample preparation prior to MBE growth has been described in Appendix A. After cleaning, a 500 nm thick Si-doped n-doped (5 x 10^{18} cm^{-3}) GaN buffer layer was grown at 710°C at a flux of 4.5 nm/min. The growth was done under metal rich conditions with periodic (every 10 minute) growth interruptions to prevent metal build up on the surface. The growth temperature was calibrated by the 1x1 to 7x7 RHEED transition in silicon. Following the growth of the buffer layer, 500 nm of $Al_{0.07}Ga_{0.93}N$ cladding and 70 nm of $In_{0.18}Al_{0.82}N$ are grown at 780°C and 497°C, respectively. An $In_{0.02}Ga_{0.98}N$ waveguide layer was grown at 590°C. These layers (GaN, AlGaN, InGaN,

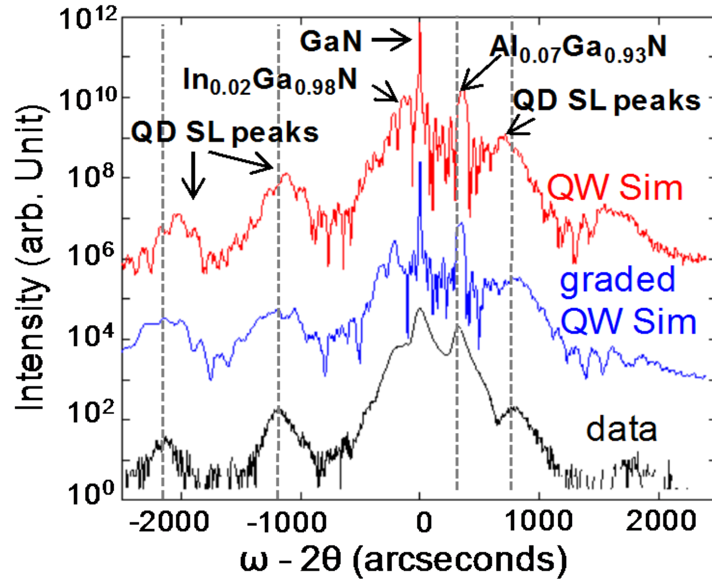

Fig. 3.5 X-ray diffraction rocking curve from the laser heterostructure.

and InAlN) were doped at a concentration of n~5 x 10^{18} cm^{-3} in each layer. Seven periods of $In_{0.4}Ga_{0.6}N$ quantum dots/ GaN barrier layers, emitting at at λ=630 nm were grown at a substrate temperature of 540°C under nitrogen rich conditions at equivalent pressures of Φ_{Ga}: Φ_{In} ~ 1:2 and at a growth rate of 0.5 Å/s. After the growth of the dots, a 20 nm thick Mg-doped p-$Al_{0.15}Ga_{0.85}N$ electron blocking layer was grown at 730°C with a doping concentration of p~6x10^{17} cm^{-3}. A 150 nm p-$In_{0.05}Ga_{0.95}N$ waveguide layer was grown, followed by p-$In_{0.18}Al_{0.82}N$ and p-$Al_{0.07}Ga_{0.93}N$ cladding, grown at 590°C, 497°C and 740°C, respectively, with doping concentrations of 2x10^{17} cm^{-3} in the waveguide and 5x10^{17} cm^{-3} in the cladding layers. Finally, a 200 nm thick p-doped $In_{0.01}Ga_{0.99}N$ layer was grown (p~7x10^{17} cm^{-3}) as the uppermost layer for injections of holes. The composition of the bulk layers were determined by x-ray diffraction, with a typical rocking curve shown in Fig. 3.5. Superlattice peaks from the InGaN/GaN pairs are clearly visible in the black measured data. The red curve is the best fit to the measured data by

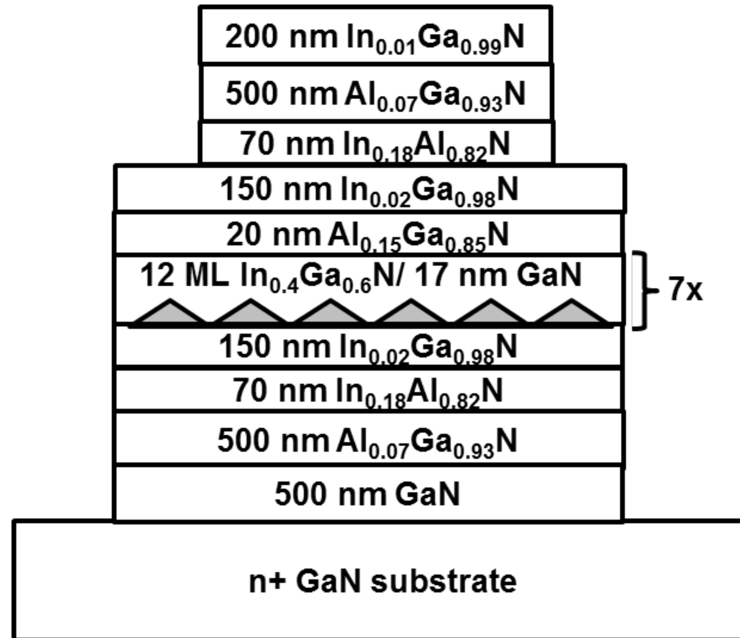

Fig. 3.6 Schematic showing the etched laser heterostructure. The first mesa is etched to the cladding/waveguide heterointerface to minimize scattering.

taking the dots as planar layers (quantum wells) of uniform composition. The fit is done using the structure in Fig. 3.1 and by solving the Takagi-Taupin equations in Jordan Valley RADS software by Prof. Rachel Goldman and Alexander Chang.

The lasers are fabricated in a ridge geometry, shown schematically in Fig. 3.6. A detailed outline of the laser fabrication is listed in Appendix B, but is given here in brief for completeness. The lasers are etched in a two-step mesa to provide optical confinement and to reduce loss from scattering along the sidewall. The p-(Ni/Au 5/200 nm) and n-(Ti/Au 10/200 nm) ohmic contacts are deposited by e-beam evaporation and annealed in an air-ambient at 550°C for 2 minutes. The lasers are passivated with SiO_2 and interconnection pads are deposited for probing the devices. The lasers ridges are aligned along the a-direction and the devices are cleaved along the m-plane to finish the laser cavity. Scanning electron microscopy images of the fabricated lasers are shown in Fig.

3.7. High-reflectivity dielectric (SiO_2/TiO_2) distributed Bragg reflectors (DBRs) are deposited on the two facets.

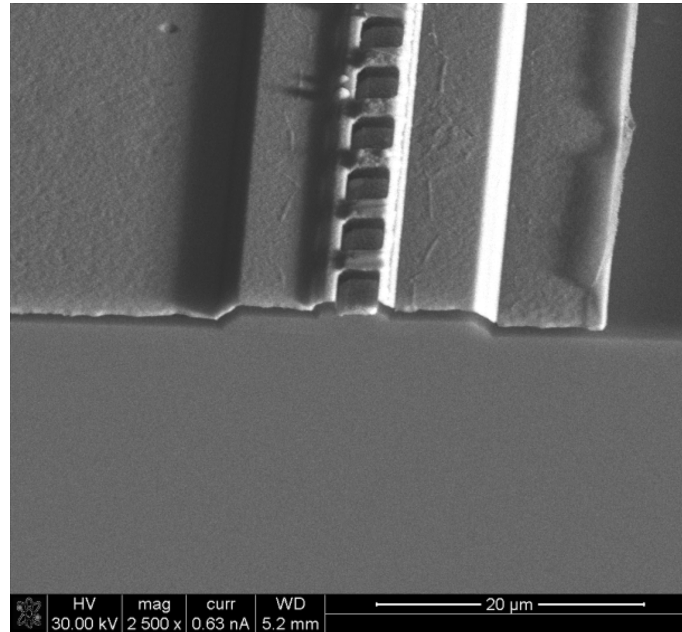

(a)

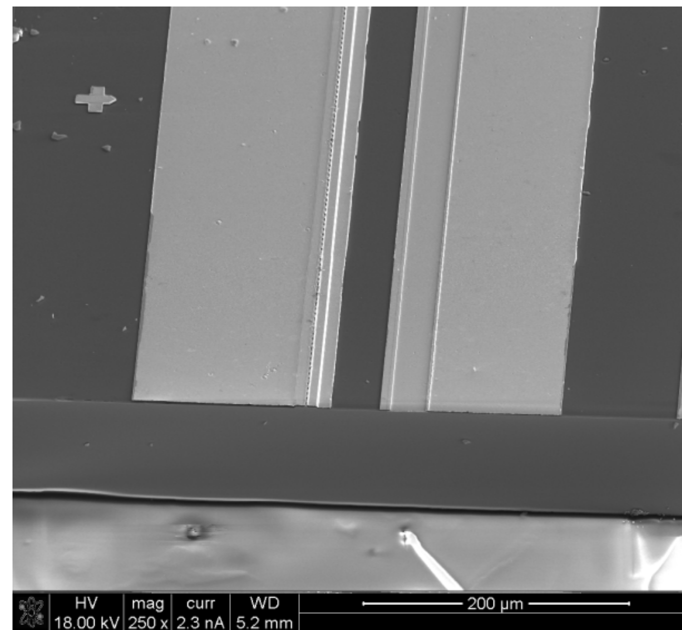

(b)

Fig. 3.7 Scanning electron microscopy images of (a) the ridge-waveguide laser facet and (b) overview of the fabricated device.

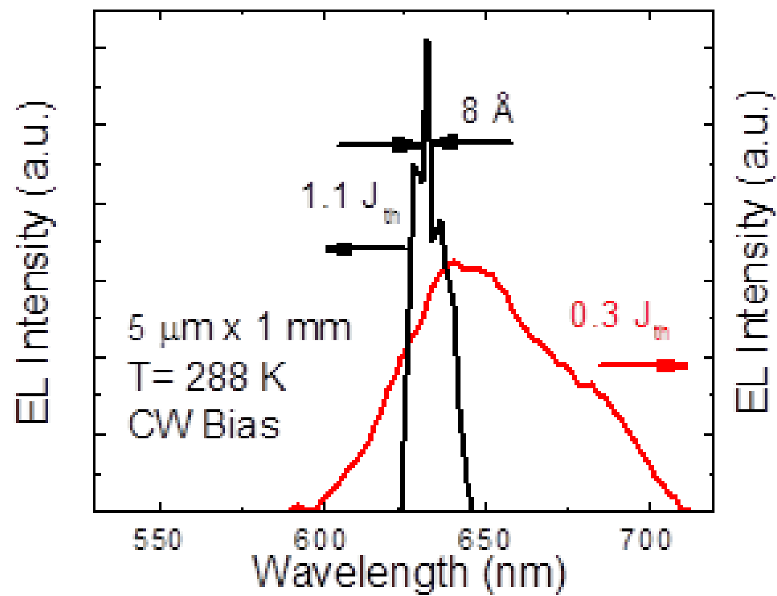

Fig. 3.8 Electroluminescence spectrum below threshold and at 1.1 times threshold.

3.4 DC Laser Characterization

Ridge waveguide, edge-emitting lasers of various cavity lengths were fabricated using standard photolithography, dry etching and metallization techniques. The typical ridge width is 5 µm and the cavity length varied from 0.6 to 1.6 mm. Broad area (10-50 µm devices) were also fabricated, but their results were generally worse than the smaller 5 µm devices and are not discussed here. This is likely due to the relatively large defect densities in the starting substrates (~10^6 cm^{-2}) which leads to increased non-radiative recombination in these devices. The ridge was etched down to the cladding/waveguide heterointerface to maximize the optical confinement while minimizing scattering losses associated with modal interaction with the sidewall. The end mirrors were formed by cleaving the device along the m-plane and subsequently coating the facets with e-beam evaporated dielectric DBRs (TiO_2/SiO_2) to enhance the reflectivities to ~0.73 and ~0.95.

The thicknesses are designed by transfer matrix method, described in Appendix D. The reflectivities are calibrated by measuring the reflectance of the stack on a silicon wafer.

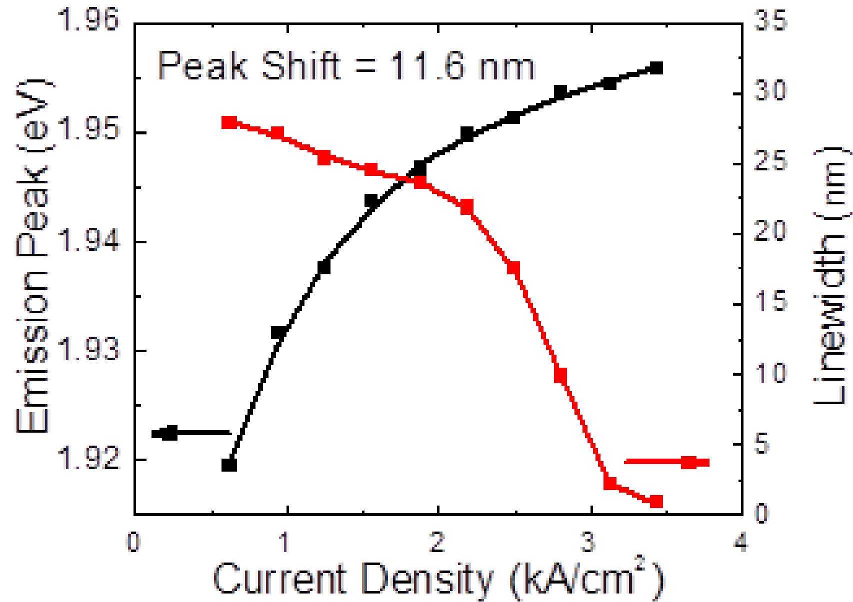

Fig. 3.9 Variation of the peak emission energy and dominant peak linewidth with injection.

Measurements were made on the lasers under continuous wave (CW) bias. Detailed schematics of the measurement setups for this chapter are shown in Appendix C. The measurements were performed at room temperature with adequate heat sinking to minimize heating effects in the devices. However, it should be noted that due to the relatively high series resistance in these lasers (30 Ω), the active device temperature may be substantially higher (>100ºC) [88]. The electroluminescence spectra of a laser below (0.3 J_{th}) and above (1.3 J_{th}) threshold are shown in Fig. 3.8. The lasing peak exhibits a blue shift of 11.6 nm due to the QCSE in the dots. This small shift is indicative of a small polarization field as the shift is significantly smaller than those reported for shorter

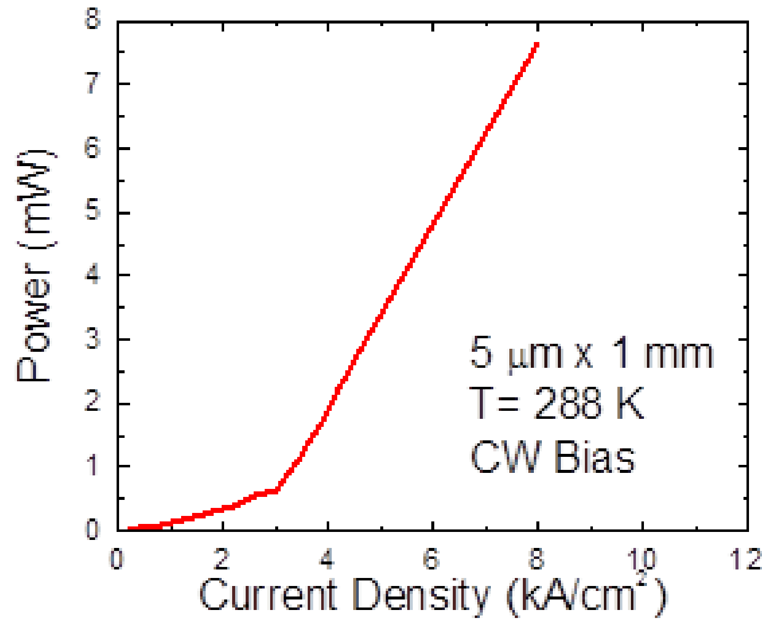

Fig. 3.10 Typical light-current characteristics from the low-reflectivity facet of the laser.

wavelength (blue and green) quantum well lasers grown on c-plane GaN substrates [13, 89]. The only other factor that may result in a blueshift is a decrease in temperature which is not the case here. The measured variation of the shift of emission peak with injection current density is plotted in Fig. 3.9. Also plotted in Fig. 3.9 is the variation of emission linewidth with injection current. A narrow linewidth of 8 Å is measured for the dominant longitudinal mode in the lasing spectrum, as indicated in Fig. 3.8. The variation of output power (from the low reflectivity facet) with injection current density is plotted in Fig. 3.10, from which a threshold current density of 2.5 kA/cm^2 is derived. The relatively large light output (0.5 mW) below the laser threshold is indicative of a relatively small spontaneous emission coupling coefficient, β. Further optimization of the laser heterostructure, by using an all InAlN cladding is described in chapter 4 & 5 and is used to increase the modal confinement and β. The polarization of the light output was

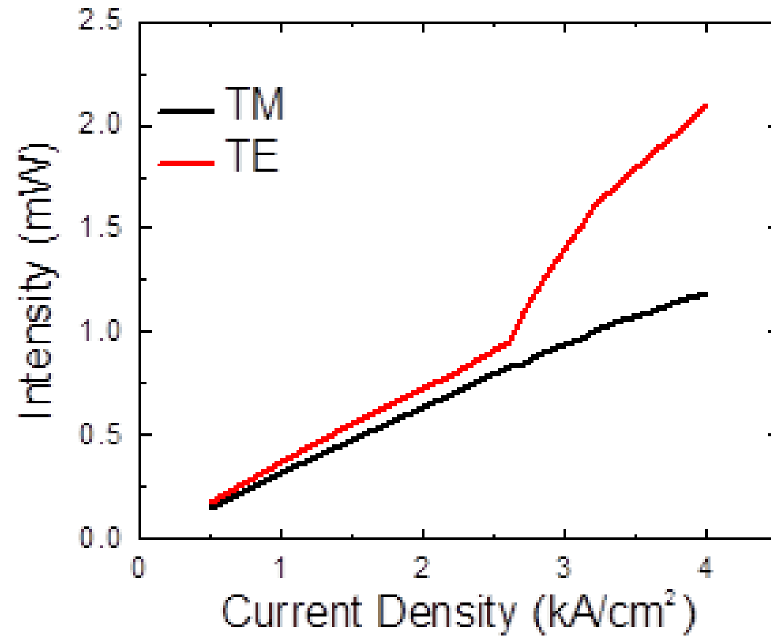

Fig. 3.11 Output polarization of the laser showing a TE threshold at 2.5 kA/cm^2.

measured as a function of the injection current density and the results are shown in Fig. 3.11. While the TM-polarized light output remains low throughout the injection range, the TE-polarized component increases significantly with a threshold at 2.5 kA/cm^2. This is because the TE mode has better confinement and a higher gain than the TM mode [90]. It should be noted that even beyond the TE threshold the TM output intensity does not saturate, which suggests that the Fermi levels do not clamp above threshold. This is likely due to the nearly degenerate valence band energy levels and band mixing effects.

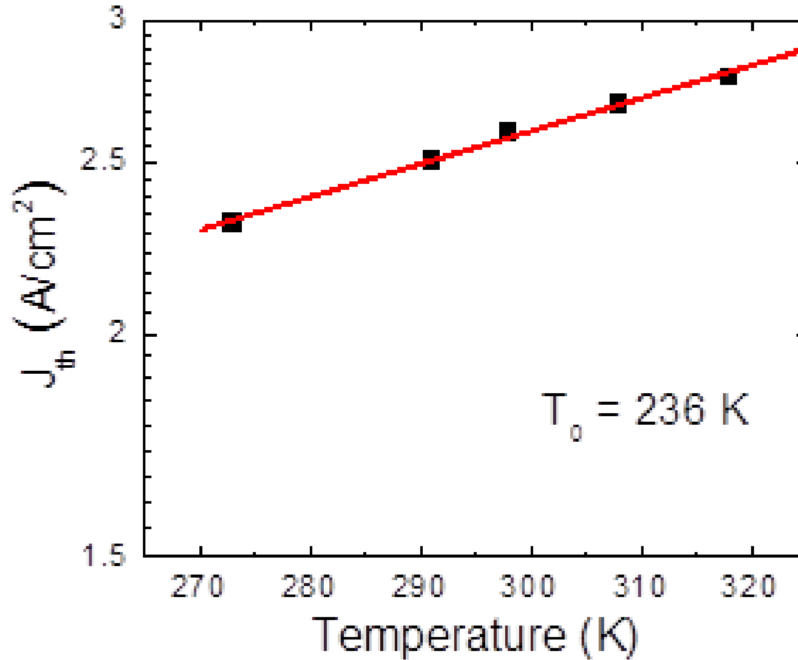

Fig. 3.12 Variation of threshold current density with temperature.

3.5 Temperature Dependent Laser Characteristics

An important aspect of laser performance is the temperature dependence of the threshold current, expressed by

$$J_{th}(T) = J_{th}(0)\exp\left(\frac{T}{T_0}\right) \tag{3.1}$$

where T_0 (K) is defined as the characteristic temperature. The output light-current characteristics, similar to that shown in Fig. 3.10, was measured at different temperatures in the range of 270-320 K. The variation of J_{th} with T is plotted in Fig. 3.12, from which a value of T_0 = 236 K is derived. This is a large value, as expected from a laser made with wide bandgap semiconductors. More importantly, this value of T_0 is larger than any previous values reported for red-emitting InGaP/InGaAlP double heterostructure and

MQW lasers [16-17]. The increase in threshold current with temperature can be accounted for by considering the increasing spread of electrons and holes in the respective bands and carrier leakage from the active region. In small bandgap semiconductor lasers Auger recombination plays a major role in increasing the temperature dependence and the value of T_0 is reduced to 40-60K. In the InGaN/GaN QD lasers carrier leakage is minimized by the quasi-3D confinement and confinement of carriers in the deep potential wells of the $In_{0.4}Ga_{0.6}N$/GaN dots (ΔE_c, ΔE_v ~ 870, 580 meV) [91]. However, the multiplicity of hole states [92] will lead to occupation of higher energy states as the temperature is increased and hole leakage from these states can take place.

3.6 Gain and Differential Gain Measurement

The threshold current of a semiconductor laser and the dynamic characteristics including the small-signal modulation bandwidth, chirp and linewidth enhancement factor are ultimately determined by the gain in the active region. The gain of the $In_{0.4}Ga_{0.6}N$ QD lasing medium near threshold was measured by the Hakki-Paoli technique [93] using the formula:

$$\Gamma g_i = \frac{1}{L}\ln\left(\frac{r_i^{1/2}+1}{r_i^{1/2}-1}\right) + \frac{1}{L}\ln(R) \qquad (3.2).$$

Here Γ is the optical confinement factor, L is the cavity length, R is the facet reflectivity, and

$$r_i = \frac{I_p + I_{p+1}}{2I_v} \qquad (3.3)$$

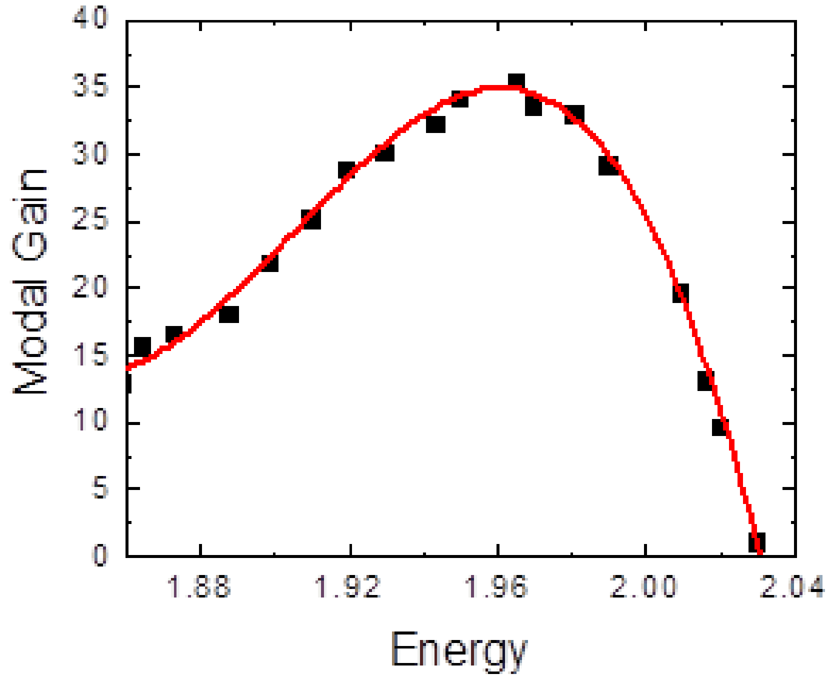

Fig. 3.13 Gain spectrum of the red-emitting quantum dots measured using the Hakki-Paoli technique.

where I_p and I_{p+1} are adjacent peak intensities in the electroluminescence spectrum separated by the valley intensity, I_v. The emission spectra for increasing injection are recorded (with a spectral resolution of 0.03 nm), till threshold is reached, when the spectra is characterized by a succession of peaks and valleys. The spectral gain is derived by analyzing these data. The net modal gain Γg is plotted as a function of photon energy in Fig. 3.13. The peak net modal gain at threshold is 35 cm^{-1}, which compares well with calculated modal gains for green (λ = 524 nm) InGaN/GaN QD lasers [20]. The peak modal gain is also comparable to those reported for InGaAs/GaAs and other quantum confined heterostructure lasers.

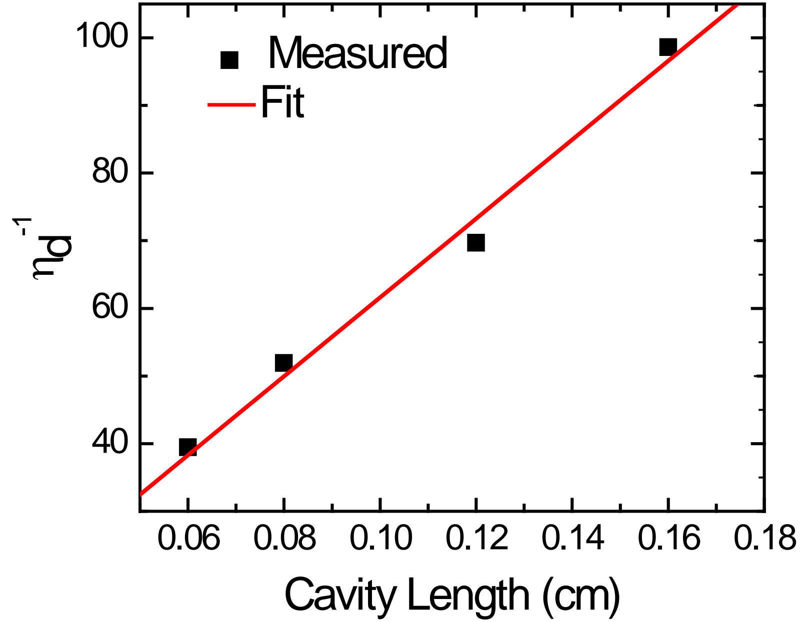

Fig. 3.14 Variation of the differential quantum efficiency with laser cavity length.

Light-current measurements have been made on lasers of varying cavity lengths and the differential quantum efficiency η_d and J_{th} were recorded for each length. Figure 3.14 shows the variation of η_d^{-1} with cavity length. From this data, a value of $\eta_i = 0.30$ is derived using the relation:

$$\frac{1}{\eta_d} = \alpha_i L \ \ln\frac{1}{\sqrt{R_1 R_2}} + \frac{1}{\eta_i} \tag{3.4}$$

where η_d is the differential efficiency of the laser, R_1 and R_2 are the mirror reflectivities, L is cavity length, and α_i is the cavity loss. The cavity loss is determined to be 25 cm^{-1} in these heterostructures. Further optimization, by using an all InAlN cladding, results in reduced cavity loss, higher spontaneous emission coupling into the laser mode, reduced threshold current density, and higher output powers and is discussed in chapter 4 & 5. Measured values of J_{th} are plotted against inverse cavity length in Fig. 3.15. The

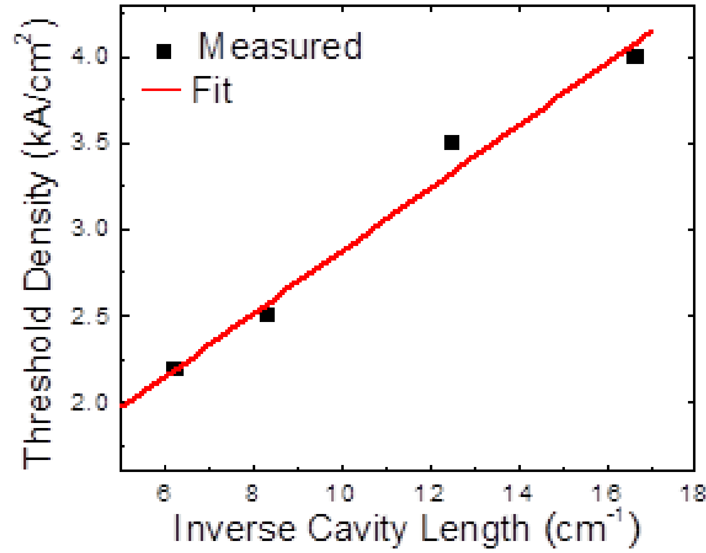

Fig. 3.15 Variation of the threshold current density with inverse cavity length.

differential gain dg/dn is calculated by analyzing this data with the relation the relation [97]:

$$J_{th} = J_{th}^{0} + \frac{qd}{\Gamma \eta_i \tau_r \frac{dg}{dn}}\left[\alpha_i + \frac{1}{2L} ln\left(\frac{1}{R_1 R_2}\right)\right] \quad (3.5)$$

where d is the active region thickness calculated as the number of dot layers times the effective dot height (3.55 nm), Γ is the product of the optical confinement factor simulated by the transfer matrix method (0.07) and the fill factor (0.35), τ_r is the measured radiative lifetime (2.2 ns), and R_1 and R_2 are 0.73 and 0.95, respectively; the transparency current density J_{th}^0 and dg/dn are fitting parameters for this function. A value of differential gain dg/dn = 3.8 x 10^{-17} cm^2 is derived along with a value of J_{th}^0 = 850 A/cm^2.

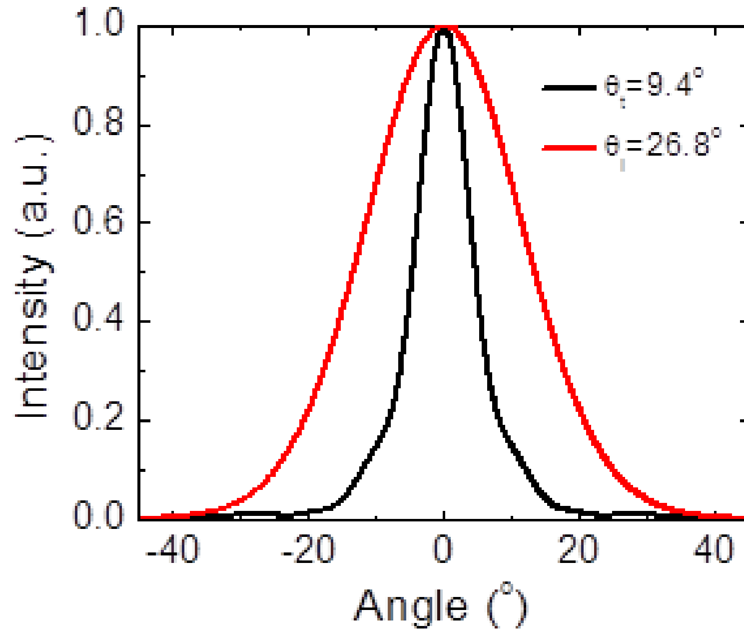

Fig. 3.16 Far field mode profile measured from the low reflectivity laser facet.

3.7 Far Field Imaging of the Laser Output

Finally, the output of the lasers was characterized by far field imaging. The far field pattern of the output from one of the facets (R=0.73) of a device with a 4 μm ridge device is shown in Fig. 3.16 along the growth (transverse) and lateral directions. The pattern is characterized by a divergence angle of 26.8° in the transverse direction and 9.4° in the lateral direction, yielding an aspect ratio of 2.85. A narrower ridge may be used to reduce the astigmatism of the laser output. However, this would result in higher scattering loss and devices with smaller ridges being more difficult to fabricate.

3.8 Summary

Red-emitting lasers using the III-nitride material system are important devices with the potential for the creation of monolithic white light sources and solid state displays. While blue- and green-emitting InGaN/GaN quantum well and quantum dot lasers have

previously been demonstrated, red-emitting nitride lasers had remained elusive. The first red-emitting InGaN/GaN quantum dot lasers are demonstrated. Due to the reduced polarization field present in the quantum dots, efficient recombination at 630 nm can be demonstrated with an efficiency of >30%. The lasers uniquely incorporate $In_{0.18}Al_{0.82}N$ cladding in order to improve the optical confinement at these long emission wavelengths. Detailed steady state characterization of the lasers has been presented including light-current characterization, showing a threshold at 2.5 kA/cm^2. The lasers have been measured at varying temperatures, from which a characteristics temperature of 236 K is derived. These characteristics are much better than those reported in red-emitting InGaAlP based laser diodes. The gain and differential gain have been measured and reported using Hakki-Paoli measurements and length dependent L-I characterization, respectively. These characteristics are very promising for high efficiency white light sources and projectors where high temperature stability is a requirement.

Chapter IV

Optimization of the InGaN/GaN Quantum Dot Laser Heterostructure

4.1 Introduction

The prior chapters in this work have discussed the need for long wavelength III-nitride lasers (chapter 1), the growth of red-emitting self-assembled InGaN/GaN quantum dots (chapter 2), and the characterization of lasers incorporating such quantum dots (chapter 3). In the growth and fabrication of these devices, it is important to keep in mind the requirements for real world applications including white light sources (solid state lighting), displays and projectors (including heads-up displays in automobiles), and plastic fiber communication, amongst others [1-2, 98-100]. For these applications, it is desirable to use lasers with low threshold current density, high output power, high differential gain, and high efficiency. For plastic fiber communications, it may additionally be desirable to directly modulate the semiconductor lasers, which would also require large small-signal modulation bandwidth. While the red lasers presented in chapter 3 are characterized by small threshold current density (J_{th}~2.5 kA/cm^2), the output power is relatively small (8 mW). Improving the output power will also increase the efficiency, making these quantum dot lasers more attractive for the applications discussed above. Reducing the cavity loss, by redesigning the laser waveguide, increasing the quantum dot efficiency, and reducing device self heating by improving the diode

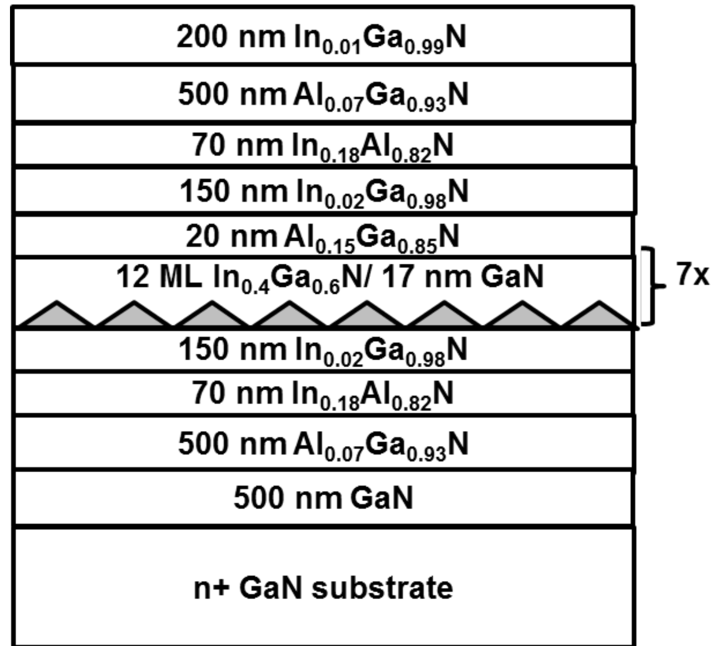

Fig. 4.1 Quantum dot laser heterostructure.

characteristics will help to reach these goals. The optimization of these parameters are discussed in this chapter and devices incorporating such optimizations are discussed in chapter 5.

4.2 Motivation for Optimizing InGaN/GaN Quantum Dots and Laser Heterostructure

The quantum dot laser heterostructure presented in chapter 3 was the first III-nitride laser grown at such long wavelengths (630 nm). While many of the performance characteristics of these lasers are compatible with real work applications (small threshold current density, high temperature stability, small polarization field in the dots), the maximum output power in these devices was still limited to around 8 mW. In many applications, including heads-up displays in automobiles [101-103], it would be desirable to increase the output power into 10s of mW or 100s of mW [104]. In this chapter, the

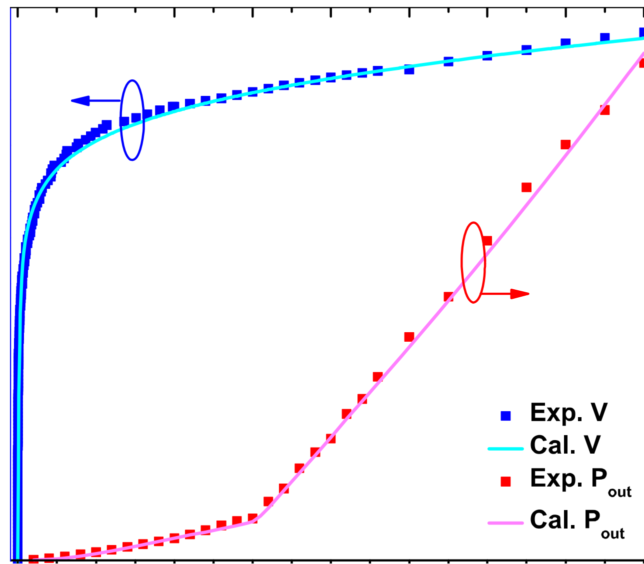

Fig. 4.2 Laser light-current-voltage characteristics.

optimization of the various layers in the laser heterosturcture (cladding, doping levels, quantum dot efficiency) are investigated. The laser diodes had relatively large series of ~30 Ω, compared with ~8-10 Ω in diodes grown on sapphire. Additionally, the presence of a partial AlGaN cladding still lead to a cavity loss of 25 cm^{-1}. The feasibility of replacing this will all $In_{0.18}Al_{0.82}N$ cladding is investigated. In particular, this large bandgap material (~4.5 eV) may have further reduced p-doping as compared with GaN (3.4 eV). Finally, further optimization of the quantum efficiency, η_i, is investigated to improve the level of spontaneous recombination and to reduce the threshold current density.

Due to the relatively large series resistance found in these diode (~40 Ω), device heating may be a series issue. While the substrate temperature is kept fixed by a

thermoelectric cooler, as detailed in Appendix C, the junction temperature may be significantly higher. To investigate this, the diode optical and electrical characteristics were performed by our collaborators, Prof. John Dallesasse's group at UIUC, using the laser heterostructure from chapter 3, shown in Fig. 4.1. Details on the growth of this device are listed in chapter 3. The L-I-V characteristics are given in Fig. 4.2 (dotted points). Above threshold, the laser dissipates as much as 6 W of heat, given the relatively small wall plug efficiency of this device (~0.2%). The solid lines are calculated, discussed in more detail in [88]. With a thermal impedance of 43ºC/W [88, 105-106], the laser reaches a junction temperature of ~120ºC at threshold under continuous wave biasing at an ambient temperature of 20ºC. The relatively large temperature stability (T_0>200 K), discussed in chapter 3 despite this large junction heating is likely due to the large band offsets in these long wavelength devices (ΔE_c ~ 1 eV). To further confirm the device heating, the modal gain, shown in Fig. 4.3, is calculated at 120ºC and compared with the measured modal gain from chapter 3. A good agreement with the measured data (points) and the calculated modal gain (red line) at 120ºC agrees with the device heating in the L-I-V. The slight mismatch at smaller energies is likely due to the distribution of multiple dot sizes amongst the first two layers, as discussed in chapter 2.

In summary, the relatively large threshold current densities necessary to operate the laser (J_{th}~2.5 kA/cm^2) are due to relatively low internal quantum efficiency (36%), high series resistance (30 Ω), and large cavity loss (25 cm^{-1}). Optimization of the quantum efficiency, p-doping, and laser waveguide will allow for lasers with reduced threshold current densities, higher output powers, and higher efficiency. Optimization of these parameters are discussed in chapter 4.

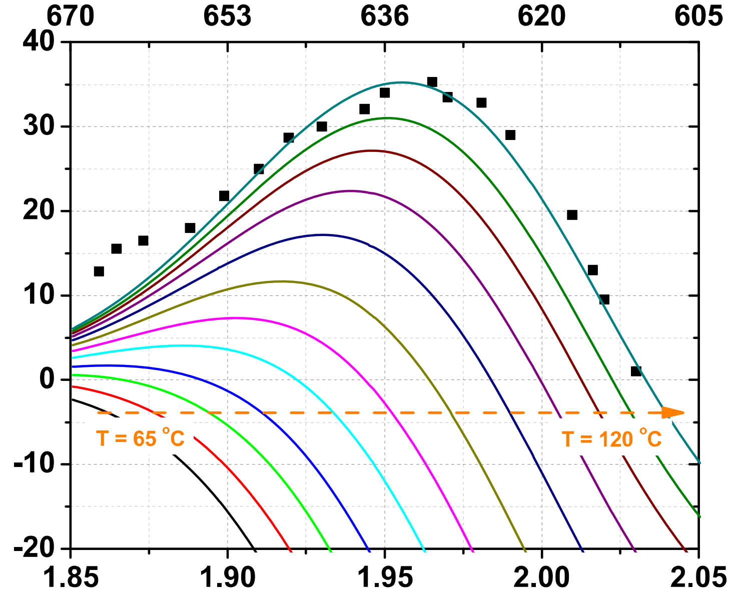

Fig. 4.3 Measured modal gain (points) and calculated modal gain (solid curves) for varying injections.

4.3 Optimization of p-doping with Metal Modulated Epitaxy

The large bandgap present in the III-nitrides has led to several challenges in the growth of electrically injected heterostructures. The most well known of these challenges is likely large activation energy of the acceptor levels in the material. Treating the acceptor (Mg being the most common in GaN) under the Bohr model [107], it is possible to estimate the acceptor energy, E_a:

$$E_a = E_v + \frac{e^4 m_h^*}{2(4\pi\epsilon)^2\hbar^2} \tag{4.1}$$

where E_v is the valence band edge, e is the charge on an electron, m_h^* is the hole mass, ϵ is the permittivity of the material, and $\hbar$ is the reduced Planck's constant. Upon substitution of the appropriate constants, this can be rewritten as:

$$E_a = E_v + 13.6\frac{m_{h,r}}{\epsilon_r^2} \tag{4.2}$$

where $m_{h,r}$ is the relative hole mass (m_h^*/m_0), and ϵ_r is the relative permittivity. With the relatively large hole mass in GaN (m_{hh}~1.2 m_0) and for a dielectric constant of 9.7 [ ], an activation energy of ~175 meV above the valence band edge is expected in this material. Reported activation energies of hole in GaN:Mg are indeed close to this value [109-111]. The number of thermally activated holes at room temperature (k_BT~24.8 meV), given by:

$$p\sim \exp\left(-\frac{E_a-E_v}{k_BT}\right) \tag{4.3}$$

will only be around 1%. For a hole concentration of 10^{17} cm^{-3} this requires a doping concentration of 10^{19} cm^{-3} of electrically active (substitutional) magnesium atoms in the GaN crystal. This problem is further exacerbated by the relatively large background n-type doping concentration of 10^{17} cm^{-3}, caused by nitrogen vacancies [112-115].

	STANDARD GROWTH	MME
T_{sub}	p-GaN: 675℃	p-GaN: 600℃
N2 plasma	GaN: 0.66 sccm / 300W	GaN: 0.66 sccm / 300W
Ga Flux	Ga: 2 x 10^{-7} Torr	Ga: 3.5 x 10^{-7} Torr
Growth Rate	GaN: 220 nm/hr Ga, N & Mg shutter open continuously	GaN: 200 nm/hr (shutters open) N shutter open continuously Ga & Mg: 5s open/10s closed

Table 4.1 Growth conditions for standard p-doped GaN and recipe for metal modulated epitaxy p-doped GaN.

The injection of holes into the active region requires high quality, highly doped cladding and contact layers. While standard growth techniques have resulted in doping p~1x10^{18} cm^{-3} in GaN, a high level of Mg (10^{20} cm^{-3}) is required to achieve this value and intrinsic n-doping from nitrogen vacancies must also be overcome both of which degrade material quality and efficient injection of holes. An alternative is to use metal modulated epitaxy (MME), where the metal shutters are open and closed periodically during the growth (typical conditions being ~5 seconds open / 10 seconds closed) [31]. While the precise mechanism for the increased efficiency of hole doping is not known, it may be due to the additional time given to the Mg atoms on the surface to diffuse and to fill in vacancies. We have studied the characteristics of GaN p-i-n diodes grown using our standard growth techniques and using MME, with the growth conditions described` in Table 4.1. In addition to the interruption of the growth, the substrate temperature is

20 nm p+GaN
100 nm p-GaN
20 nm GaN
300 nm n-GaN
n+ GaN on Sapphire

Fig. 4.4 Heterostructure used for testing diode characteristics of the p-GaN layers grown under various conditions.

lowered and higher gallium flux (1.75x) is used. The diode heterostructure is shown in Fig. 4.4. The diodes are identical except for the different conditions used for growing the p-GaN. The diodes are fabricated in a similar procedure to that described in Appendix B. Step 7 (deposition of the p-contact) is carried out first, but the thickness of the p-contact is reduced to 5nm/5nm Ni/Au so the contact will be optically transparent. Step 3 (etching to the n-GaN) and step 4 (deposition of the n-contact) are carried out in an identical manner as described in Appendix B. The size of the devices is 280 μm x 280 μm. The electrical characteristics of the two diodes are shown in Figs. 4.5 (a) and (b), respectively. As can be seen, the MME diode has a substantially shaper turn-on at 3 V, with reduced series resistance (6 Ω vs 9 Ω).

To further study the material properties of the standard and MME p-GaN layers by themselves, layers were grown on sapphire substrates with an AlN buffer layer, as shown schematically in Fig. 4.6. Ohmic Hall [116] and transmission line measurement (TLM) [117] contacts were places on the samples which were used to characterize the

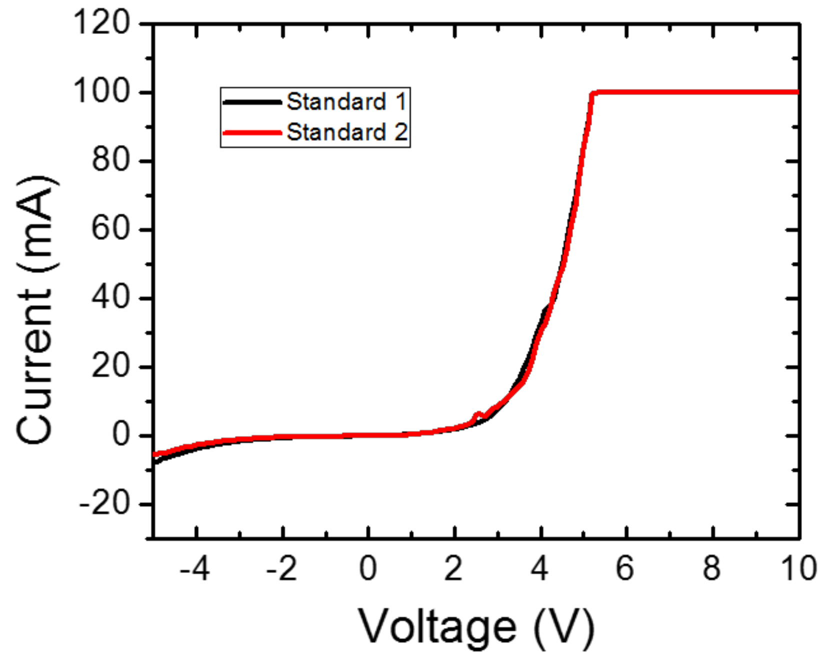

(a)

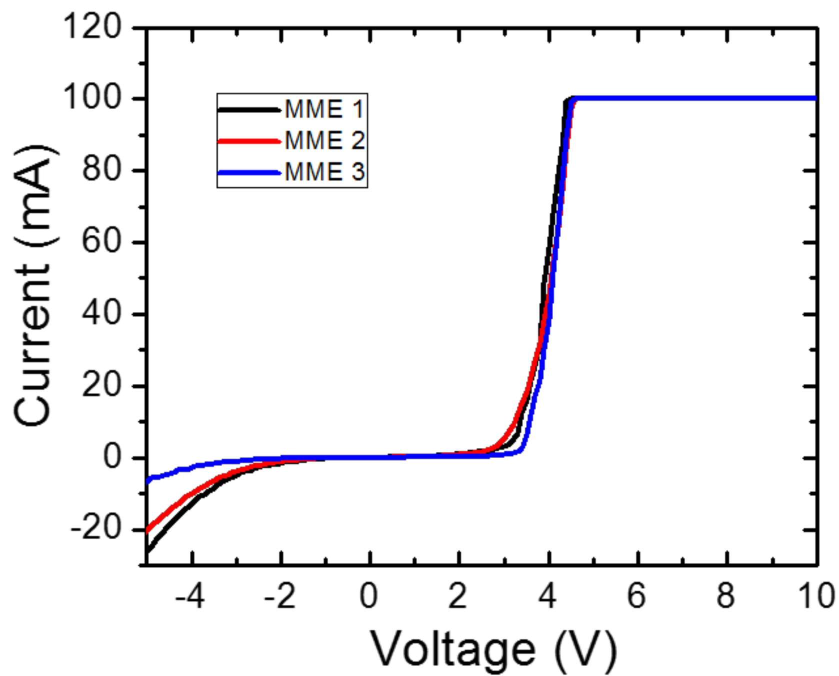

(b)

Fig. 4.5 Diode I-V characteristics for devices grown with standard p-GaN and MME p-GaN, as described in Table 5.1. The multiple curves on each plot are from different devise on the same chip.

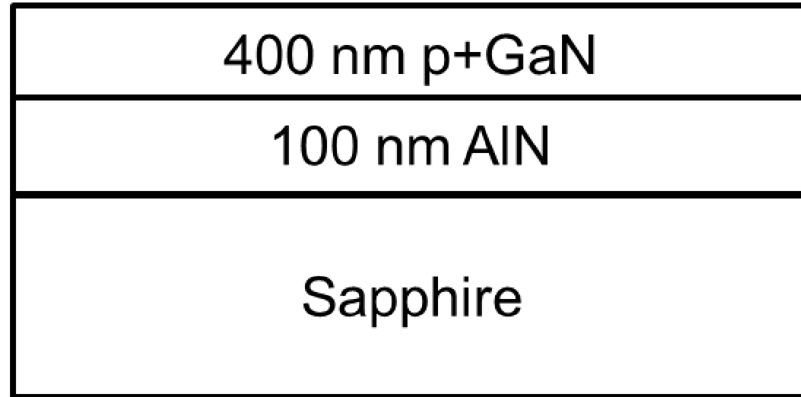

Fig. 4.6 Heterostructure used for measured of electrical characteristics of the p-dopde GaN layers.

Parameter	MME p-GaN	Standard p-GaN
Hole Concentration, p	3.5 x 10^{18} cm^{-3}	1.8 x 10^{18} cm^{-3}
Hole Mobility, μ_h	0.26 cm^2/Vs	0.30 cm^2/Vs
Resitivity	7.3 Ωcm	11.4 Ωcm

Table 4.2 Comparison of hole concentration, mobility and resistivity of p-doped GaN layers.

resistivity and contact resistance of the samples. The MME layers were characterized by a contact resistance which is nearly an order of magnitude smaller and a resistivity (and sheet resistance) of ~2/3. The p-doping in the MME sample was 3.5 x 10^{18} cm^{-3}, nearly twice that in the standard sample. The full characteristics of the Hall samples are shown in table 4.2.

To further study and optimize the p-doped GaN using MME, four additional samples were grown, as summarized in table 4.3. Standard refers to the standard p-doping

Diode	Description
Standard	Standard p-GaN
Ref MME	Reference MME
LT MME	T_{sub}[600°C]-10°C
Ga+ MME	Φ_{Ga}[3.5e-7 Torr]*1.05
Mg+ MME	Φ_{Mg}[1e-8 Torr]*1.1
In MME	Φ_{in}(2.2e-8Torr)

Table 4.3 Growth conditions of the MME p-GaN for testing the diode characteristics. The description column lists the changes in each device from table 4.1.

recipe described above, and the reference MME sample refers to the growth conditions in table 4.1. The other test heterostructues were identical with one change during each growth. LT (low temperature) MME had the substrate temperature reduced from 600°C to 590°C to increase the Mg sticking coefficient. Ga+ MME had the gallium flux during the growth increased by 5% to reduce nitrogen vacancies. Mg+ MME had the magnesium flux increased by 10% to increase the Mg concentration in the crystal. In MME was identical to the reference MME sample, but an additional flux of 2.2×10^{-8} Torr indium was added to act as a surfactant and reduce the band gap slightly (increasing the thermally activated hole concentration). Each MME layer was grown on 20 nm i-GaN/300 nm n+GaN to test the diode characteristics, shown schematically in Fig. 4.4. The current-voltage (I-V) characteristics of the best diode on each sample are shown in Fig. 4.7. Table 4.4 shows a summary of the diode characteristics from the devices listed in table 4.3. As can be seen, the diode grown at a slightly lower temperature (590°C) had

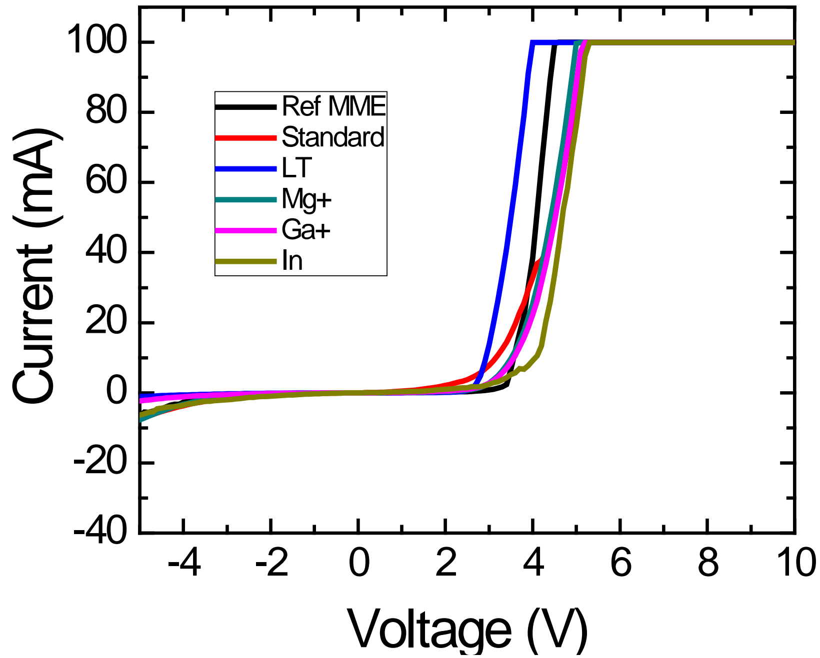

Fig. 4.7 Current-Voltage characteristics of the best device on each sample from the diodes with varying p-GaN growth conditions, described in tables 4.1 and 4.3.

Diode	Turn-On	Series Resistance	Reverse Leakage (at -5V)
Standard	3.5 V	10 Ω	7.6 mA
Ref MME	3.3 V	6 Ω	6.6 mA
LT MME	2.7 V	7 Ω	1.0 mA
Ga+ MME	3.25 V	9 Ω	2.3 mA
Mg+ MME	3.25 V	8 Ω	7.7 mA
In MME	3.25 V	8 Ω	6.4 mA

Table 4.4 Electrical characteristics from the diodes described in table 4.3.

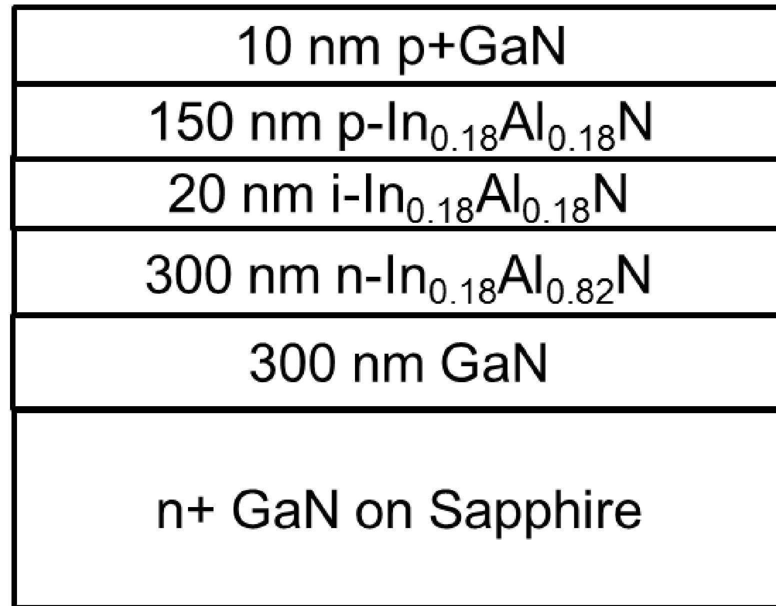

Fig. 4.8 InAlN diode heterostructure. The thin p+GaN on top is to reduce the contact resistance.

the best I-V characteristics in terms of leakage and turn-on, and comparable series resistance with the reference sample. It should be noted that further lowering the temperature was also investigated but resulted in degraded diode characteristics. Finally, the optimized MME p-GaN was grown on AlN/Sapphire substrates and Hall measurements were performed from which a hole concentration of 3.6 x 10^{19} cm^{-3} was obtained, more than one order of magnitude higher than the reference MME and standard p-GaN samples.

4.4 Laser Heterostructure with all InAlN Cladding

By optimizing the laser cladding and waveguide layers, we can improve the optical confinement factor and reduce the losses associated with substrate leakage and free carrier absorption in the doped cladding. While typical GaN-based lasers incorporate

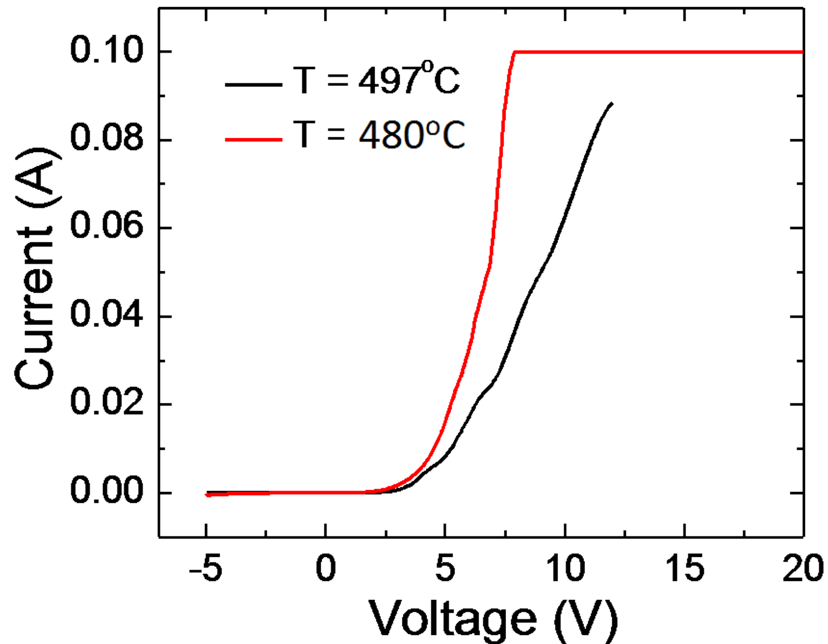

Fig. 4.9 Diode I-V characteristics with the $In_{0.18}Al_{0.82}N$ grown at 497°C, and 480°C.

$Al_xGa_{1-x}N$ layers [4-13, 19, 20] for the laser cladding, such layers are of limited use at longer wavelengths where the refractive index difference between the cladding and waveguide becomes reduced, as discussed in chapter 3. Additionally, due to the tensile strain present in these layers, the thickness of these layers is limited, further increasing substrate leakage. Alternatively, $In_{0.18}Al_{0.82}N$ layers can be grown which has much lower refractive index than what can be achieved with $Al_{x\sim0.07}Ga_{\sim0.93}N$ layers. However, due to the large effective hole masses in this material, p-doping of this material may pose a challenge. The lasers described in chapter 3, while incorporating a mixed AlGaN/InAlN cladding, may improved if an all InAlN cladding could be used. However, due to the large bandgap, whether this will increase the series resistance need to be investigated.

To determine the electrical characteristics of the $In_{0.18}Al_{0.82}N$ layers, p-i-n diodes were grown with the structure shown in Fig. 4.8. To optimize the electrical characteristics of the material, diodes were grown under varying conditions including substrate temperature. The electrical characteristics of two diodes, grown at 480°C and 497°C are shown in Fig. 4.9. The lower temperature growth results in a substantially reduced series resistance (10 Ω vs 25 Ω). It should be noted that the indium flux had to be lowered from $2.5x10^{-8}$ Torr to $2x10^{-8}$ Torr to compensate for the reduced substrate temperature and increased indium sticking coefficient compared with the samples described in table 3.1 when the substrate temperature was lowered to 480°C. XRD was used to confirm the composition was lattice matched to GaN with x=0.18 in both didoes. The reduction in the series resistance is likely due to increased magnesium incorporation at this temperature. This value is comparable to that in GaN p-i-n diodes grown and described in section 4.4, making these layers suitable for incorporation into the laser heterostructure. Secondary ion mass spectroscopy was used to measure the Mg concentration of $8x10^{20}$ cm^{-3} allowing for the very high hole concentration at room temperature.

The low series resistance of the $In_{0.18}Al_{082}N$ diodes will allow for replacement of the $Al_xGa_{1-x}N$ cladding with $In_{0.18}Al_{0.82}N$, including on the p-side. In addition to the improved modal confinement and expected reduction in cavity loss, removing the AlGaN will provide one additional benefit to the laser growth. The p-$In_{0.18}Al_{0.82}N$, with its relatively low growth temperature (480°C) will allow the quantum dots be growth with minimal high temperature annealing (~750°C) during the growth of the (Al)GaN. This allows for minimized outdiffusion of indium during these layers and will preserve the dot properties, optimized without the growth of the top half of the laser.

4.5 Optimization of Red-Emitting InGaN/GaN Quantum Dots

4.5.1 Optimization of InGaN Thickness for Each Dot Layer

Room temperature photoluminescence (PL) intensity from the heterostruture (shown in Fig. 4.10) from seven layers of $In_{0.4}Ga_{0.6}N$/GaN self assembled quantum dots will be strongly dependent on the number of InGaN MLs used to form quantum dots. Three QD samples were grown with ~6, 8 and 10 MLs of InGaN grown to form a self-assembled InGaN QD layer. Seven such layers of InGaN/GaN QDs were grown and characterized to see the effects of InGaN ML on structural and optical properties of the QDs. The highest PL intensity (and efficiency) is obtained from the QD sample with 8 MLs of grown InGaN as seen in Fig. 4.11 (a). A 1x1 μm^2 AFM scan of topmost eighth layer of uncapped InGaN QDs show that the QDs have a base diameter of ~42 nm and height of ~3 nm, with a typical dot density of ~7 x 10^{10} cm^{-2}, as shown in Fig. 4.11 (b). For QDs grown with 12 MLs of InGaN, the PL intensity from the same number of dot layers (seven) was found to be lower. This is possibly due to a larger dot size resulting from increased growth time. A larger size quantum dot will result in reduced e-h wavefunction overlap which is confirmed by longer radiative carrier lifetimes measured on these samples (Fig. 4.11 (c)). Growth of QDs with only 6 MLs of InGaN results in the formation of incomplete QDs with reduced size (height ~2.5 nm, base ~ 34 nm) and low aspect ratio resulting in lower PL intensities due to electron wavefunctions extending into barrier regions [118]. An optimum number of MLs is required to obtain QDs with highest

intensities. For red emission, ~8 MLs of $In_{0.4}Ga_{0.6}N$ are optimum to obtain QDs having strong intensities and efficiencies.

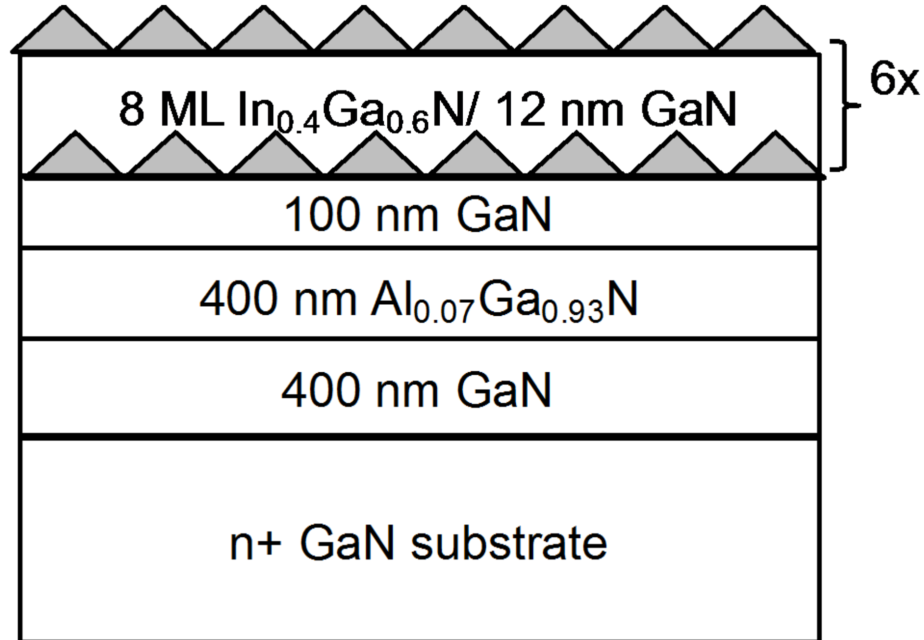

Fig. 4.10 Quantum dot heterostructure used for optimizing the quantum dot efficiency. The InGaN thickness, GaN barrier thickness, and nitrogen interruption time were optimized.

4.5.2 Optimization of N_2 Growth Interruption Time During Each Dot Layer

After the growth of 8 MLs of the InGaN layer on GaN at 540°C to form the QDs, growth was interrupted and the QD layer was annealed in-situ under the presence of nitrogen flux for various times before the growth of GaN barrier. Fig. 4.12 shows the variation of PL intensities and shifts in peak energies for 2, 5 and 10 second interruption times. For an increase in the interruption time from 2 to 10s, an increase in the dot size was observed, likely due to enhanced adatom mobility on the surface due to the presence of nitrogen. This likely leads to reduced e/h overlap and reduced efficiencies.

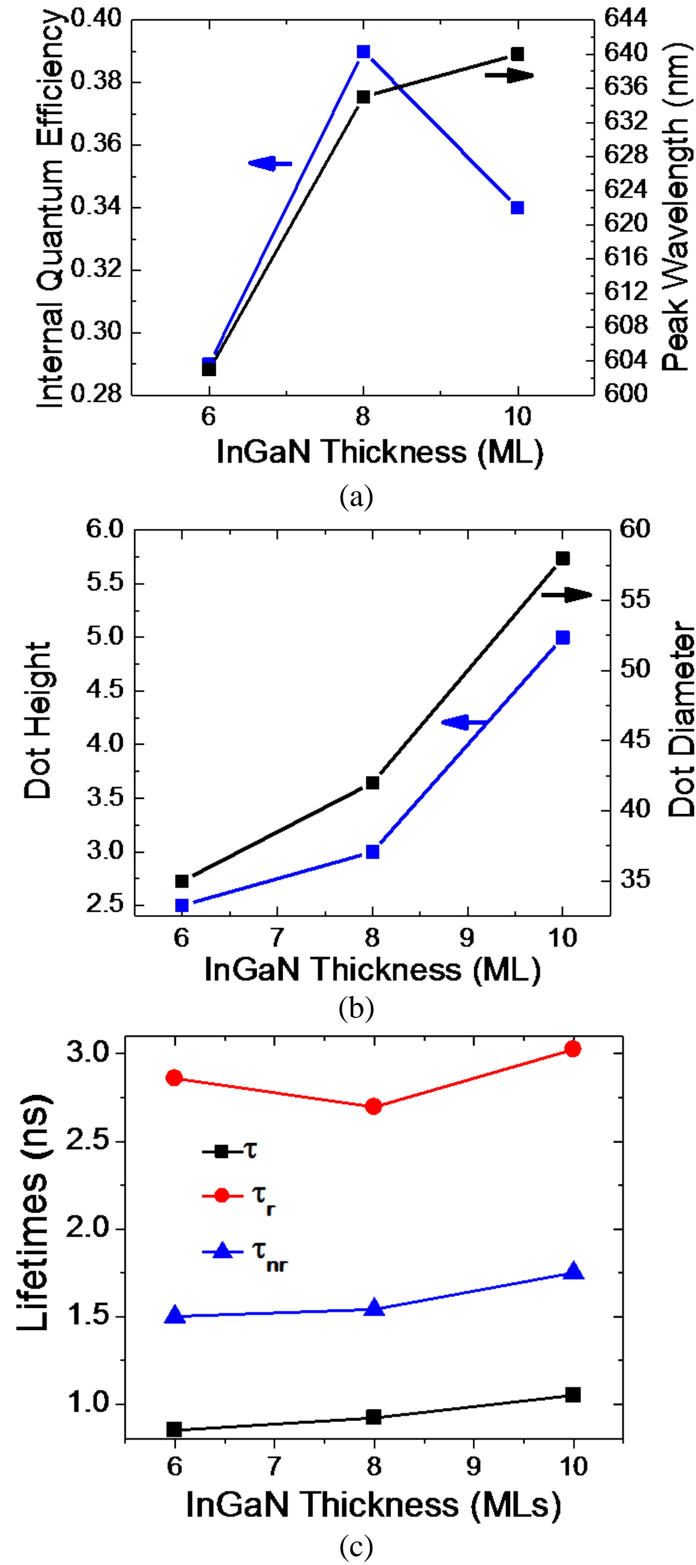

Fig. 4.11 Variation of (a) optical properties, (b) structural properties, and (c) carrier lifetimes with change in deposited InGaN thickness.

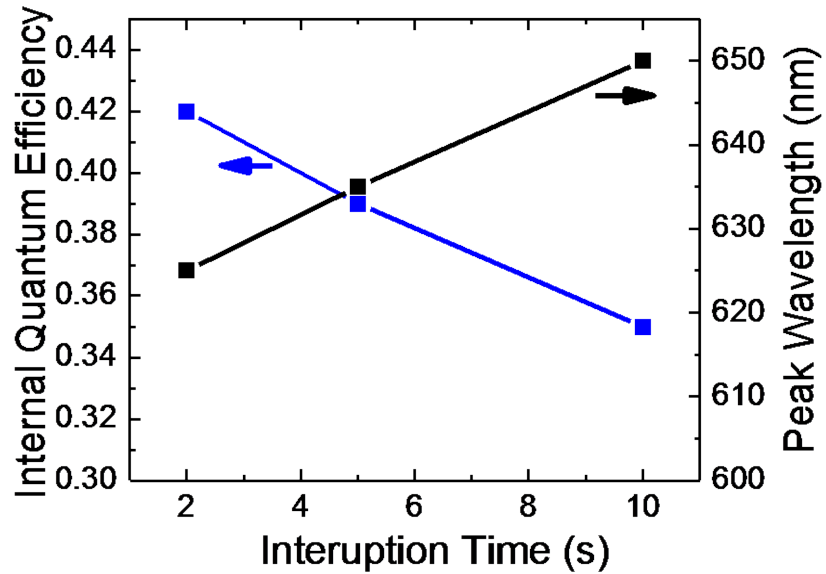

(a)

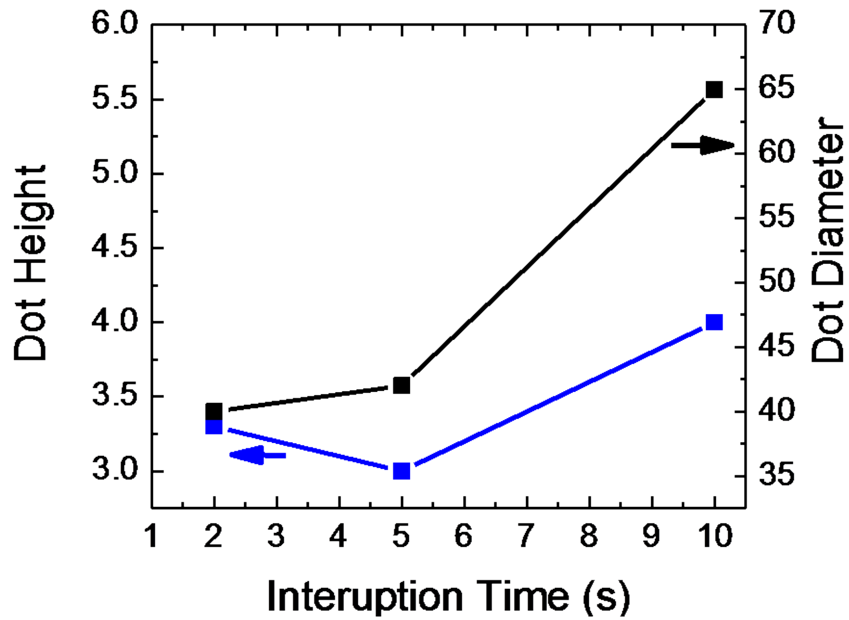

(b)

Fig. 4.12 Variation of (a) optical properties, (b) structural properties, and (c) carrier lifetimes with change ininteruption time.

The enhanced PL intensity at low interruption times and reduced radiative carrier lifetimes is found in well-formed high density QDs. A further reduction in interruption time (t = 0 s) showed a further reduction in average dot size, likely due to the formation of incomplete dots and led to reduced efficiencies. Additionally, larger annealing times

possibly result in coalescence of smaller dots to form bigger islands due to Ostwald ripening [119]. This explains both the lowering of the PL intensity and an observed increase in carrier lifetimes. An optimum interruption time after QD layer growth enhances the optical properties of the QD layers significantly. A continual red-shift in peak PL emission from QD samples is observed with increasing annealing times. This follows from the increasing dot size which causes comparatively larger piezoelectric polarization field in the dots resulting in red-shift in emission.

4.5.3 Optimization of GaN Barrier Layer Thickness

A sufficient GaN spacer layer thickness in between two layers of InGaN QDs is required to relax the tensile strain present in the spacer layer and promote growth of uniform uncoupled QDs. However, as discussed in chapter 2, this strain and the indium segregation from the previous layer is required to form high density QDs. If the barrier thickness is too low, the different QD layers may exhibit significantly different structural, and hence, optical properties. This would cause broadening of the PL spectrum and reduced efficiency. The growth conditions of the GaN barrier layers were calibrated at the optimized InGaN QD growth conditions, described in the previous sections. Quantum dot samples with 9, 12 and 15 nm of GaN barrier thicknesses were grown and characterized. PL intensities show an initial increase with increasing barrier thickness (Fig. 4.13(a)), followed by a decrease. The decrease is likely due to the formation of incomplete islands when the dots are separated by too thick of a GaN barrier. The 12 nm is sufficiently thick to reduce the strain between layers, while still allowing for complete dot formation (as shown in Fig. 4.13 (b)).

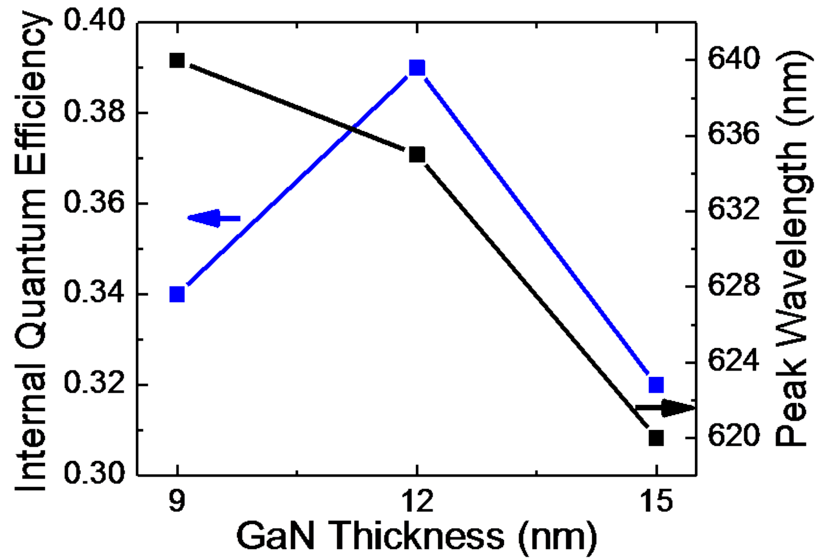

(a)

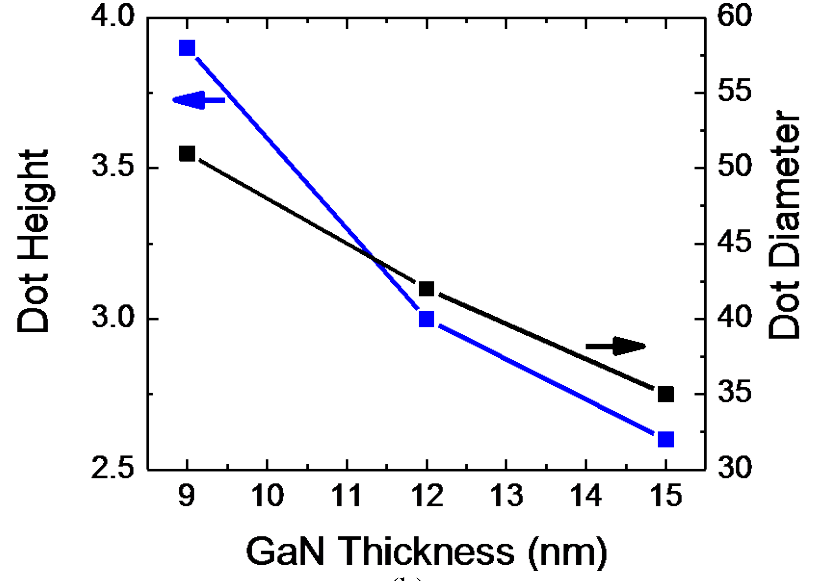

(b)

Fig. 4.13 Variation of (a) optical properties, (b) structural properties, and (c) carrier lifetimes with change in the barrier thickness.

4.5.4 Use of InGaN Barriers Between Quantum Dot Layers

The large strain present during the growth of the $In_{0.4}Ga_{0.6}N$ layer on the GaN barrier and waveguide layers may result in increased piezoelectric polarization field and lead to the formation of defects. The strain present during the growth of the $In_{0.4}Ga_{0.6}N$ layer is

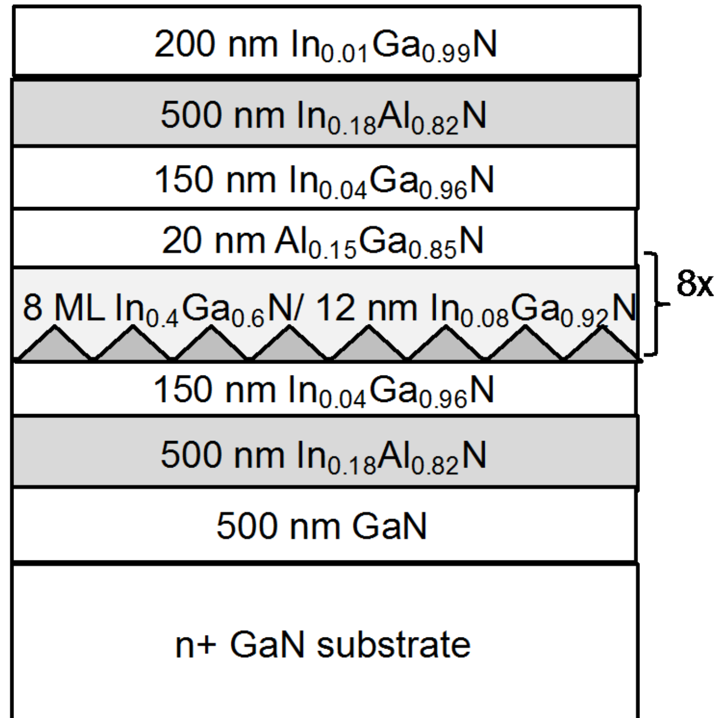

Fig. 4.14 Optimized Laser heterostructure with $In_{0.04}Ga_{0.96}N$ waveguide layers and $In_{0.08}Ga_{0.92}N$ barriers.

$\Delta a/a_0$=4.4%. It is possible to replace this layer with a low composition $In_xGa_{1-x}N$ layer, taking care to ensure that the layer can be grown on the AlGaN or InAlN cladding layer without generating dislocations and maintaining a smooth surface. $In_xGa_{1-x}N$ with a maximum composition of ~8% was found to be viable and could be grown with a smooth surface, determined through both reflective high energy electron diffraction (RHEED) during growth and atomic force microscopy imaging after growth. The composition of the layer was determined through a high resolution x-ray diffraction rocking curve. The optimized heterostructure with the $In_{0.04}Ga_{0.96}N$ waveguide is shown in Fig. 4.14. It should be noted that with the InGaN barrier, an efficiency of 51% was achievable, shown in Fig. 4.15. Additionally, the small indium in the laser waveguide increases the refractive index difference between the waveguide core and $In_{0.18}Al_{0.82}N$ cladding layer, leading to reduced cavity loss in the lasers.

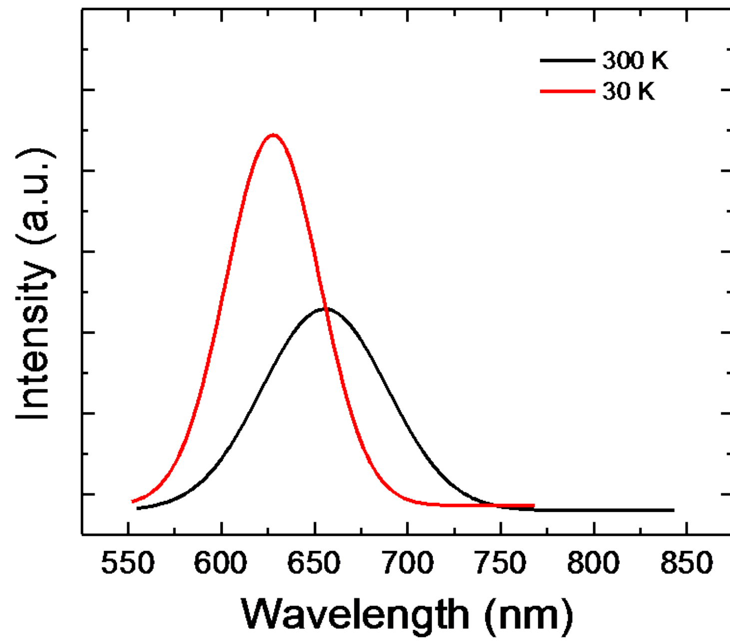

Fig. 4.15 Room temperature and 30 K temperature emission from which an internal quantum efficiency of 51% is derived.

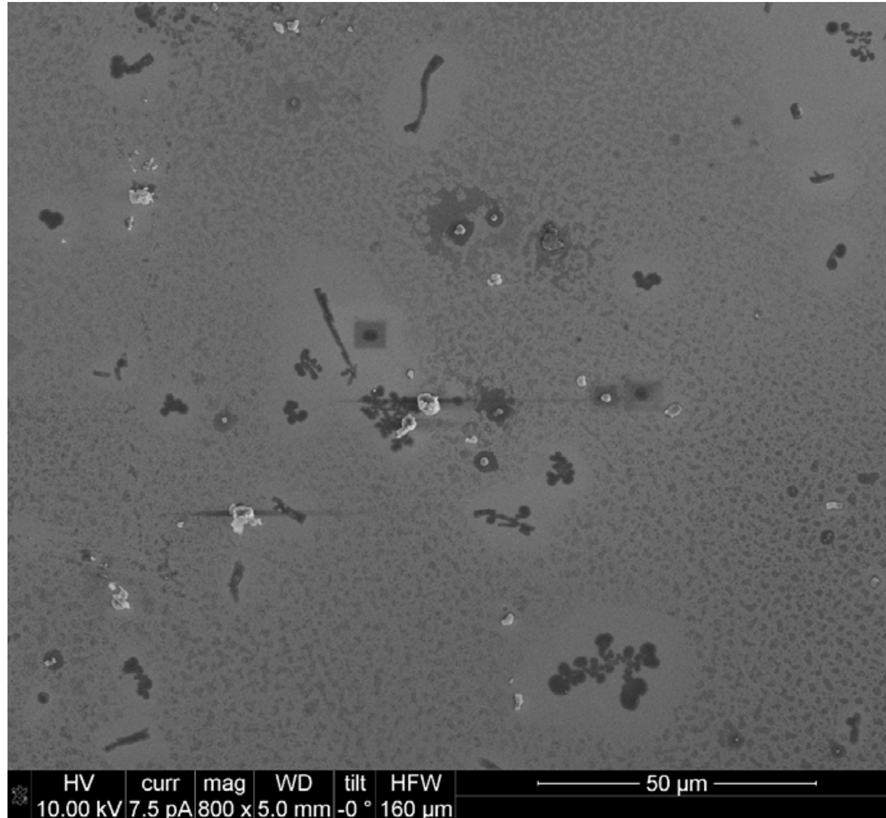

Fig. 4.16 Quantum dot sample etched to expose defects. The dark hexagonal pits correspond to dislocations.

4.5.5 Generation of Defects During the Quantum Dot Growth

As mentioned in section 4.5.4, a relatively large strain is present during the formation of the long-wavelength quantum dots (~4%). This large strain may lead to the formation of defects which was investigated by etch pit dislocation measurements. Defect-selective etching is a well-known technique for determining the dislocation density in GaN-based systems [120-123]. In the experiments done here, etch pit dislocation

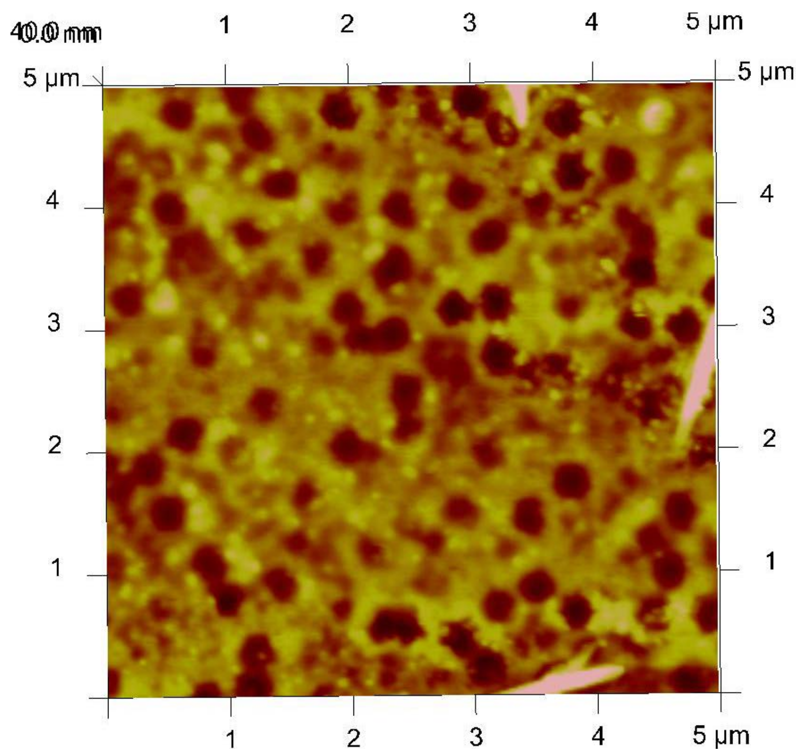

Fig. 4.17 Etch pit dislocation experiment on GaN on sapphire templates.

densities were carefully measured on bulk GaN substrates due to the relatively small number of defects in the substrate (10^5 cm^2) compared with GaN on sapphire templates (<10^8 cm^{-2}). The defects were selectively etched with a eutectic mixture of molten bases (NaOH, KOH and MgO – 53.6%, 37.3% and 9.1% by weight, respectively) at 450 ^oC. The number of etch pits were counted and correlated with the defect density. The defect density was measured in two samples, a bulk GaN substrate, grown by HVPE, and a similar substrate with 7 layers of the optimized quantum dots grown on top. Both show a defect density of ~$1.5x10^5$ cm^2. A scanning electron microscopy image of the quantum dot sample after etching is shown in Fig. 4.16. This indicates that the quantum dots do not cause the formation of threading or screw dislocations. For comparison, an atomic force microscopy image of GaN on sapphire templates after etching is shown in Fig.

4.17. The defect density in this sample, calculated from the number of hexagonal etch pits is $3x10^8$ cm^{-2}.

4.6 Summary

The performance of the red-emitting laser heterostructures can be optimized through reducing the device self-heating by reducing the diode series resistance, reducing the cavity loss by increasing the refractive index difference between the waveguide core and cladding, and by improving the internal quantum efficiency of the $In_{0.4}Ga_{0.6}N$ quantum dots. The series resistance of the laser diodes is largely caused by inefficient activation of the p-doping. The diodes are optimized through improving the p-doping by using metal modulated epitaxy during growth and the use of an all $In_{0.18}Al_{0.82}N$ cladding. $In_{0.18}Al_{0.82}N$ cladding also has the benefit of increasing the refractive index difference between the waveguide core and cladding and will reduce the cavity loss by minimizing free carrier absorption in the cladding and substrate leakage. Additionally, due to the relatively low growth temperature, high levels of hole concentrations are achievable.

A detailed study into the optimum growth conditions for the red-emitting $In_{0.4}Ga_{0.6}N$ quantum dots is has been discussed. By optimizing the InGaN thickness, nitrogen interruption time and GaN barrier thickness, the quantum dot efficiency is improved. By switching to an $In_{0.04}Ga_{0.96}N$ barrier, the efficiency can be further improved to 50% and will also increase the optical confinement factor in the lasers. Finally, through etch pit dislocation measurements, the quantum dots are found to not generate any dislocations. Further improvements in the dot efficiency will require the use of lower defect density substrates.

Chapter V

High Performance InGaN/GaN Quantum Dot Red-Emitting (λ = 630 nm) Lasers

5.1 Introduction

As discussed in chapters 1-4, III-nitride based visible light sources are being developed for full-color mobile projectors and laser displays, optical data storage, heads-up displays in automobiles, solid state lighting, plastic fiber communications, and medical applications [1, 2, 98-100]. The usual incorporation of InGaN/GaN quantum wells in the active region of lasers and light emitting diodes (LEDs) restricts their output to the green emission region [4-11]. Longer wavelengths are difficult to achieve because of the very large strain-induced polarization and material inhomogeneities in the InGaN wells with large In content. In contrast, InGaN/GaN self-organized quantum dots, grown by molecular beam epitaxy (MBE) can emit in the 630 nm (red) region. This is possible since the quantum dots are formed by strain relaxation and it has been shown that the polarization field and resulting quantum confined Stark effect (QCSE) are substantially lower than those in comparable quantum wells [11,12]. Consequently, the radiative lifetimes in the quantum dots are significantly lower than in quantum wells, allowing for the demonstration of longer wavelength visible lasers.

As an alternative to AlGaAs or InGaAlP based red-emitting devices, InGaN based

lasers have relatively small threshold current densities (J_{th}~2.5 kA/cm^2) and large temperature stability (T_0>200 K). However, for many of applications described above including in solid state lighting and mobile projectors, higher output power is desirable, between 20-70 mW [104]. Chapter 4 described optimizations to the laser heterostructure to increase the laser output power and further reduce the threshold current density to improve the overall device efficiency. In this chapter, red-emitting (λ~630 nm) quantum dots having radiative lifetime ~ 2.5 ns and internal quantum efficiency greater than 50% are used in the active region in the laser heterostructure. Edge-emitting red-emitting lasers incorporating such quantum dots have been grown and fabricated. The lasers have been characterized in terms of the steady state light-current characteristics and electroluminescence. Additionally, the temperature dependence of the lasers has been measured. Length dependent light-current characterization was performed to extract the laser cavity loss and differential gain and check the optimizations designed in chapter 4. A variable spacer layer between the active quantum dots and electron blocking layer has been introduced an optimized to further improve the laser performance. Edge-emitting red-lasers exhibit an extremely low threshold current density of 1.6 kA/cm^2, a high temperature coefficient T_0=240K, and a large differential gain dg/dn = 9x10^{-17} cm^2.

5.2 Optimized Quantum Dot Laser Heterostructure

Red-emitting InGaN/GaN laser heterostructures, shown schematically in Fig. 5.1 were grown on bulk c-plane n-GaN susbtrates. The growth of the multiple layers have been described in chapters 3 and 4, but are briefly included here for completeness. As described in chapter 4, the more commonly used AlGaN waveguide cladding layers are

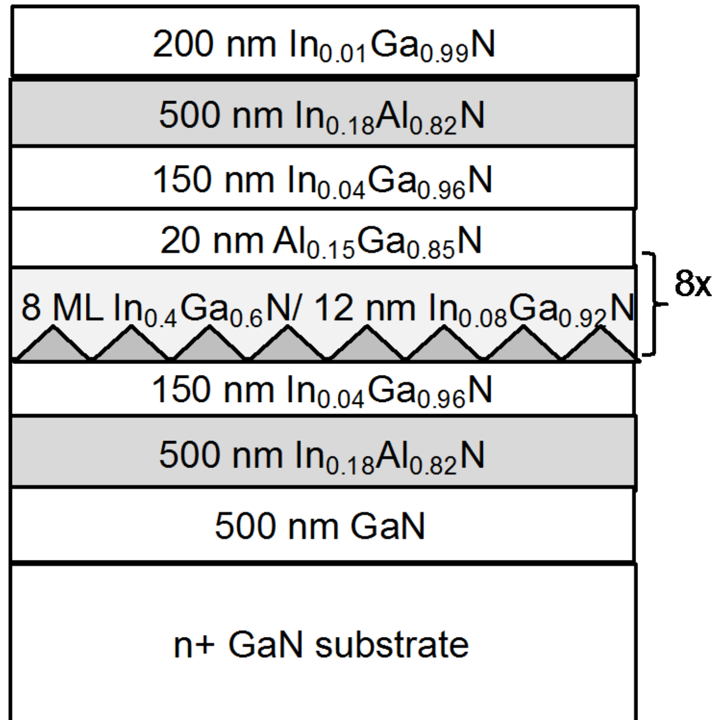

Fig. 5.1 Quantum dot laser heterostructure.

replaced by latticed-matched $In_xAl_{1-x}N$ (x=0.18). The use of this material, which provides a large index step compared with lattice mismatched AlGaN, in the cladding significantly improves confinement of the optical modes at the longer wavelengths. This leads to reduced cavity loss due to free carrier absorption from the reduced overlap of the optical mode with the heavily doped cladding. Additionally, substrate leakage will also be reduced, further minimizing the cavity loss. The optical confinement provided by $In_{0.18}Al_{0.82}N$ is comparable to that of $Al_{0.46}Ga_{0.54}N$ [81]. The growth of this alloy was done under varying growth conditions to optimize its optical and structural characteristics, as described in chapter 3. Due to the low incorporation of In at high temperatures, epitaxy must be done at a relatively low substrate temperature while ensuring the temperature is sufficiently high to provide surface mobility of Al atoms and prevent a rough surface. The best results were achieved at a substrate temperature of 497°C and with In and Al fluxes of

$2.5x10^{-8}$ and $3.4x10^{-8}$ Torr, respectively. However, for growth of the p-doped $In_{0.18}Al_{0.82}N$, a lower series resistance was possible at a growth temperature of 480°C. To compensate for the reduced substrate temperature, the In flux was lowered to $2.0x10^{8}$ Torr. It is also important to note that the relatively low growth temperature of the InAlN upper cladding layer reduces In outdiffusion from the InGaN/GaN QDs in the active region, providing an additional advantage over AlGaN based cladding. To further improve the optical confinement, the GaN barrier layers and waveguide were replaced with $In_{0.08}Ga_{0.92}N$, which also resulted in an increase in the QD internal quantum efficiency to 0.51.

As can be seen in Fig. 5.1, 8 $In_{0.42}Ga_{0.58}N/In_{0.08}Ga_{0.92}N$ layers have been incorporated in the laser heterostructure to maximize the confinement factor and gain. The additional layer compared with the chapter 3 heterostructure was chosen to account for the low density of islands on the first quantum dot layer. At the same time, adding more dot layers increases the possibility of generating dislocations, increasing the threshold current density and non-uniform hole injection. The optical confinement factor, calculated by the transfer matrix method, is 0.075 and the QD fill factor is 0.38. The thickness x of the GaN spacer layer between the QDs and the $Al_{0.15}Ga_{0.85}N$ electron blocking layer was varied from 15-60 nm. The top p-GaN contact layer has a doping of $5x10^{17}$ cm^{-3}, and the last 100 nm was grown by metal modulated epitaxy to yield an even higher doping level, as described in chapter 4. The laser diodes have a turn-on voltage of 2.7-3.3 V, a series resistance of ~6 Ω, and a reverse leakage current of 6.6 mA at -5 V. Ridge waveguide edge-emitting lasers of various cavity dimensions were fabricated using standard photolithography, dry-etching, and metallization techniques. The details of the process steps are described in Appendix B and are identical to those used in the fabrication of the

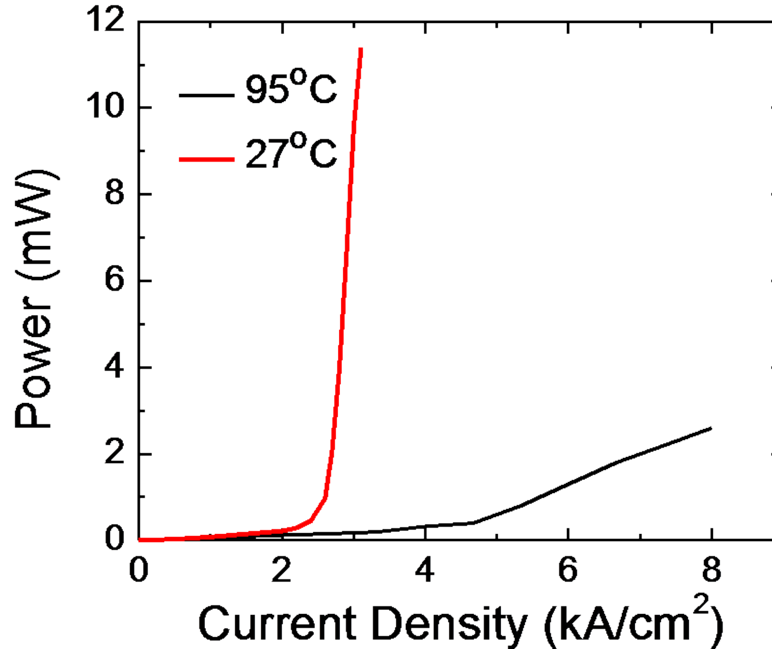

Fig. 5.2 Light-current characteristics for a 5 mm x 1 mm laser without high reflectivity facet coating.

chapters 3 lasers. The ridge is etched down to the waveguide/cladding heterointerface to minimize the cavity loss associated with side wall roughness. End mirrors were formed by cleaving the device along the m-plane and coating the cleaved facets with TiO_2/SiO_2 distributed Bragg reflectors (DBRs), to give reflectivities of ~0.7 and 0.95. The dielectric thicknesses and facet reflectivity were calculated by transfer matrix method, as described in Appendix D. Measurement of the mirror reflectivity was made on silicon wafers coated with an identical stack of dielectrics. All laser measurements described in the following sections were from the output from the low-reflectivity facet. Devices without any facet DBR coating were also characterized. No special device mounting or heating sinking were implemented in these measurements. However, as described in chapter 4, heat management may lead to further improvements in the laser performance.

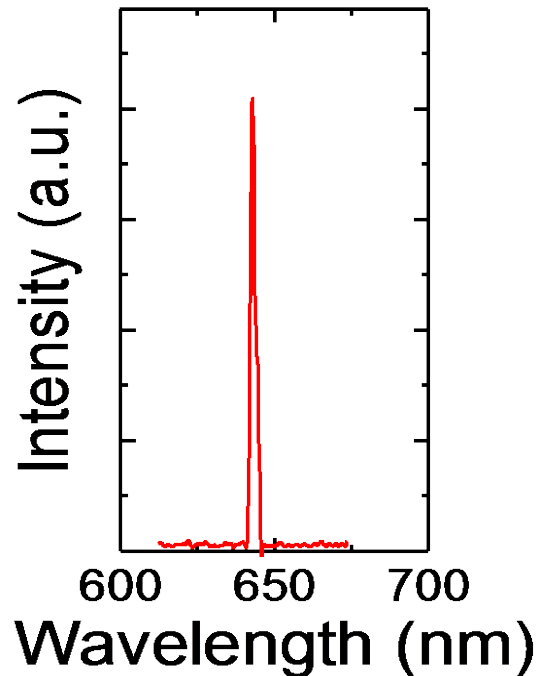

Fig. 5.3 Electroluminescence spectrum from one of the uncoated facets of the optimized laser.

5.3 DC Laser Characterization

Figure 5.2 shows the output light-current (L-I) characteristics at room temperature and 95°C under continuous wave (cw) bias condition for a device prior to facet coating, and with a GaN spacer thickness x=60 nm. The cavity width and length of this device were 5 μm and 1 mm, respectively. This 60 nm GaN spacer thickness resulted in the best performance and were used for all the measurements in sections 5.3 and 5.4. Further details on the effect of this layer and its optimization are described in section5.5 The 95°C temperature was chosen in accordance with design specifications for automobile heads-up display applications [101-104]. The threshold current density of this device is J_{th} = 2.8 kA/cm^2 at 300 K and 4.8 kA/cm^2 at the higher temperature. The corresponding output slope

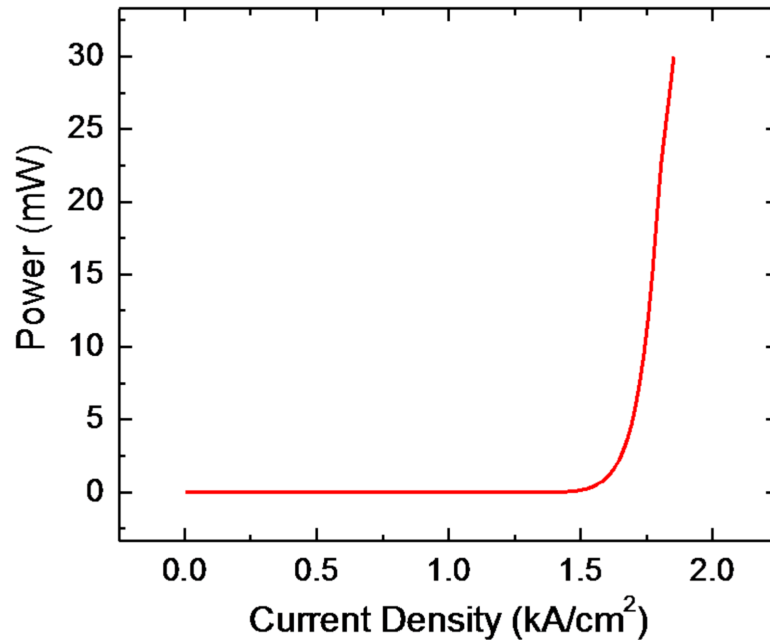

Fig. 5.4 Light-current characteristics from the low reflectivity of a DBR coated laser at room temperature under pulsed bias.

efficiency decreases from 0.42 W/A (η_d=0.23) to 0.03 W/A. This is likely due to thermallization of carriers at the elevated temperature. Further modeling of the laser active region at this higher temperature will be needed to calculated the active region temperature at an ambient temperature of 95°C. Device packaging or active cooling techniques may be necessary to improve the high temperature performance further. The output spectral characteristics at 300K at an injection of 1.1 J_{th} is shown in Fig. 5.3. The minimum measured linewidth is 8 Å at a peak emission of 630 nm.

Figure 5.4 shows the L-I characteristics of a 10 μm x 1 mm device at 300 K, with DBR facet coatings (0.7 and 0.95), and x= 60 nm, and under pulsed (1% duty cycle) biasing conditions. The laser exhibits J_{th}=1.7kA/cm^2, a slope efficiency of 0.41 W/A, and a wall plug efficiency of 1.6%. It should be noted that while there is still room for

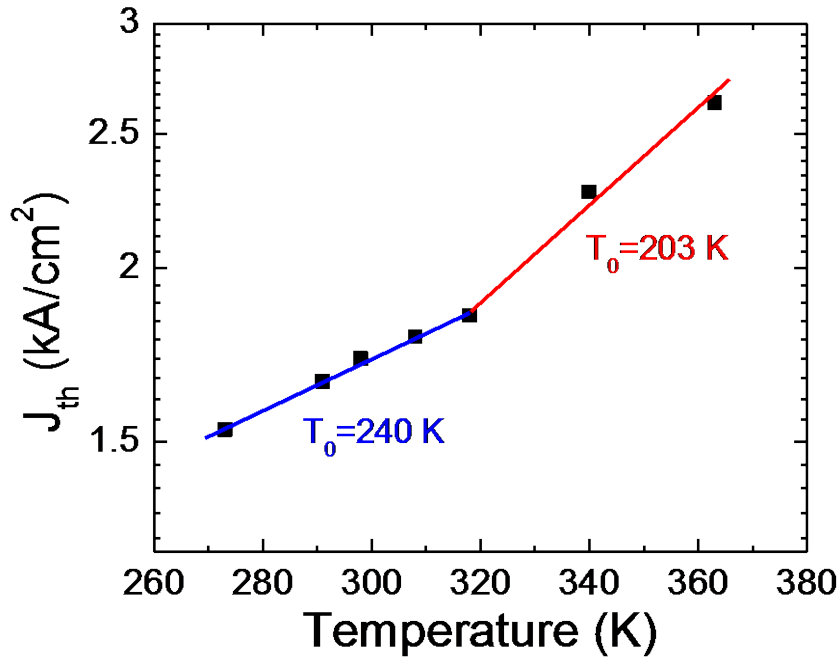

Fig. 5.5 Temperature dependence of the threshold current density of a laser with DBR coating.

improvement, this efficiency is 10x larger than in the heterostructure described in chapter 3. This is due to the increased internal quantum efficiency of the quantum dots and the increased optical confinement factor in this heterosturcutre. The maximum output power is 30 mW, putting it in the range needed for projector and heads-up display applications. The temperature dependence of J_{th} under pulsed biasing (1% duty cycle) for the laser of Fig. 5.4 is shown in Fig. 5.5. The values of T_0 quoted in the figure are obtained by analyzing the data with the relation: $J_{th}(T) = J_{th}(0)\exp(T/T_0)$. These high values of T_0 are extremely encouraging and result from the large band offsets and good carrier confinement in the InGaN/GaN dot heterostructures. The measured T_0=240 K up to 320 K is comparable with the value reported in the chapter 3 heterostructure, and the degradation at higher temperatures is likely due to the thermallization of carriers at elevated

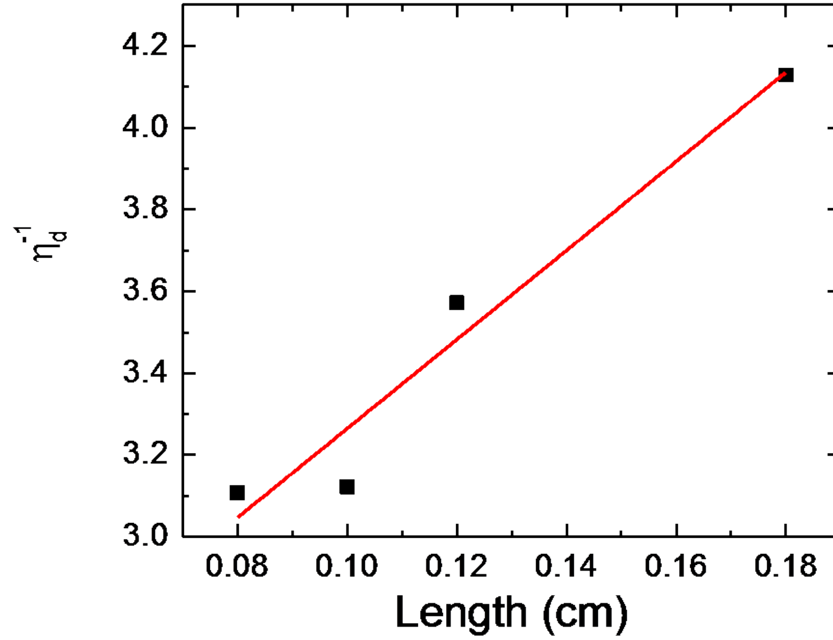

Fig. 5.6 Variation of inverse differential quantum efficiency with cavity length.

temperatures. In contrast, red-emitting lasers made with InGaAlP/GaAs heterostructures have J_{th}~6-8 kA/cm^2 and T_0~60-80 K [17-18].

5.4 Length Dependent Characterization and Differential Gain

Similar to the measurements carried out in chapter 3, length dependent characterization of the lasers was performed to measured the laser cavity loss and differential gain. Light-current measurements have been made on lasers of varying cavity lengths and the differential quantum efficiency η_d and J_{th} were recorded for each length. Figure 5.6 shows the variation of η_d^{-1} with cavity length. From this data, a value of η_i = 0.49 is derived using the relation:

$$\frac{1}{\eta_d} = \alpha_i L \ \ln\frac{1}{\sqrt{R_1 R_2}} + \frac{1}{\eta_i} \tag{5.1}$$

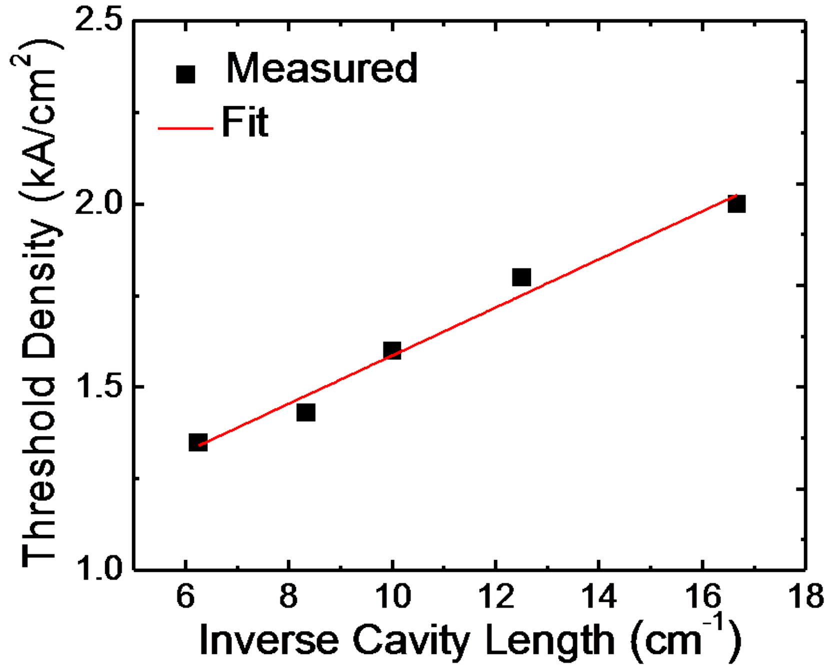

Fig. 5.7 Variation of threshold current density with inverse cavity length.

where η_d is the differential efficiency of the laser, R_1 and R_2 are the mirror reflectivities, L is cavity length, and α_i is the cavity loss. The cavity loss is determined to be 8.3 cm^{-1} in these heterostructures, compared with 25 cm^{-1} in the lasers described in chapter 3. The reduced cavity loss is due to smaller free carrier absorption and substrate leakage with the presense of the all $In_{0.18}Al_{0.82}N$ cladding. Measured values of J_{th} are plotted against inverse cavity length in Fig. 5.7. The differential gain dg/dn is calculated by analyzing this data with the relation the relation [93]:

$$J_{th} = J_{th}^{0} + \frac{qd}{\Gamma \eta_i \tau_r \frac{dg}{dn}} \left[\alpha_i + \frac{1}{2L} ln\left(\frac{1}{R_1 R_2}\right) \right] \quad (5.2)$$

where d is the active region thickness calculated as the number of dot layers times the effective dot height, Γ is the product of the optical confinement factor simulated by the transfer matrix method (0.075) and the fill factor (0.38), τ_r is the measured radiative

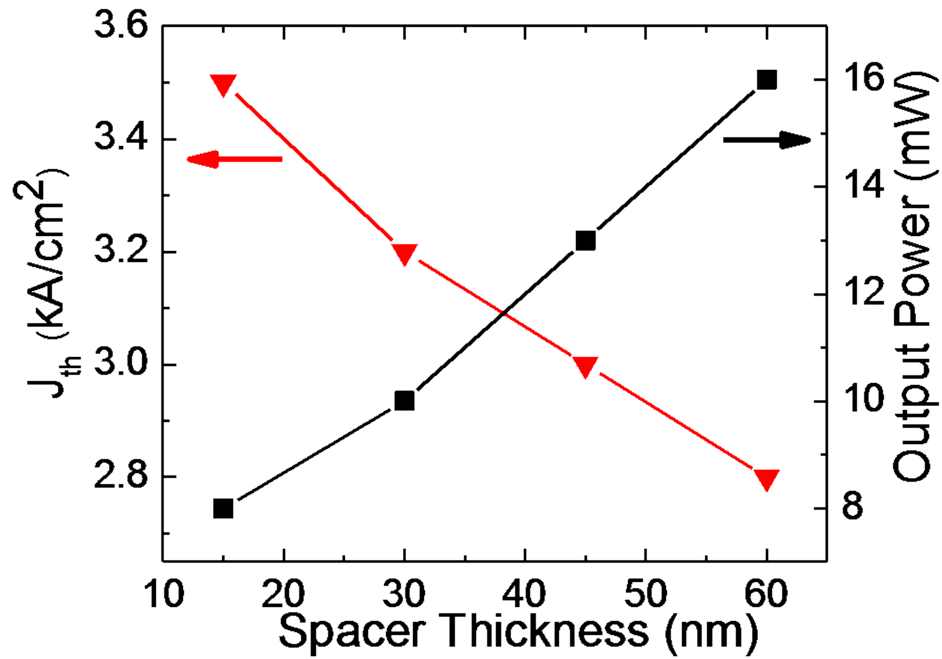

Fig. 5.8 Variation of threshold current density and maximum output power from lasers with no facet coating as a function of spacer thickness.

lifetime (2.5 ns), and R_1 and R_2 are 0.7 and 0.95, respectively; the transparency current density J_{th}^0 and dg/dn are fitting parameters for this function. A value of differential gain dg/dn = 9.0 x 10^{-17} cm^2 is derived along with a value of J_{th}^0 = 550 A/cm^2. This value of differential gain is ~2x larger than the value found in the previous heterostructure, described in chapters 3. From comparable length dependent measurements, described in chapter 3, dg/dn = 3.8 x 10^{-17} cm^2 was measured, while from small signal modulation measurements dg/dn = 5.3 x 10^{-17} cm^2 was derived. Such as large value of differential gain is comparable with shorter wavelength blue- and green-emitting quantum dot lasers [19, 20]. It is ~ 5x larger than values reported in shorter wavelength blue-emitting InGaN/GaN quantum well based lasers.

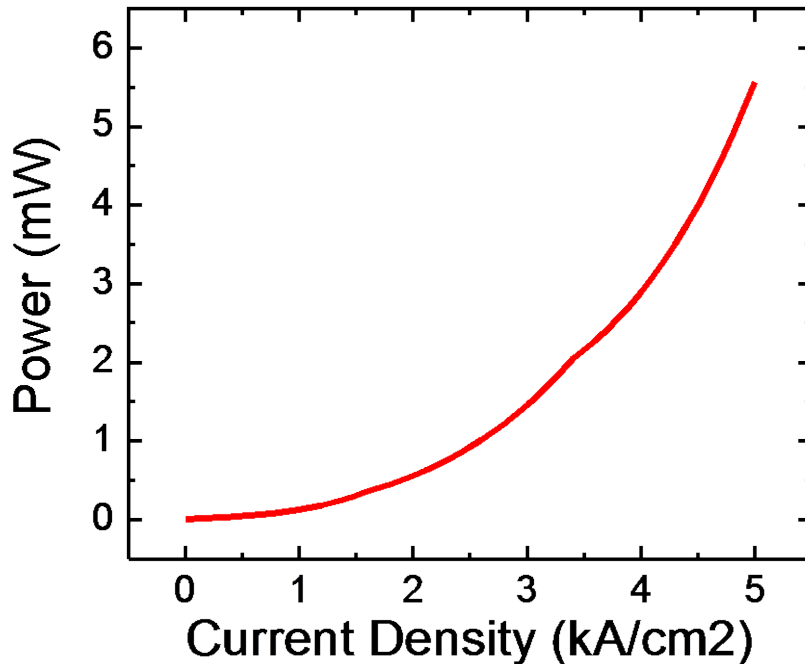

Fig. 5.9 Light current characteristics of a laser (LED) with no electron blocking layer showing no threshold.

5.5 Variation of Spacer Layer Thickness

In the III-nitride material system, there exists a large difference between the effective carrier masses, with $m_e^*{\sim}0.2m_0$ and $m_{hh}^*{\sim}1.2m_0$, leading to several deleterious effects. The combination of large triangular potential barriers due to the polarization field and the large hole masses leads to accumulation of holes in the first one or two quantum well (or dot) layers. Additionally, a non-negligible fraction of electrons, with their relatively small carrier mass, have a tendency to overshoot the quantum wells and recombine in the p-side of the LED or laser. The combination of these effects has led to the ubiquitous incorporation of an electron blocking layer (EBL) in III-nitride based optoelectronic devices to prevent electron leakage. The

effectiveness of such an EBL will depend greatly on the placement of the layer in the laser (or LED heterostructure). To study the effects of the placement of the EBL, a variable spacer layer has been incorporated into the laser heterostructures, shown schematically in Fig. 5.1. Light-current characteristics were measured from four devices with x = 15 nm, 30 nm, 45 nm, and 60 nm. A summary of the threshold current density and maximum output power from these devices is shown in Fig. 5.8. As can be clearly seen, an increase in the spacer thickness results in higher output power and lower threshold current density. Following this trend, a fifth device with no spacer layer, effectively $x = \infty$, showed no non-linearity in the light-current characteristics, shown in Fig. 5.9, demonstrating the importance of the presence of the EBL. The separation between the EBL and quantum dots is important, likely due to the role is plays in band bending near the active region due to the piezoelectric polarization field.

5.6 Summary

The growth of red-emitting $In_{0.4}Ga_{0.6}N/In_{0.08}Ga_{0.92}N$ quantum dots is described here along with their incorporation into high power ridge waveguide laser heterostructures. In comparison with other material systems (AlGaAs, InGaAlP), the laser described in the previous chapters were characterized by small threshold current density and excellent temperature stability. However, large cavity loss and relatively small internal quantum efficiency in the active layer led to restricted output power and efficiency. Through the careful optimization of the laser heterostructure, described in chapter 4, lasers were fabricated with higher efficiency quantum dots (η_i =0.51), and improved $In_{0.18}Al_{0.82}N$ cladding. The lasers were fabricated and characterized in terms

of the light-current characteristics, showing a further reduced threshold current density (1.6 kA/cm^2) and higher output power (up to 30 mW). Length dependent characterization of the lasers was also performed, from which a cavity loss of 8.3 cm^{-1} is derived. This is substantially smaller than the value in the pervious laser heterostructure and is attributable to the use of $In_{0.18}Al_{0.82}N$ cladding. The measured differential gain is 9.0 x 10^{-17} cm^2, which is also improved and comparable with shorter wavelength green and blue-emitting InGaN/GaN quantum dots. Finally, a spacer layer between the InGaN quantum dot active region and AlGaN electron blocking layer is introduced and optimized to maximize the laser output power. It is found that 60 nm results in the highest output power and lowest threshold current density.

Chapter VI

Bias Modulation of InGaN/GaN Quantum Dot Lasers and Measurement of Auger Recombination

6.1 Introduction

Visible lasers have many potential applications including solid state lighting, optical date storage, and in plastic fiber communications [1, 2, 98-100]. While the previous chapter has focused on steady state characteristics necessary for these applications, dynamic characterization of the quantum dot lasers is useful in determining the maximum modulation frequency for optical communication. Additionally, important device and material characteristics can be determined from small- and large-signal analysis of these lasers [122-123]. Under a damping limited operation for the laser diodes, the resonant frequency is related to the injection current through the device differential gain, dg/dn [124]. Damping in these semiconductor laser diodes is typically attributed to gain compression, and these two parameters can be extracted through careful analysis of the laser small signal response. This chapter describes the small signal characteristics of red-emitting InGaN/GaN quantum dot lasers and demonstrates their potential for use in plastic fiber communication systems.

Nitride-based quantum well light emitting diodes and lasers suffer from a strong inherent polarization field, and the associated band bending causes poor electron-hole

wavefunction overlap [25], poor radiative efficiencies, blueshift of peak emission with current density due to the quantum confined Stark effect (QCSE) and a high leakage of carriers in devices incorporating such QWs in the active region. Additionally, a larger than expected Auger recombination coefficient is typically measured [125-128], which should ideally be very small in such wide bandgap material [44], which has been suggested as the cause of the severe efficiency droop typically observed in quantum well based light emitting diodes. To study the gain and Auger characteristics in the red-emitting quantum dot lasers, small and large signal analysis shown in this chapter. From analysis of these characteristics, differential gain, dg/dn, gain compression factor, ε, and the Auger recombination coefficient, C_a, are derived.

6.2 Small Signal Modulation of InGaN/GaN Quantum Dot Laser Diodes

Epitaxial growth of the separated confinement heterostructure (SCH) lasers has been described earlier in chapter 3, but is given here in brief for completeness. The heterostructures were grown on the Ga-polarized face of n+ c-plane (0001) GaN substrates (defect density ~ 10^6 cm^{-2}) by molecular beam epitaxy (MBE). The QD laser heterostructure is shown in Fig. 6.1. Growth of the n-type buffer layer is followed by that of the n-type lower cladding, 7 periods of 8 monolayer $In_{0.4}Ga_{0.6}N$ / 17 nm GaN QD layers inserted at the center of a $In_{0.02}Ga_{0.98}N$ waveguide layer, p-type $Al_{0.15}Ga_{0.85}N$ electron blocking layer, p-type upper cladding layer and finally an $In_{0.01}Ga_{0.99}N$ p-contact layer (p = 5 x 10^{17} cm^{-3}). It may be noted that the cladding layers consist of a combination of $Al_{0.07}Ga_{0.93}N$ and lattice-matched $In_{0.18}Al_{0.82}N$ for better mode confinement at 630 nm. The average In composition in the quantum dots was obtained from energy-dispersive X-ray measurements to be ~ 40 %.[4] Ridge waveguide edge-emitting lasers of various cavity

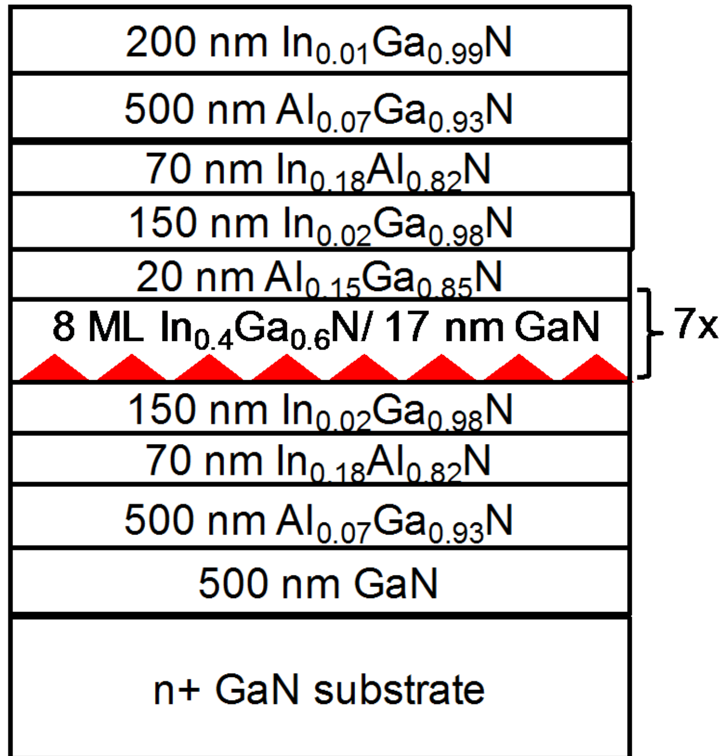

Fig. 6.1 Laser heterostructure used for small and large signal modulation measurements described in chapter 4, grown by molecular beam epitaxy. The lasers are fabricated into ridge geometry lasers, using the process outlined in Appendix B.

lengths were fabricated using standard photolithography, dry-etching and contact metallization techniques, described in detail in Appendix B. The ridge width is 4 μm and the cavity length is 800 μm for measurement of the small signal response of the red lasers. The mirrors were formed by cleaving the devices along the m-plane and subsequently coating the facets with electron-beam evaporated TiO_2/SiO_2 distributed Bragg reflectors (DBRs) to attain reflectivities of ~0.7 and 0.95. The light-current (L-I) characteristics of a typical device (under cw operation) is shown in Fig. 6.2, indicating a threshold current density of 2.4 kA/cm^2. This laser has been characterized at room temperature, maintained by a thermoelectric cooler, shown schematically in Appendix C with the Ge detector replaced with a Si detector. As discussed in earlier chapters it should be noted that while

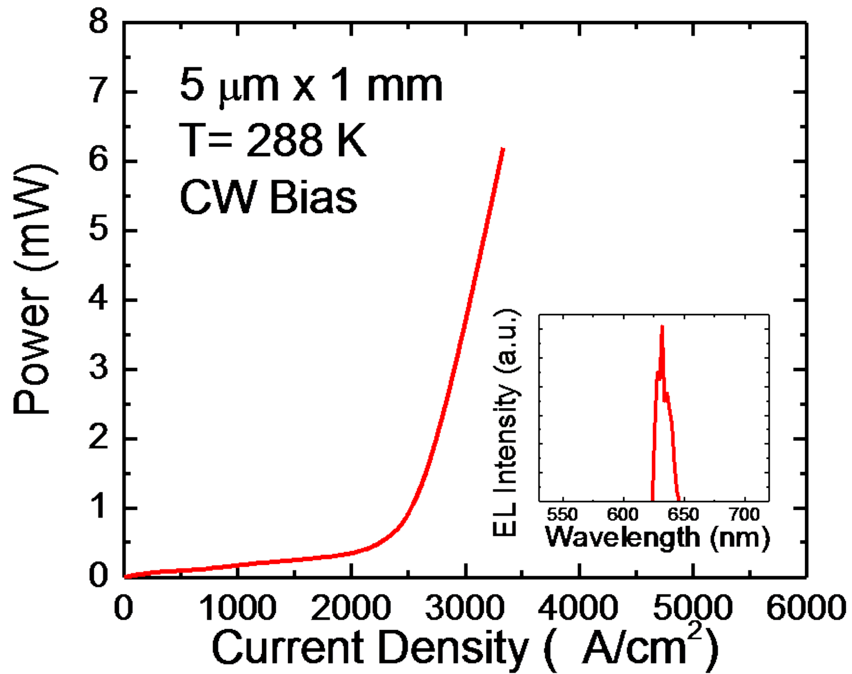

Fig. 6.2 Light-current characteristics of a typical laser fabricated with the heterostructure shown in Fig. 6.1. The output spectral characteristics are shown at 2.7 kA/cm^2 (1.1J_{th}).

the back of the substrate may be this temperature, the active region may be considerably hotter [88, 106]. The spectral characteristics of this device are shown in the inset of Fig. 6.2 at a bias of 1.1J_{th}. The peak emission of this laser occurs at 630 nm. The small-signal modulation response of 800 μm long ridge waveguide lasers was measured under pulsed bias conditions (5 μs pulses; 0.5 % duty cycle) using a sweep oscillator with a bias T, low-noise amplifier, a high-speed silicon detector and a spectrum analyzer. A detailed depiction of the setup is shown in Appendix C. The modulation response is shown in Fig. 6.3. The indicated currents refer to the DC bias current. A 10 dBm sinusoidal signal of varying frequency (100 MHz to 3 GHz) is superimposed on the DC bias with the sweep oscillator and bias T. Light from the lasers is collected with a multimode fiber and detected

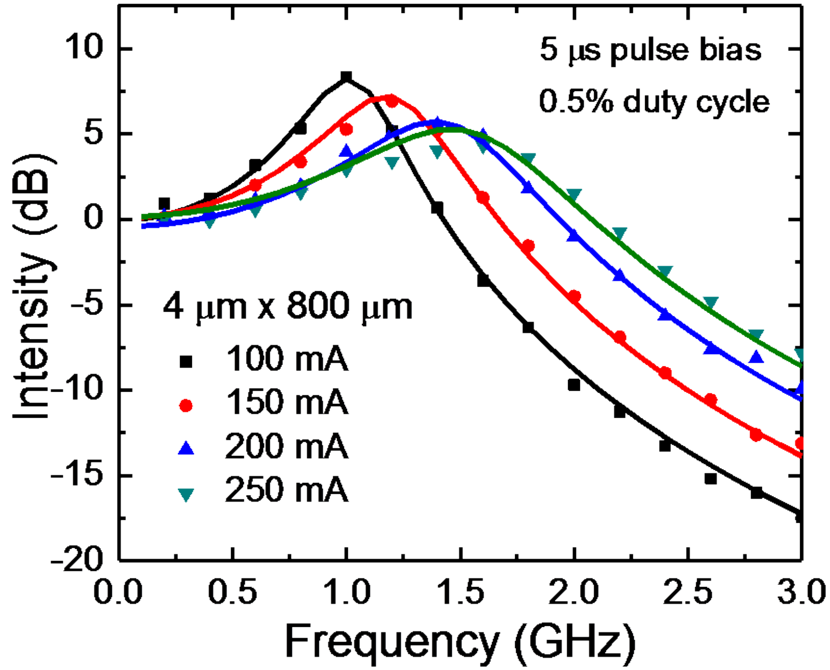

Fig. 6.3 Small signal modulation response of the $In_{0.4}Ga_{0.6}N$/GaN quantum dot laser diodes (points) and fit of the measured response curves (solid lines).

with a Newport D15 40 GHz high speed detector. The small signal response is amplified and analyzed with an electrical frequency analyzer. The relative change in AC intensity from the lowest measured frequency (100 MHz) are plotted. The measured data have been analyzed with the damped oscillator small signal response model:

$$|M(f)|^2 \propto \frac{1}{\left(f^2-f_r^2\right)^2+\left(\frac{\gamma_d}{2\pi}\right)^2 f^2} \tag{6.1}$$

where γ_d is the damping factor and f_r is the resonance frequency of the response. A -3 dB modulation bandwidth of 2.4 GHz was measured at the highest DC injection current of 250 mA and the resonance frequency at this injection level is 1.6 GHz. A higher -3 dB modulation bandwidth may be possible with higher injection currents but this was not possible due to device and facet heating, and no measurements at higher injections were

possible. The relatively fast frequencies that these lasers can be modulated at may allow for their use in plastic fiber communication systems up to ~3.9 gigabits per second which have pass bands at this wavelength range. The relatively small -3dB modulation frequency, in comparison with InGaAs/GaAs quantum dots may however be due to the relatively large carrier masses in this material system [129].

6.3 Differential Gain and Gain Compression in Red-Emitting Quantum Dots

In addition to demonstrating the potential for these lasers to be used in optical communication systems, small signal analysis can also be used to analyze the gain characteristics of the InGaN quantum dot lasers. The lasers have been fit with the damped oscillator response given in Eqn. 6.1 and the resultant resonant frequencies and damping coefficients are extracted. The differential gain dg/dn is related to the small-signal modulation data using the relation:

$$f_r = \frac{1}{2\pi}\left[\frac{v_g \Gamma (I - I_{th}) \frac{dg}{dn} \eta_i}{L w d_{act} q}\right]^{\frac{1}{2}} \tag{6.2}$$

where v_g is the photon group velocity, Γ is the confinement factor, η_i is the QD internal quantum efficiency, L is the cavity length and d_{act} is the thickness of the active region. A value of η_i = 35.9% was obtained from temperature and excitation dependent photoluminescence measurements made on the red-emitting quantum dots (4). The confinement factor is estimated as the product of the transverse confinement factor Γ_z. where z is the growth diction (0001), and the quantum dot fill factor, Γ_{xy}. The procedure for calculating the transverse optical confinement factor is given in Appendix D, with the appropriate insertion of the laser structure in the code in Appendix D.1. Unlike a quantum well, the in-plane optical confinement factor can not be considered unity with the discrete

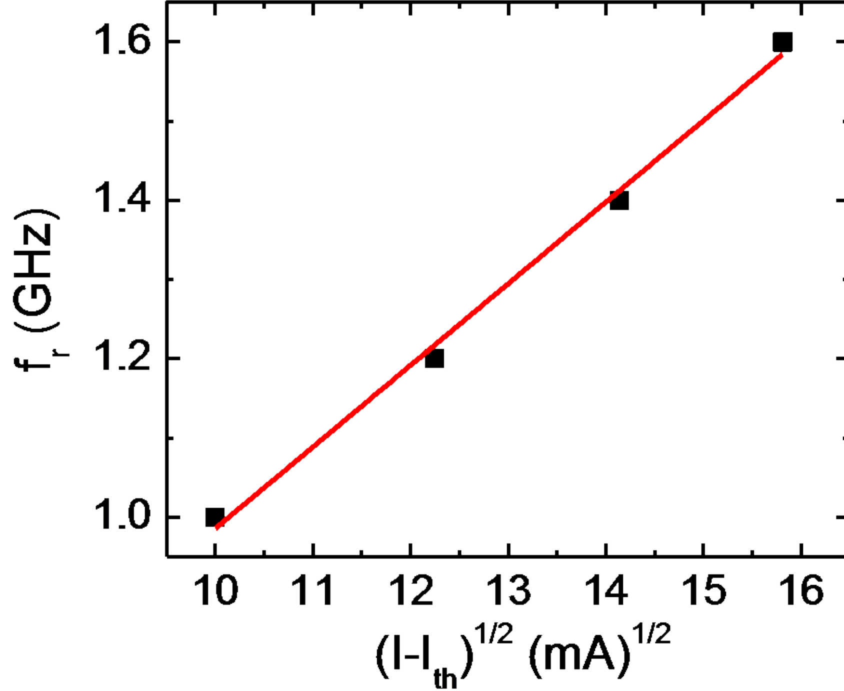

Fig. 6.4 Variation of the laser resonant frequency with the square root of the injection current above threshold. The plotted resonant frequencies are fit using the damped oscillator model to the measured response curves in Fig. 6.3.

and discontinuous quantum dots. The quantum dot fill factor is used as in-plane confinement factor and is calculated as follows. The pyramidal dots with a base width of 37 nm and height of 5 nm are modeled as equivalent flattened cubes of the same volume and base width with a 3.55 nm effective height. Comparing the volume of an array of these cubes with the volume of the nominal thickness of the deposited InGaN (8 ML), given by the change in reflective high energy electron diffraction (RHEED) pattern from 2D to 3D growth, results in a fill factor of 0.35. Taking the fill factor into account, the confinement factor is 0.025 for the laser heterostructure. The plot of f_r vs. $(I-I_{th})^{1/2}$, obtained from the data of Fig. 6.3, is shown in Fig. 6.4. The slope of the plot is 3.3 GHz/mA$^{1/2}$, from which a differential gain dg/dn = 5.3 x 10^{-17} cm^2 is derived from eqn. 6.2. The value is

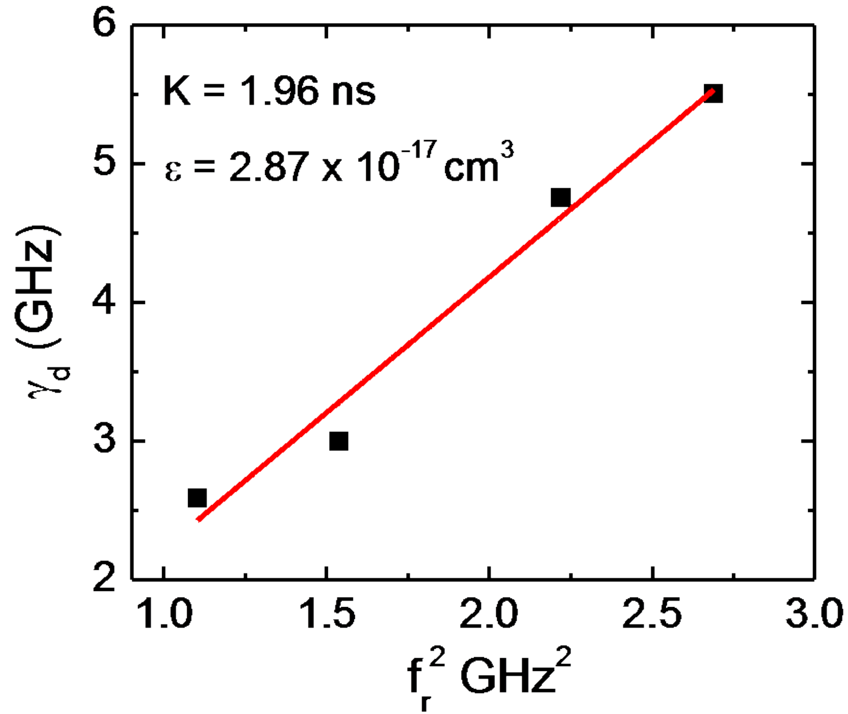

Fig. 6.5 Variation of the laser resonant frequency with the square root of the injection current above threshold. The plotted resonant frequencies are the values fit using the damped oscillator model to the measured response curves in Fig. 6.3.

comparable to that for shorter wavelength (λ = 430 nm) strained and strain compensated InGaN/GaN quantum well lasers [130, 131]. It should be noted that this is comparable with values derived from length dependent characterization of these red InGaN/GaN QD lasers (3.8 x 10^{-17} cm^2). However, it is considerably smaller than In(Ga)As/GaAs quantum dot lasers [132]. This is largely due to the large carrier effective masses in these materials.

It is known that hole injection is non-uniform in InGaN/GaN multi-quantum well light-emitting diodes (LEDs) and lasers and a similar situation exists in multi-quantum dot devices. Most of the injected holes pile up in the first couple of wells/dots from the injecting p-layer, leading to increased carrier density, and hot-carrier effects, including gain compression. Under gain compression limited modulation response in the devices

under study, the damping factor γ_d is related to f_r by the approximate relationship: $\gamma_d = Kf_r^2$. The proportionality constant is the K-factor which is a measure of the damping limited bandwidth. A plot of γ_d versus f_r^2 obtained from analysis of the data of Fig. 6.3 with Eqn. 6.1 is illustrated in Fig. 6.5. A value of K = 1.96 ns is derived from the slope of this plot. The maximum modulation bandwidth of the lasers under this damping model is then given by $f_{-3dB}=2^{3/2}\pi/K=4.53$ GHz. These higher values of bandwidth (beyond 2.5 GHz) may be accessible if higher injection currents could be reached, perhaps through device packaging or contact improvement. Under the gain compression limited bandwidth model, a value of the gain compression factor $\varepsilon = 2.87 \times 10^{-17}$ cm^3 is then derived from the approximate relationship:

$$K \cong 4\pi^2 \left(\frac{\epsilon}{v_g \frac{dg}{dn}} + \tau_p \right) \tag{6.3}$$

where τ_p is the cavity photon lifetime. This value of ε is comparable to those measured for In(Ga)As/GaAs quantum dot lasers [133].

In summary, small-signal modulation measurements on InGaN/GaN ridge waveguide quantum dot lasers emitting at λ = 630 nm were performed. The lowest measured threshold current density is 2.4 kA/cm^2. The maximum measured -3 dB modulation bandwidth is 2.4 GHz. A differential gain of 5.3×10^{-17} cm^2 and a gain compression factor of 2.87×10^{-17} cm^3 are derived from the modulation data.

6.4 Large Signal Modulation of InGaN/GaN Quantum Dot Lasers

Nitride based light emitting diodes suffer from droop where the light output efficiency continuously and severely decreases with injection after a peak at very low biases. One potential culprit of this phenomena that has been suggested is Auger

recombination [33, 37, 39]. While large bandgap III-Nitride based quantum wells are expected to have relatively small levels of Auger recombination, which is proportional to $(k_BT/E_g)^{3/2}\exp(-E_g/k_BT)$, measured values are typically orders of magnitude larger. It is therefore important to investigate if quantum dot based devices suffer from similar unexpectedly large Auger recombination coefficients. Previously, luminescence techniques have been used to measure Auger recombination in InGaN materials and heterostructures [44, 81, 134-135]. The Auger coefficient can also be derived from large signal modulation measurements made on lasers [136, 137].

These measurements were made on identical devices described earlier in this chapter, shown schematically in Fig. 6.1 with L-I characteristics shown in Fig. 6.2. When a laser is electrically switched from the off-state to a bias state above threshold, there is a turn-on delay between the electrical pulse and the coherent optical output pulse. For the laser to reach threshold, the carrier concentration in the quantum dots, n, must reach it's threshold value, n_{th}. Below threshold, carriers are injected at a constant rate from the injection current density and lost due to Shockley-Read-hall (SRH) recombination, spontaneous recombination, or Auger recombination. From the laser rate equations for injected carriers in the active region, the turn-on delay time τ_d can be expressed as

$$\tau_d = qV\int_0^{n_{th}} \frac{1}{I - qVR(n)} dn \tag{6.4}$$

where V is the active region volume and R(n) is the total carrier recombination rate given by

$$R(n) = \frac{n}{\tau} = A_{nr}n + R_{sp}n^2 + C_a n^3 \tag{6.5}$$

Here τ is the carrier lifetime, A_{nr} is the Shockley-Read-Hall (SRH) recombination

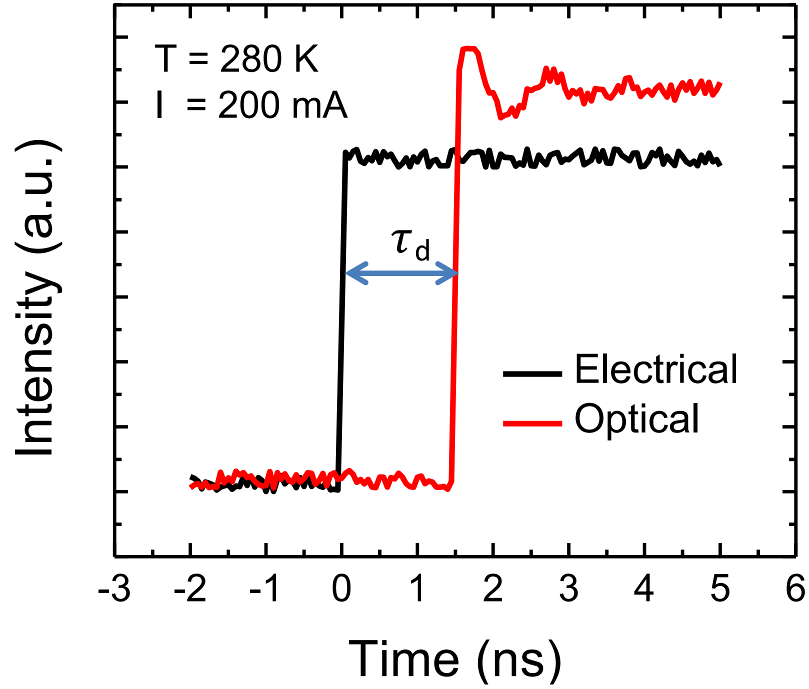

Fig. 6.6 Measured electrical and optical signals showing the laser diode response to a large signal current pulse driving the laser above threshold. The time delay, τ_d, is indicated in the plot.

coefficient and R_{sp} is the radiative recombination coefficient. It may also be remembered that

$$J_{th} = qdn/\tau = qdR(n_{th}) = qd(A_{nr}n_{th} + R_{sp}n_{th}^2 + C_a n_{th}^3) \tag{6.6}$$

where d is the thickness of the laser active region. Therefore accurate measurement of the turn-on delay time and calculation of A_{nr} and R_{sp} allow self-consistent determination of n_{th} and C_a using Eqns. (6.4)-(6.6).

6.5 Measurement of Auger Recombination Coefficient in InGaN Quantum Dots

In the large-signal modulation measurement the laser is biased with 500 ns pulses (under 1% duty cycle) having a rise time of 100 ps (20 - 80 %) in switching from current I = 0 to I > I_{th}. An impedance matching unit is used to reduce reflection and distortion of the pulses.

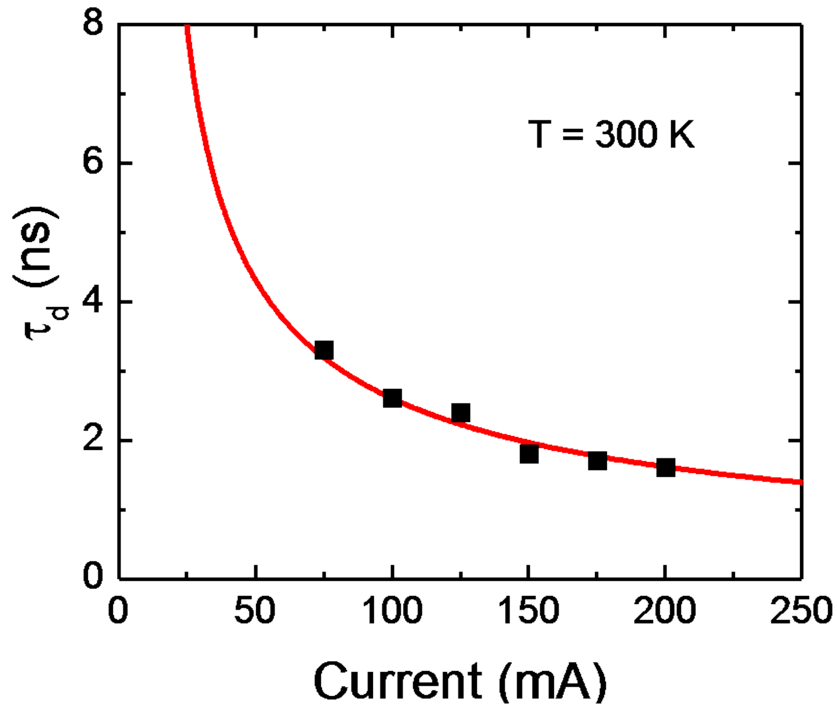

Fig. 6.7 Variation in the measured values of the delay time with current injection at room temperature. The solid line indicates the calculated delay time with injection.

The measurement system is shown schematically in Appendix C and is similar to the small signal analysis setup with the amplifier and electrical spectrum analyzer replaced with a high speed oscilloscope. The coherent output light from the laser is collected with a fiber coupled to a high-speed GaAs photodetector and temporally resolved with a 2 GSa/s sampling oscilloscope. The electrical pulsed bias is also routed to the oscilloscope and concurrently measured, as shown in Fig. 6.6 at 280 K with an injection of 100 mA. It should be noted that the quoted temperature is the Peltier cooler temperature, and the actual active region temperature may be considerably higher. The relaxation oscillations in the optical pulse are clearly observed. Thus the turn-on delay τ_d can be measured after properly accounting for the delays in the fiber, rf cable and the detector. The measured values of τ_d at room temperature for different injection currents from 50 to 200 mA are

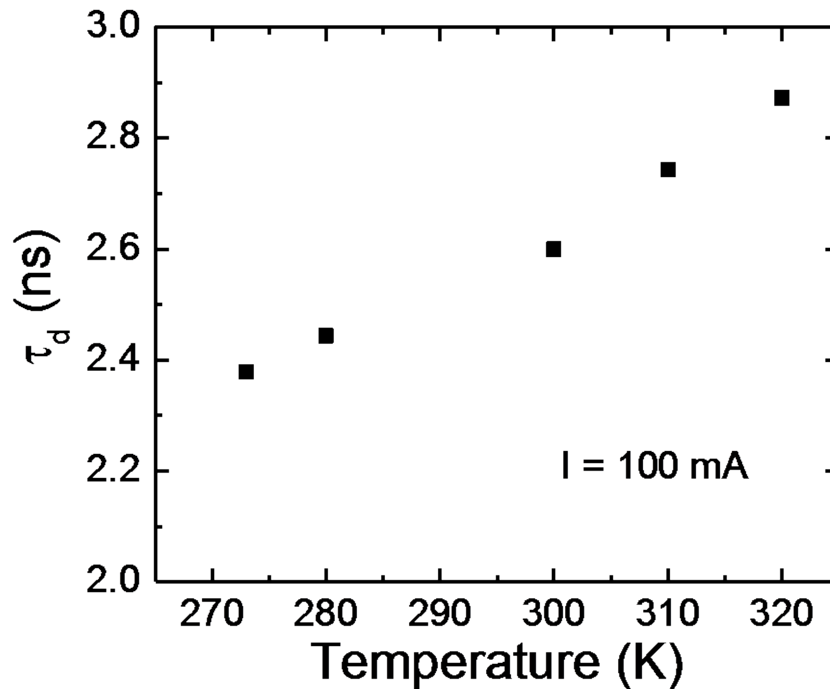

Fig. 6.8 Variation in the time delay with temperature at a current bias of 100 mA. The small increase in delay with temperature is likely due to electron-hole scattering in the quantum dots, as described in chapter 2 and section 6.5.

plotted in Fig. 6.7. The delay time decreases with increasing current due to a decrease of carrier lifetime. The solid curve is the calculated using the model described in the previous section. The current-dependent delay times were also measured at different temperatures. Figure 6.8 shows a plot of τ_d at a fixed injection current of 100 mA plotted as a function of temperature. It is evident that the delay time increases with increase of ambient temperature. This is likely due to electron hole scattering in the quantum dots and is discussed in more detail in sections 2.4 and 6.5.

In order to analyze the temperature and injection dependent time delay data and to accurately determine the Auger recombination coefficient, it is necessary to calculate R_{sp} and A_{nr}. The value of R_{sp} is calculated using the Fermi golden rule with an eight-band $\mathbf{k} \cdot \mathbf{p}$

Electron Traps			Hole Traps		
ΔE (eV)	σ (cm^2)	N_T (cm^{-3})	ΔE (eV)	σ (cm^2)	N_T (cm^{-3})
0.24	5.154×10^{-16}	2.11×10^{15}	0.387	5.08×10^{-17}	3.62×10^{16}
0.461	2.242×10^{-16}	5.12×10^{15}	0.595	1.136×10^{-16}	6.25×10^{16}
0.674	1.22×10^{-15}	4.63×10^{15}			

Table 6.1 Characteristics of deep level traps in GaN, grown by plasma-assisted molecular beam epitaxy, obtained from transient capacitance measurements.

description of the bands. The interface strain and polarization field in the dots are taken into account in the model. Thus at room temperature, $R_{sp} = 1.4 \times 10^{-11}$ cm^3 s^{-1} is derived. This value is very similar to those reported for nitride materials by others [137-138]. Measurement of A_{nr} is carried out by independent transient capacitance measurements made on GaN n^+-p homojunction diodes to determine the presence of deep level traps in PAMBE-grown GaN, assuming that in the laser heterostructure deep traps in the GaN barrier regions between the QD layers and the $In_{0.02}Ga_{0.98}N$ waveguide layer lead to non-radiative recombination. As discussed in the lifetime characterization of the quantum dots in chapter 2, this is likely a valid assumption. Three electron and two hole trap levels with characteristics listed in Table 6.1 were identified in the GaN layer. Under high injection conditions ($n = p >> n_i$), $A_{nr} \cong \sigma v_{th} N_T / 2$ where σ and N_T are the trap cross-section and density, respectively. A total value of $A_{nr} = 6.98 \times 10^7$ s^{-1} is calculated taking into account all the trap levels listed in Table 6.1. The value of n_{th} and C_a are then determined by solving Eqns. (6.4) – (6.6) iteratively and self-consistently for all the injection current. It should be noted that the recombination rate due to SHR recombination ($A_{nr}n$) is relatively small compared with spontaneous radiation recombination ($R_{sp}n^2$) and Auger recombination ($C_a n^3$) are the carrier concentrations typically found in a laser diode (10^{19}

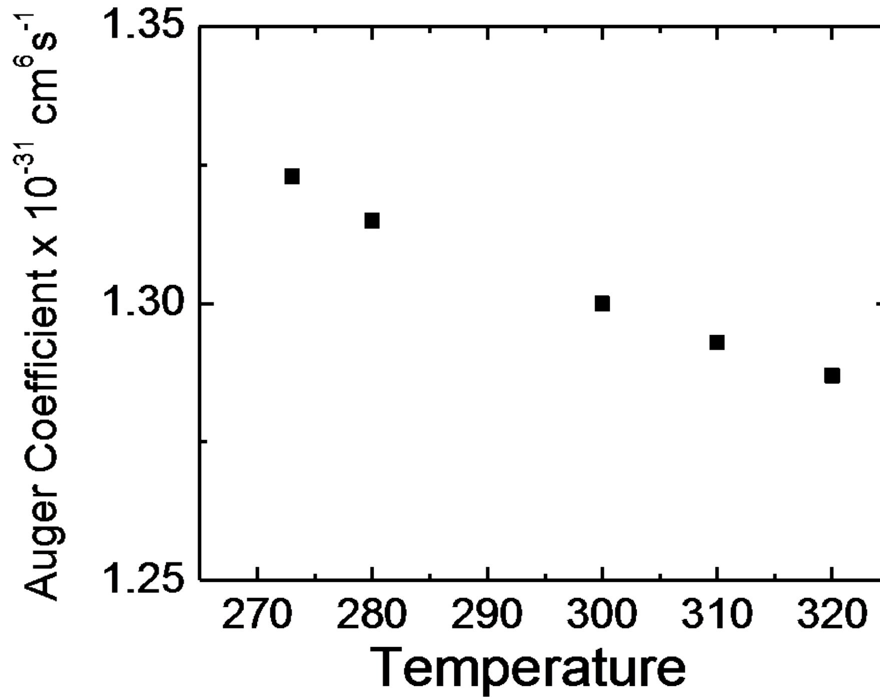

Fig. 6.9 Variation of the Auger coefficient with temperature from the measured time delays shown in Fig. 6.7.

cm^3) and the SHR recombination could often be neglected with minimal impact on the model accuracy. From the variation of time delay with temperature, the Auger coefficient is calculated for each temperature using the same value of R_{sp} and trap levels derived above. The values of C_a at different temperatures are plotted in Fig. 6.9. At room temperature C_a = 1.3x10^{-31} cm^{6}s^{-1} and n_{th}=1.3x10^{19} cm^{-3}.

6.6 Variation of Auger Recombination Coefficient with Temperature

In the temperature range in which the turn-on delay measurements have been made, it is found that τ_d increases with increase of temperature. Similarly, there is a small decrease in the value of C_a, shown in Fig. 6.9, with increase of temperature. Interestingly, the trends are identical to those observed for τ_d and C_a in InGaAs/GaAs quantum dots

[139]. The behavior can be explained by invoking electron-hole scattering in quantum dots [134-135], similar to what was necessary to explain the temperature dependence of carrier lifetime in Chapter 2. It is assumed that the low energy electron states in the quantum dots which participate in the Auger process are discrete and that occupation of these states depends on electron-hole scattering and occupation of the hole ground state. The higher energy states into which the third carrier is transferred in the Auger process is in a continuum. In the electron-hole scattering process, which is the dominant mechanism by which hot electrons relax in quantum dots, electrons in the higher energy states scatter with cold ground state holes and transfer their energy. The holes lose their excess energy and thermalize rapidly via closely spaced hole states by emission of phonons. With increase of temperature, the thermal excitation of holes from the ground state to higher energy states will decrease the rate of electron-hole scattering and therefore the population of the electron ground state. As a consequence, the turn-on delay time will increase and the Auger coefficient will decrease as observed.

Finally, since the Auger coefficient is proportional to $(k_BT/E_g)^{3/2}\exp(-E_g/k_BT)$, it is expected that the coefficient will increase with decrease of bandgap. The value of C_a measured here for λ = 630 nm (E_g =1.97 eV) is larger than that measured in $In_{0.25}Ga_{0.75}N/GaN$ green-emitting (λ ~ 500 nm) quantum dots-in-nanowire [44] and follows the expected trend of C_a versus bandgap reported by Piprek [140].

6.7 Comparison of Auger Coefficient with other Reported Values in the III-Nitride System

Auger recombination is a three carrier process in semiconductors in which the excess energy released from the recombination of an electron-hole pair is transferred by

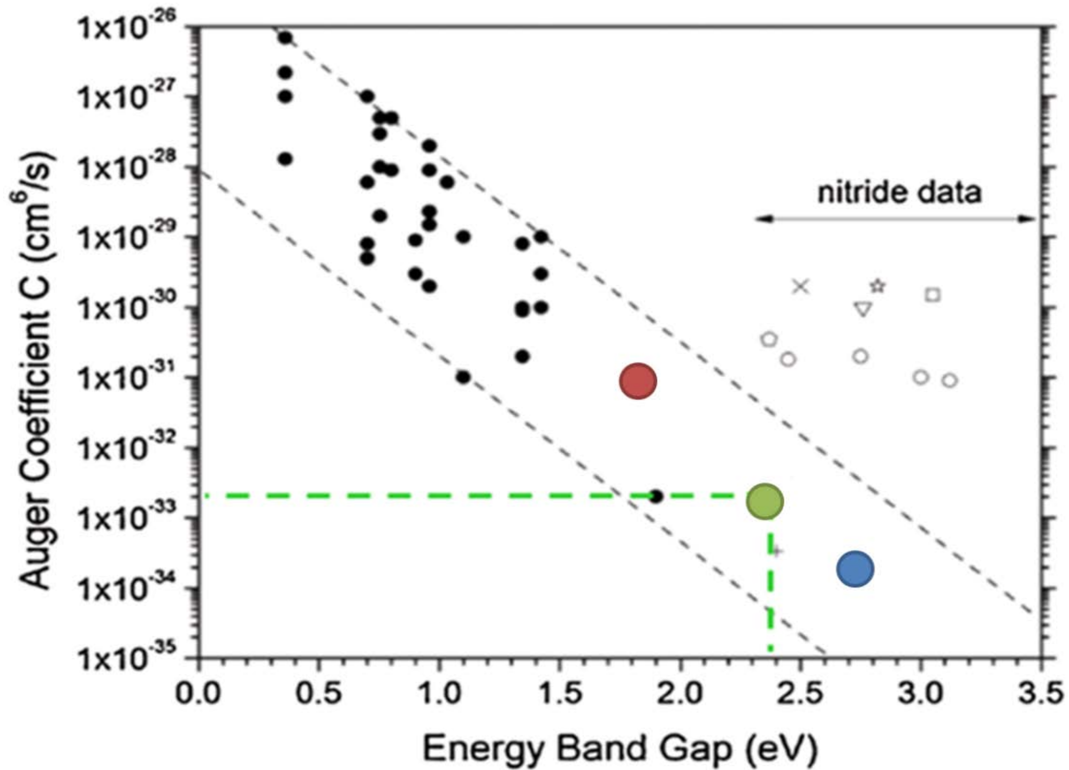

Fig. 6.10 Variation of Auger coefficient with bandap: expected (dashed grey lines) and measured (points). The red, blue, and green circles were measured in quantum dot or nanowire heterostructures where defects play a reduced role in recombination [adapted from 137, 140].

Columbic interactions to a third free carrier (either an electron or hole) deep into it's respective band. This carrier can then thermalize back to the ground state by multi-phonon emission. The probably of the Auger process, given by the Auger coefficient, C_a, decreases with bandgap, as mentioned in the previous section, proportionally to $(k_BT/E_g)^{3/2}\exp(-E_g/k_BT)$ [124]. It is therefore expected that the values of Auger recombination be small in wide bandgap materials, including the III-nitrides, shown by the dashed grey lines in Fig. 6.20. In GaN, an expected value of C_a~10^{-34} cm^6s^{-1}. As shown in Fig. 6.20, reported values for the nitrides typically lie above this range.

Calculation of Auger recombination coefficients is typically done under the

assumption of defect-free crystalline material. However, reported values of Auger coefficient are typically measured from samples grown on mismatched substrates (typically sapphire or silicon carbide) with defect densities of 10^7-10^8 cm^{-2}. It is likely then that a defect assisted Auger process is likely the cause of the higher reported values of C_s. Quantum dots, on the other hand restrict the movement of electrons and holes due to the physical 3-dimensional confinement present in the dots. Defects are then expected to play a smaller role in the Auger process. The measured value of C_a~10^{-31} cm^{6}s^{-1} in the red-emitting quantum dots is in the range of expected values for a material with a band gap of ~1.9 eV, as shown in Fig. 6.20 by the red circle.

In addition to large signal modulation of laser diodes, the Auger recombination coefficient can also be measured through small signal modulation of light emitting diodes (differential carrier lifetime measurements) [141, 142], and through the measurement of photoluminescence. It should be noted that Auger recombination has also been measured in blue- and green-emitting quantum dots and nanowires, which are also shown in Fig. 6.20. These materials with their relatively low defect densities have Auger coefficients in the expected range for their respective bandgap.

6.8 Summary

In summary, small-signal and large-signal modulation measurements on InGaN/GaN quantum dot ridge-waveguide lasers emitting at λ = 630 nm (red) have been shown. The maximum measured -3 dB modulation bandwidth is 2.4 GHz, demonstrating red-emitting quantum dot lasers as being useful in plastic fiber communications. Analysis of the small signal modulation response is also used to derive material and device characteristics. A differential gain of 5.3 x 10^{-17} cm^2 and a gain compression factor of 2.87

x 10^{-17} cm^3 are derived from the modulation data. The turn-on delay between the large signal electrical pulse and the coherent output optical pulse was measured for different injection current levels and at different temperatures. The value of the Auger coefficient C_a = $1.3x10^{-31}$ cm^6s^{-1} is measured at 300K and the coefficient exhibits an increasing trend with decrease of temperature. This behavior can be explained by invoking electron-hole scattering in the dot.

Chapter VII

Summary and Suggestions for Future Work

7.1 Summary of Present Work

The work presented in this dissertation focused on the development of red-emitting InGaN/GaN quantum dot lasers. Self assembled quantum dots grown by plasma assisted molecular beam epitaxy are described and optimized to improve the laser characteristics including reducing the threshold current density, increasing the output efficiency, and increasing the output power. Additionally, optical and structural characterization of the InGaN/GaN quantum dots are presented.

Optical and structural characterization of red-emitting InGaN/GaN quantum dots have been presented in chapter 1. It was found that the dot density and height increases from the first to third layer. Beyond the third layer, the density and height saturates at a density of ~$5x10^{10}$ cm^{-2}. The increase in dot density is attributed to indium segregation and higher indium composition in the second and third layers compared with the first layer. The dots are found to follow a scaling distribution, confirming the kinetically limited growth of the dots by molecular beam epitaxy. The quantum dots are characterized optically by photoluminescence which reveals a maximum efficiency of 35.9% in the 630 nm emitting dots. Time resolved photoluminescence has also been performed and a radiative lifetime of 2.2 ns is found in the red-emitting InGaN/GaN

quantum dots. This agrees well with theory. A carrier relaxation bottleneck is also found through time resolved photoluminescence and is attributed to the lack of phonons with available energies for electron relaxation at elevated temperatures.

At longer wavelengths, the refractive index difference between GaN and traditionally used $Al_xGa_{1-x}N$ cladding is reduced. This leads to reduced modal confinement and increased substrate leakage and overlap with the cladding leading to increased free carrier absorption. The larger cavity loss and reduced modal gain in combination with the lack of efficient emitters at wavelengths beyond 530 nm have contributed to the lack of III-nitride devices emitting in the red. The incorporation of high efficiency InGaN/GaN quantum dots with the new heterostructure have allowed for the demonstration of the first red-emitting nitride-based lasers. The lasers are characterized by relatively low threshold current density (J_{th}~2.5 kA/cm^2) and only weak temperature dependence of the threshold current density (T_0~240 K). These values are very favorable compared with traditional InGaAlP/GaAs based heterostructures emitting in the red (J_{th}=6-8 kA/cm^2, T_0=60~80 K). Additionally, length dependent characterization is presented from which a high value of differential gain is derived. From the shift in output emission wavelength with injection a relatively small value of polarization field (200 kV/cm^2) is measured.

Optimization of the laser heterostructure is described in chapter IV. P-doping is relatively inefficient in GaN based heterostructures due to the large effective heavy hole mass and large n-type background doping. Improved diode characteristics are obtained through the use of metal modulated epitaxy and the growth of p-GaN by this growth technique is optimized. $In_{0.18}Al_{0.82}N$ diodes are also grown and demonstrated with good

diode characteristics, considering the further increased bandgap and reduced doping efficiency. This is likely due to the increased Mg incorporation at the relatively low growth temperatures which also facilitates the growth of high quality quantum dots. The growth of InGaN/GaN quantum dots are optimized by by investigating the effects of the InGaN and GaN growth times along with the nitrogen interruption time. A maximum efficiency of 51% is reported with the optimizations in the growth parameters, compared with 35.9% in the previous InGaN/GaN red-emitting quantum dots.

The optimized laser heterostructure has been grown and the characteristics of these lasers are presented in chapter V. The lasers are characterized by a reduced cavity loss (~9 cm^{-1}) compared with ~25 cm^{-1} in the previous laser heterostructure. The reduced cavity loss and increased quantum dot efficiency resulted in reduced threshold current density (1.6 kA/cm^2), higher output power (30 mW), and higher wall plug efficiency (1.5%). The lasers have also been characterized by larger differential gain ($9x10^{-17}$ cm^2), and slightly higher temperature stability (T_0=240 K).

Finally, dynamic characterization of the red-emitting InGaN/GaN quantum dot lasers is presented in chapter VI including small and large signal modulation of the devices. A maximum f_{-3dB} bandwidth of 2.4 GHz has been measured. The small signal modulation is also used to derive a differential gain of $5x10^{-17}$ cm^2, comparable with the value reported from length dependent light-current characterization. Large signal analysis is used to derive the Auger coefficient, $C_a=10^{-31}$ cm^6s^{-1}. This value is in agreement with theoretically predicted values at this emission energy (1.9 eV), unlike reported values in InGaN/GaN quantum wells. This favorable value along with the deep potential wells in the InGaN/GaN dot are the likely cause the high temperature stability in these lasers and

Fig. 7.1 Heads-up display where visible lasers are used to project the drivers speed and directions on the windshield [143].

the cause of the reduced droop in previously reported InGaN/GaN quantum dot based light emitting diodes.

7.2 Suggestions for Future Work

7.2.1 Heads-Up Displays Incorporating Red-Emitting InGaN/GaN Quantum Dot Lasers

The laser heterostructure and quantum dot optimizations were designed with the desired characteristics for projector and heads-up display applications, shown in Fig. 7.1. This requires relatively high power lasers which can operate at elevated temperatures (up to 95°C). The lasers have been characterized up to this temperature. While promising characteristics have been obtained, higher output powers, particularly at higher temperatures are desirable. All measurements have been made on unpackaged, bare devices. As discussed in chapter 4, device self-heating plays a large role in the restriction of the output power and efficiency. The laser active region is reaching temperatures in excess of 100°C higher than the ambient temperature. Device packaging or active cooling may lead to more favorable characteristics and should be explored for future applications incorporating these InGaN/GaN quantum dot lasers. As discussed in chapters 2 and 6, a

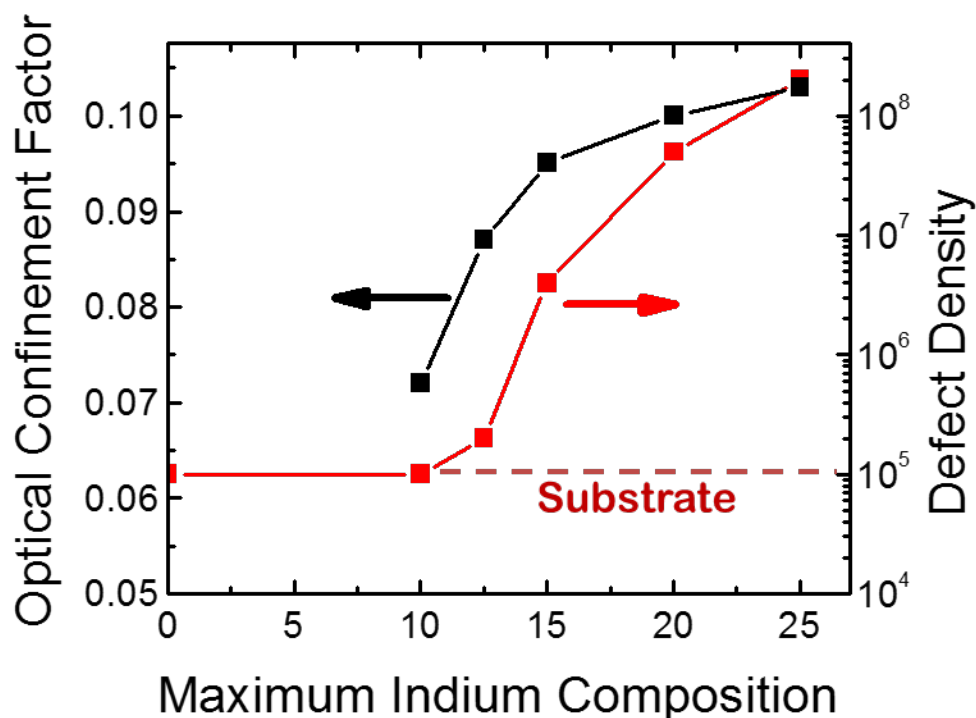

Fig. 7.2 Calculated optical confinement factor of the laser heterostructure as a function of maimum composition in the graded $In_{0\text{->}x}Ga_{1\text{->}x}N$ cladding. The defect densites were measured in samples grown up to the active region.

relaxation bottleneck is evident and the dominant scattering mechanism for the electrons into the ground state is electron-hole scattering, a process that becomes less efficient at higher temperatures. Packaging and device management are important in these quantum dot devices and should be carefully considered in practical applications.

7.2.2 Graded Index Separate Confinement Heterostructures

Visible laser heterostructures are typically grown with a step index waveguide consisting of a variety of layers with abrupt interfaces, similar to the heterostructures adopted in this thesis. Alternatively, GaAs based lasers often adopt a continuously or quasi-continuously varying index profile with graded cladding layers. For example, after growth of the GaAs contact layer and $Al_{0.3}Ga_{0.7}As$ cladding, a graded layer, $Al_{0.3\text{->}0}Ga_{0.7\text{->}1}As$ may be used near the active region. This graded layer allows for

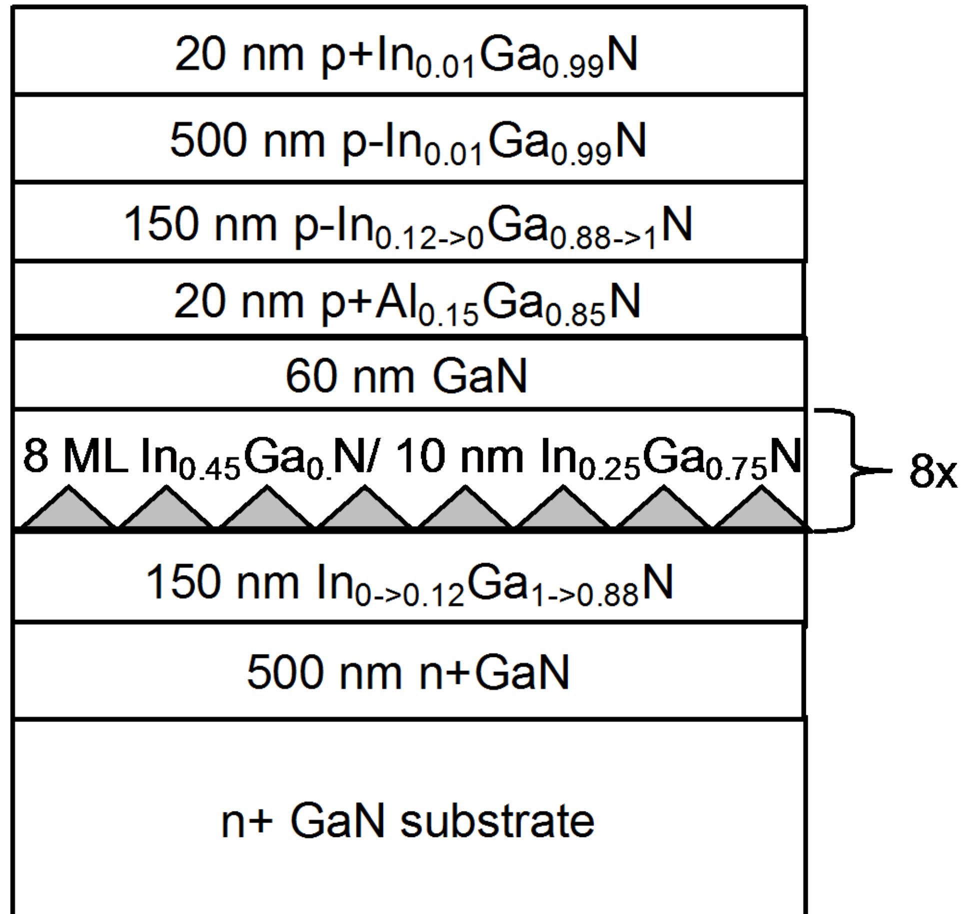

Fig. 7.3 Proposed graded separate confinement heterostructure.

superior optical confinement in such laser heterostructures. Unlike AlGaAs on GaAs which is nearly lattice matched at all compositions, AlGaN on GaN is tensile strained, restricting the compositions to $Al_{\sim 0.07}Ga_{\sim 0.93}N$, with relatively small index difference. An alternative is the use of InGaN, graded over a sufficient length to reduce the formation of dislocations The alternative cladding (graded InGaN) should have higher hole concentrations than the previously used $In_{0.18}Al_{0.82}N$ due to the smaller bandgap. Modal simulations have been performed to calculate the optical confinement factor as a function of final composition in the $In_{0\to x}Ga_{1\to 1-x}N$ cladding. A 150 nm graded layer is chosen to ensure a single transverse mode exists. Additionally, etch pit dislocation measurements

were performed on growths of this layer on GaN substrates (dislocation density ~10^5 cm^{-2}) The results of the simulation and dislocation measurements are shown in Fig. 7.2. A maximum composition of x=12% can be grown, while still providing adequate modal confinement. The proposed heterostructure with this composition is shown in Fig. 7.3.

APPENDICES

APPENDIX A

Substrate Preparation Prior to MBE Growth

Prior to introduction of samples into the MBE system, they must be thoroughly cleaned and degassed to prevent contamination in the growth chamber, particularly of organic compounds. First 500 nm of molybdenum is deposited on the back of the samples (whether GaN on sapphire or GaN substrates) for measurement of the sample temperature by an infrared pyrometer. The samples are then diced to the appropriate size (typically 400 mil x 400 mil). To remove contamination (organics from handling the samples, residual glue from the dicing tape), the samples are cleaned in trichloroethylene, acetone, and isopropanol for 5 minutes each followed by a rinse in deionized water. After the samples are loaded into Moly blocks, they are bakes for 1 hour in the intro chamber at 200°C, and for 2 hours at 400°C in the buffer chamber. The samples should be kept in the high vacuum growth chamber for 30 minutes prior to growth.

APPENDIX B

Quantum Dot Ridge Waveguide Laser Processing

1. Deposition of Alignment Mark

1.1 Solvent clean:

Acetone: 5 min on hot plate

IPA 5 min

DI water Rinse: 3 min

1.2 Lithography

Dehydrate bake: 1 min, 115 °C hotplate

Resist coating: SPR 220-3.0 @ 4.0 krpm, 30 sec

Pre-bake: 1 min @ 115 °C on hotplate

Exposure: 0.32 sec in projection stepper

Post-bake: 1 min @ 115 °C

Resist development (CEE): AZ 300 MIF or AZ 726 60 sec double puddle;

1.3 Descum:

60 sec, 60 W, 250mT

1.4 Metal Deposition

Ni/Au 50 Å /2000 Å

1.5 Metal Lift-off

2 hours in Acetone

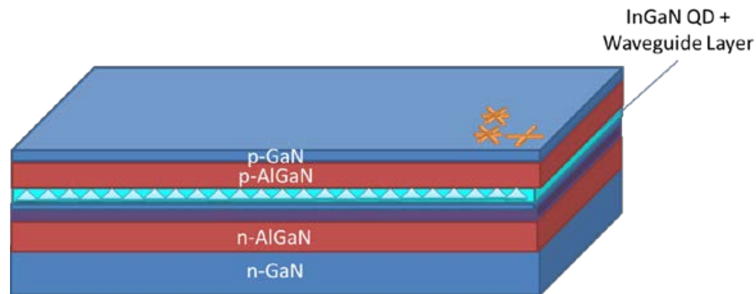

Fig. B1 Laser heterostructure post-growth.

2. Defining Ridge Geometry

2.1 Solvent clean:

Acetone: 5 min on hot plate

IPA 5 min

DI water Rinse: 2 min

2.2 Lithography

Dehydrate bake: 1 min, 115 °C hotplate

Resist coating: SPR 220-3.0 @ 4.0 krpm, 30 sec

Pre-bake: 1 min @ 115 °C on hotplate

Exposure: 0.32 sec in projection stepper

Post-bake: 1 min @ 115 °C

Resist development (CEE): AZ 300 MIF or AZ 726 60 sec double puddle;

2.3 Plasma Etching

LAM:

ICP etching, etching recipe chlorine based. The etching rate is calibrated to be 4.5-5.5 ns.

2.4 Resist Removal

Plasma Asher: 300 sec, 200 W

Acetone: 10 min on hot plate

IPA: 5 min

DI water rinse: 2 min

2.5 Dektak: measure mesa height

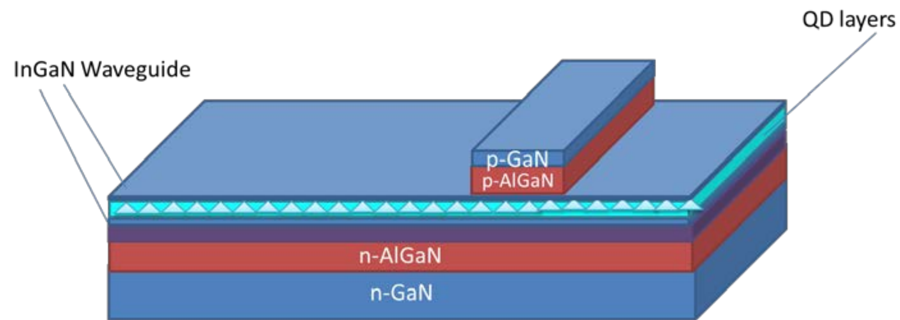

Fig. B2 Laser heterostructure after ridge etch.

3. Etching till n-GaN

3.1 Solvent clean:

Acetone: 10 min on hot plate

IPA 10 min

DI water Rinse: 2 min

3.2 Lithography

Dehydrate bake: 1 min, 115 °C hotplate

Resist coating: SPR 220-3.0 @ 4.0 krpm, 30 sec

Pre-bake: 1 min @ 115 °C on hotplate

Exposure: 0.32 sec in projection stepper

Post-bake: 1 min @ 115 °C

Resist development (CEE)t: AZ 300 MIF or AZ 726 60 sec double puddle;

3.3 Plasma Etching

LAM:

ICP etching, etching recipe chlorine based. The etching rate is calibrated to be 4.5-5.5 ns.

3.4 Resist Removal

Plasma Asher: 300 sec, 200 W

Acetone: 10 min on hot plate

IPA: 5 min

DI water rinse: 2 min

3.5 Dektak: measure mesa height

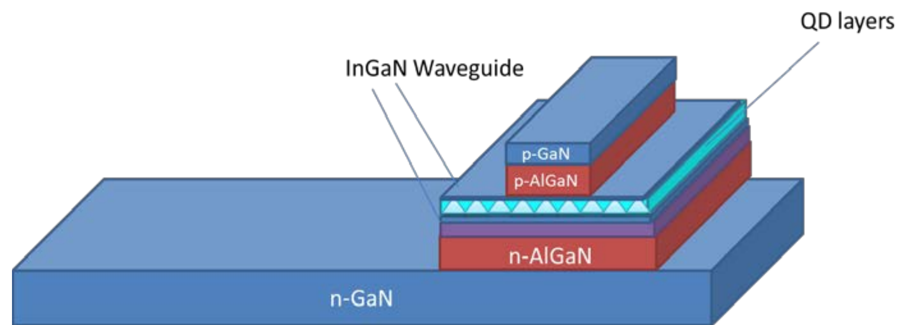

Fig. B3 Laser heterostructure after mesa etch.

4. Deposition of n-contact

4.1 Lithography

Dehydrate bake: 1 min, 115 °C hotplate

Resist coating: SPR 220-3.0 @ 4.0 krpm, 30 sec

Pre-bake: 1 min @ 115 °C on hotplate

Exposure: 0.32 sec in projection stepper

Post-bake: 1 min @ 115 °C

Resist development (CEE)t: AZ 300 MIF or AZ 726 60 sec double puddle;

4.2 Descum:

60 sec, 60 W, 250mT

4.3 Oxide removal

HCl : DI water = 1:1, 1 min to remove native oxide

DI water rinse: 3 min

4.4 Metal deposition

Ti/Au = 10nm/200nm

4.5 Lift-off

Overnight in Acetone

IPA: 10 min

DI water: 2 min

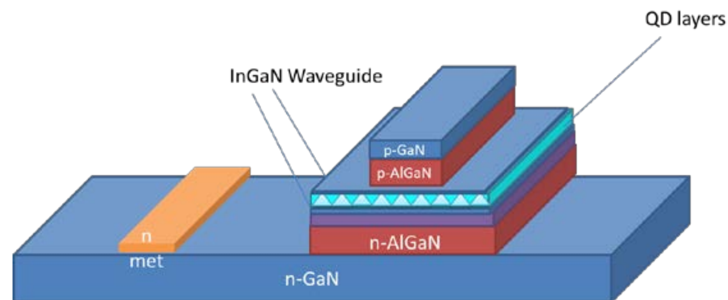

Fig. B4 Laser heterostructure after deposition of n-metal.

5. Passivation

SiO_x deposion: 800 nm using GSI PECVD

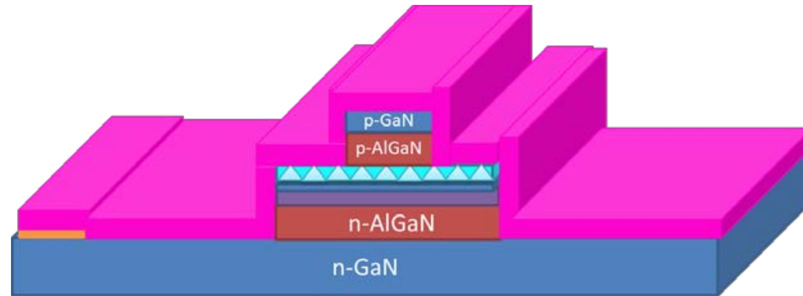

Fig. B5 Laser heterostructure after oxide deposition.

6. Oxide Etch (Formation of Via holes)

6.1 Lithography

Dehydrate bake: 1 min, 115 °C hotplate

Resist coating: SPR 220-3.0 @ 4.0 krpm, 30 sec

Note: HMDS may be necessary if the oxide was deposited at 380ºC

Pre-bake: 1 min @ 115 °C on hotplate

Exposure: 0.32 sec in projection stepper

Post-bake: 1 min @ 115 °C

Resist development (CEE): AZ 300 MIF or AZ 726 60 sec double puddle;

6.2 Plasma Etch

LAM:

SF_6 : C_4F_8 : Ar = 8 : 50 : 50 sccm, 10 mT, 300 W (rate ~ 180 nm/min)

Note: PECVD Oxide etch seems to be ~5 nm/min faster than the LNF quoted LPCVD oxide etch rate

6.3 Resist Removal

Plasma Asiher: 300 sec, 250 W, O_2 ~17%

Acetone: 10 min on hot plate

IPA: 5 min

DI water rinse: 2 min

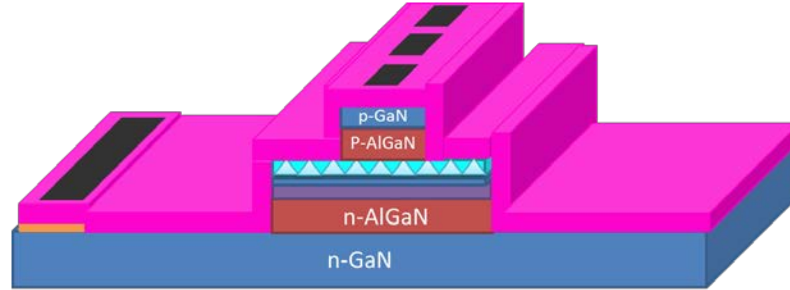

Fig. B6 Laser heterostructure after via hole etch.

7. **Deposition of p-contact and Interconnect**

7.1 Lithography

Dehydrate bake: 1 min, 115 °C hotplate

Resist coating: SPR 220-3.0 @ 4.0 krpm, 30 sec

Note: HMDS may be necessary if the oxide was deposited at 380ºC

Pre-bake: 1 min @ 115 °C on hotplate

Exposure: 0.32 sec in projection stepper

Post-bake: 1 min @ 115 °C

Resist development (CEE): AZ 300 MIF or AZ 726 60 sec double puddle;

7.2 Descum:

30 sec, 80 W, 250mT, 17% O2

7.3 Oxide removal

HCl : DI water = 1:1, 1 min to remove native oxide

DI water rinse: 3 min

7.4 Metal deposition

Ni/Au = 50Å/2000 Å

7.5 Lift-off

Overnight in Acetone

IPA: 10 min

DI water: 2 min

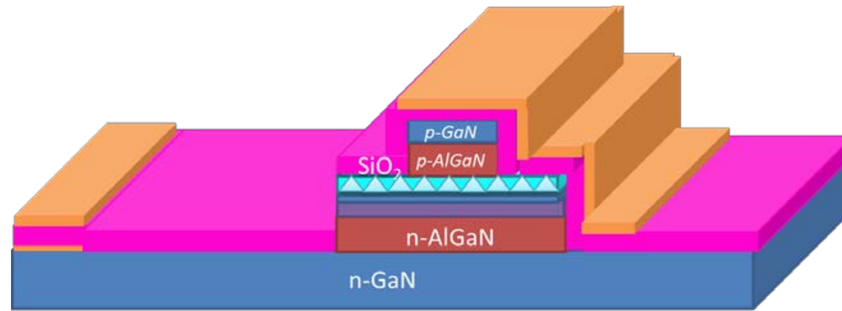

Fig. B7 Laser heterostructure after p-metal deposition.

8. Annealing

8.1 Rapid thermal annealing: 550 ºC, 5 min in N_2:O_2 (1:1) environment

9. Lapping

9.1 Mounting the sample on a glass plate with Paraffin wax (135 °C)

9.2 Lap down sample to ~ 100 µm

9.3 Solvent clean:

Xylenes > 30 min @ 105 °C hotplate

Acetone: 10 min

IPA : 10 min

DI water rinse: 2 min

10. Cleaving

10.1 Scribing: Make 2000 µm long, 400~1200 µm wide, 100 µm deep scribe

10.2 Press the sample gently with a small roller.

APPENDIX C

Measurement Setup Schematics

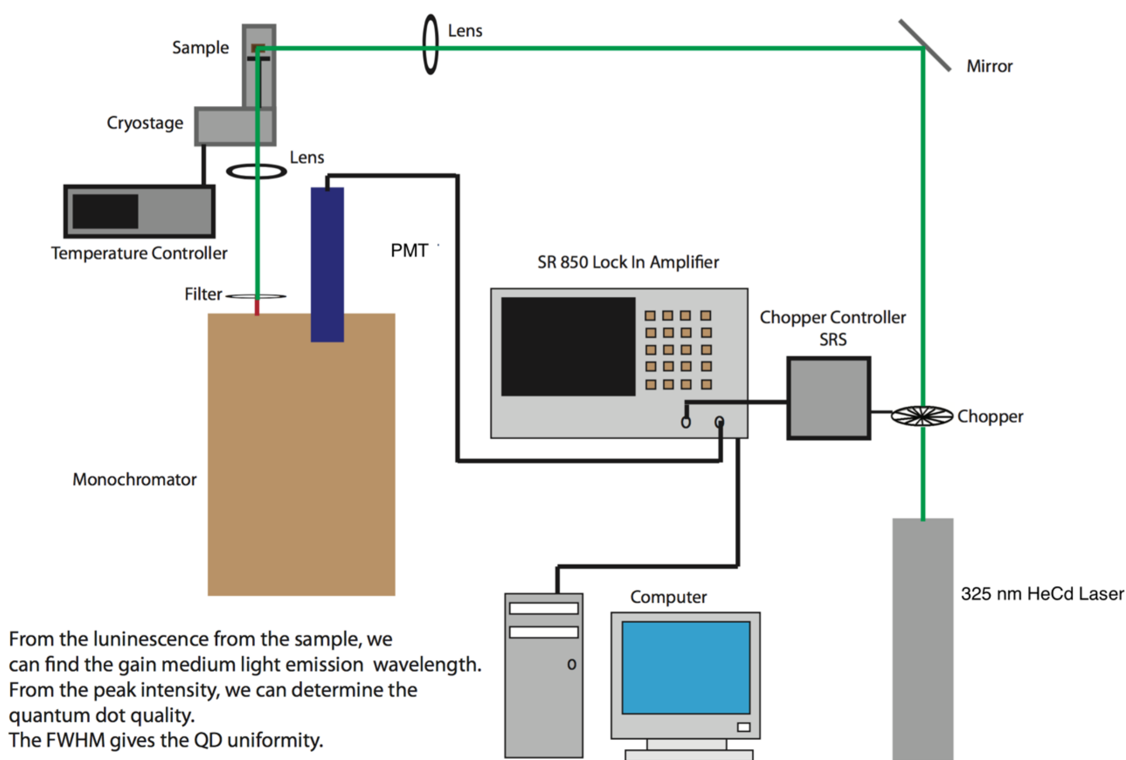

Fig. C.1 Shchematic of steady state photoluminescence setup for measuring ultra-violet and visible photoluminescence. The PMT can be replaced with a Ge detector for measuring near infrared extending the measurement range from 325 nm to 1700 nm.

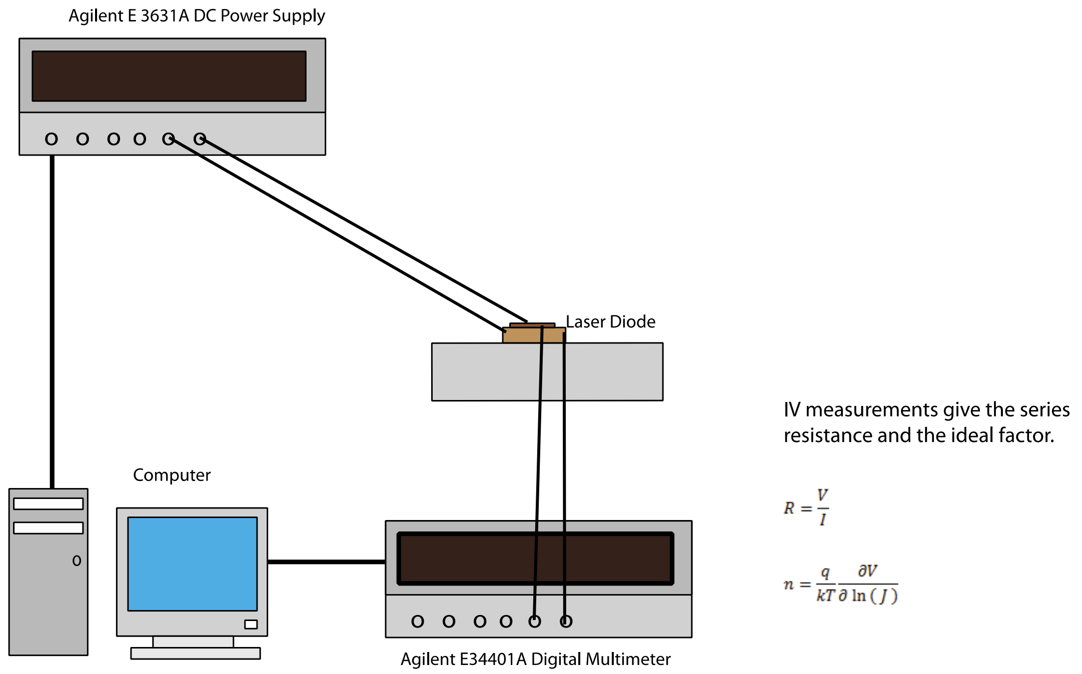

Fig. C.2 Schematic of voltage-current characterization setup.

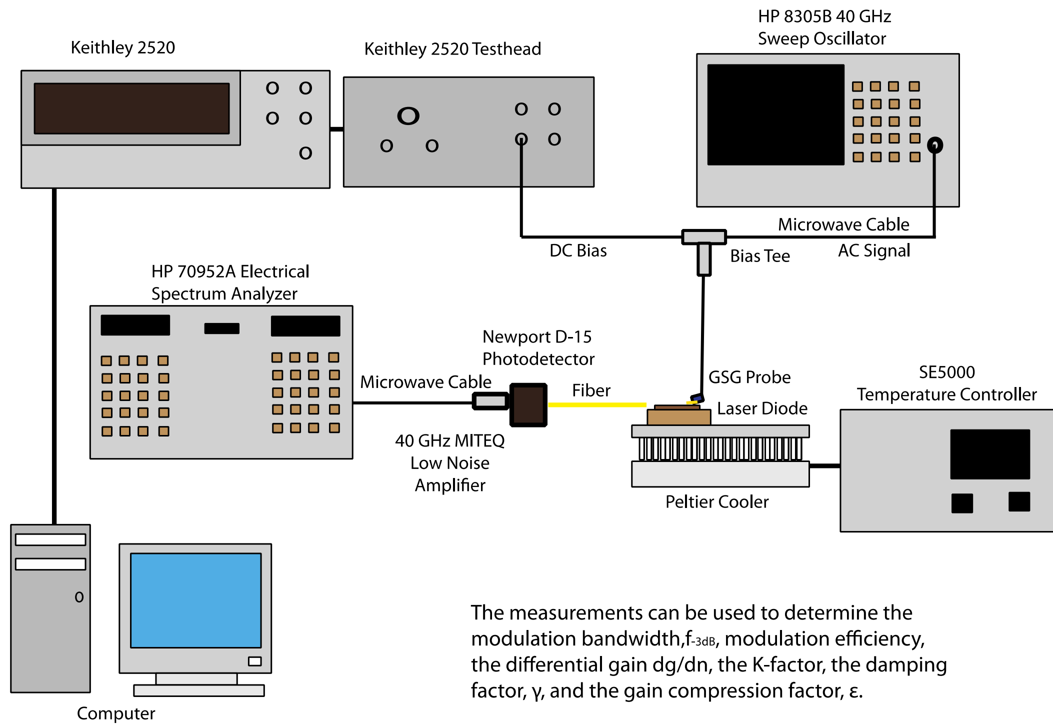

Fig. C.3 Schmetaic of the small signal modulation characteriation setup. This is used for measuring the modulation bandwidth, differential gain, and gain compression. This setup can also be used for measuring differentail carrier lifetime in light emitting diodes.

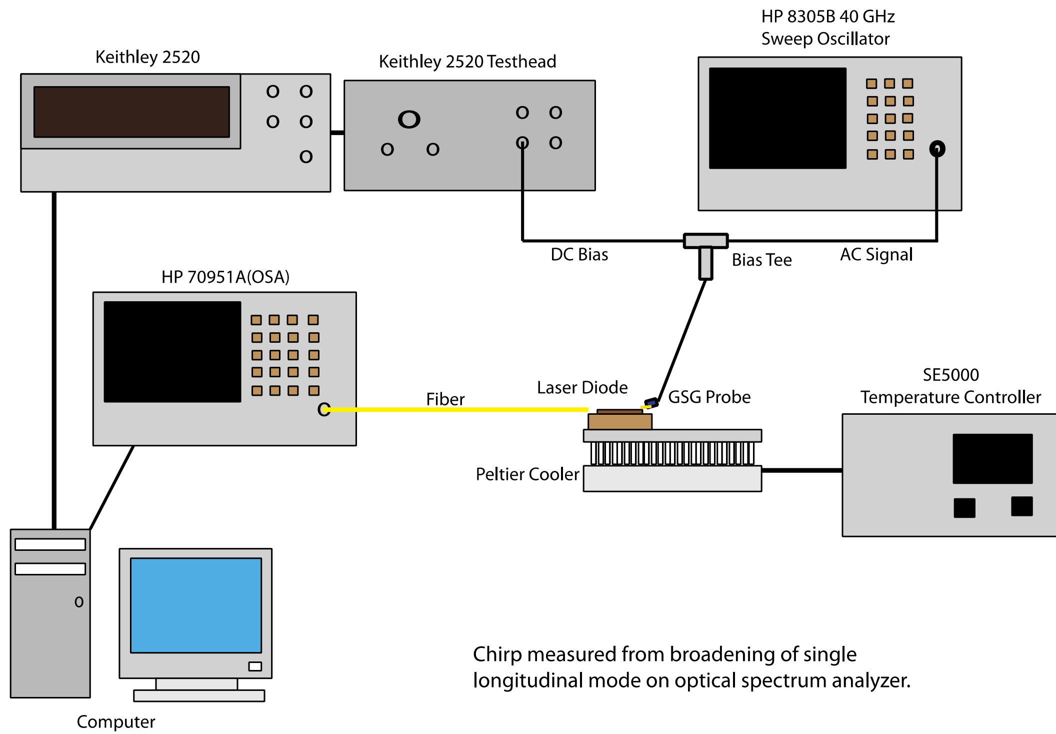

Fig. C.4 Measurement setup for measuring chirp and linewdith enhancement with small signal biasing.

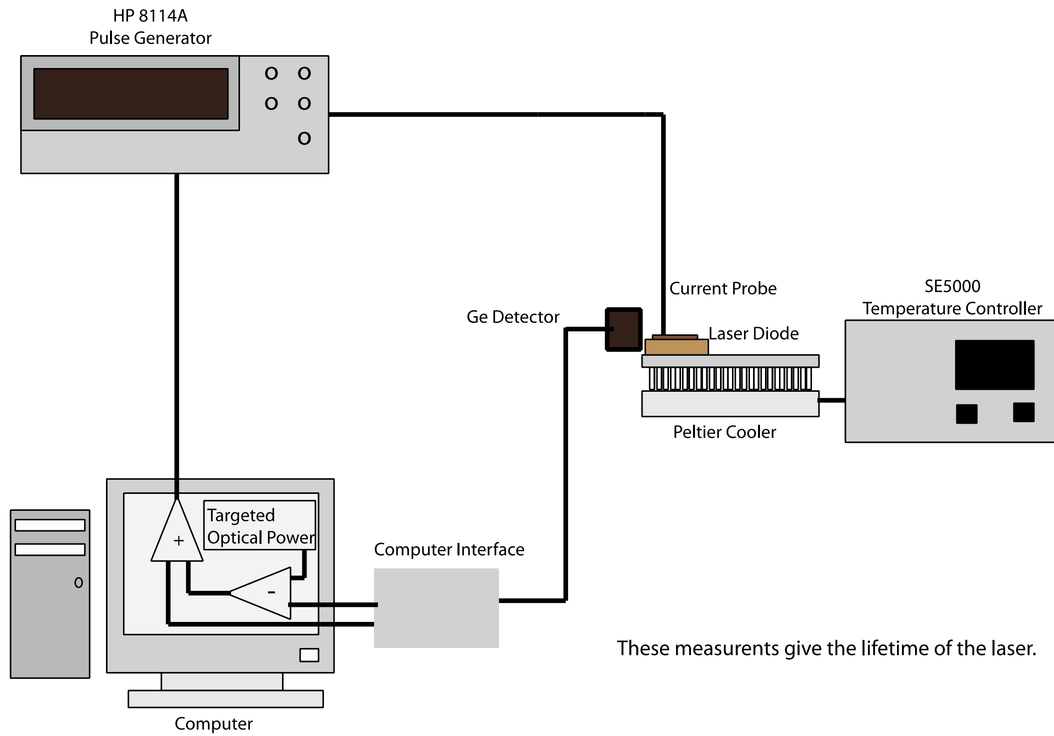

Fig. C.5 Measurement setup for testing laser diode reliability over long periods of time.

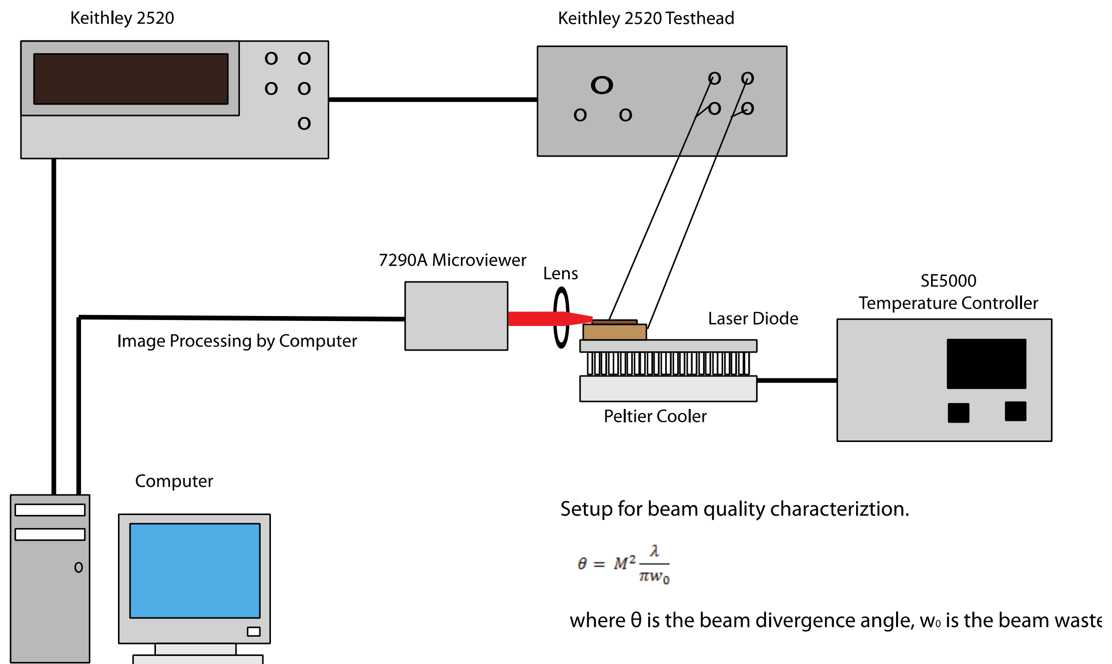

Fig. C.6 Measurement setup for analyzing far field and near field patterns of laser diodes. A standard charged coupled device (CCD) detector may be substituted for the 7290 Microviewer.

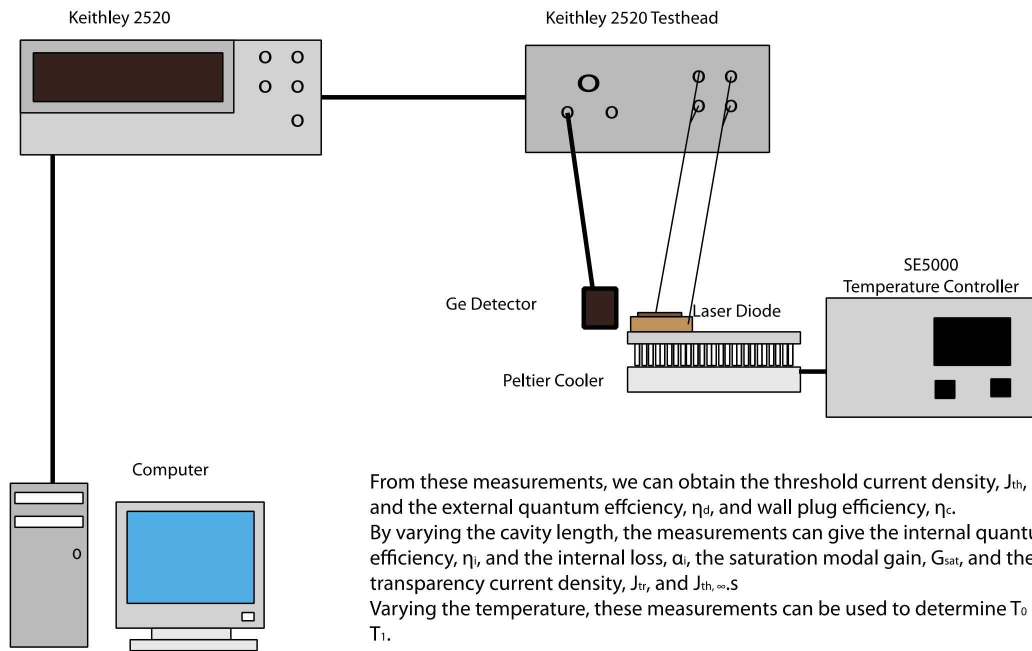

Fig. C.7 Measurement setup for characterizing light-current-voltage characteristics of the lasers.

Electroluminescence & linewidth enhancement Factor (α) Measurement System

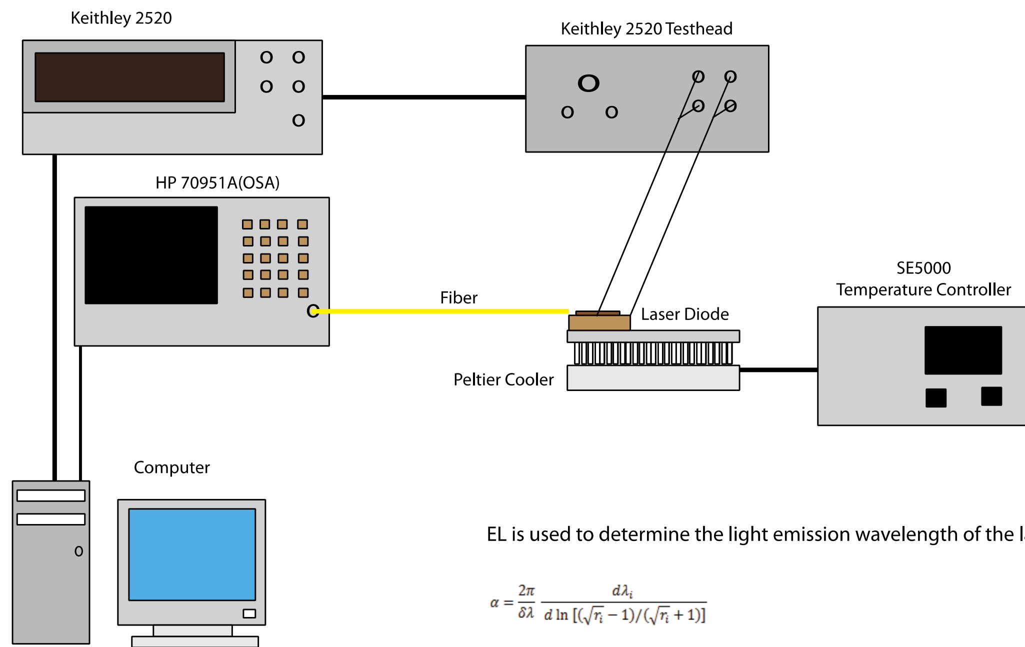

Fig. C.8 Setup for measuring spectral characteristics of the laser or light emitting diodes.

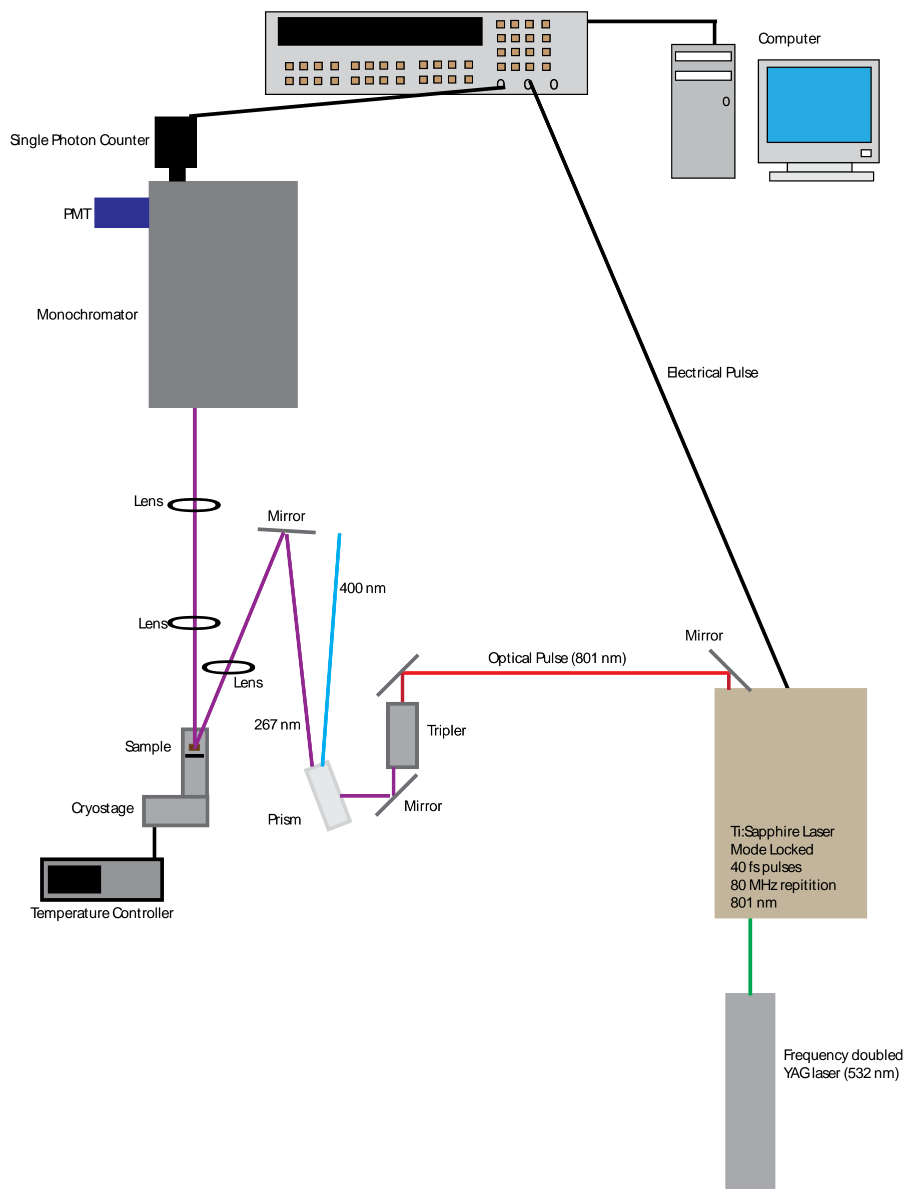

Fig. C.9 Setup for measuring photoluminescence and carrier lifetimes in materials with visible emission.

APPENDIX D

Transfer Matrix Method Simulations

Code D.1 Waveguide Mode Calculator

```
%Thomas Frost
%Example Laser Mode Calculator
%All thicknesses in microns

f=0.100; %Thickness of waveguide
c=0.005;%Thickness of QD

n1=2.3998; %AlGaN cladding
n2=2.42465; %GaN
n3=2.53; %InGaN Quantum Dot
n4=2.4432; %InGaN waveguide layer

n=[n1 n4 n2 n3 n2 n3 n2 n3 n2 n3 n2 n3 n2  n3 n2 n3 n2 n3  n2 n4 n1];
%Enter index for each layer in here including outer cladding
e=n.^2; %calculates permitivity assuming nonmagnetic
u= ones(1,length(n)) ; %can change permeability if applicable, otherwise
fill with the same number of 1's as the n vector
active=[0 0 0 1 0 1 0 1 0 1 0 1 0 1 0 1 0 1  0 0 0]; % mark active
layers with "1", others with "0"

confines=0;
i=0;
lengths=0;
for d=0.020:0.002:0.02;
    i=i+1;
    lengths(i)=d;
h=[f d c d c d c d c d c d c d c d c d f]; %height of every layer except
outer layers (assumed infinite)
w=0.630; %wavelength in um


figure(1); %to plot the b11 as a function of kz

minz=waveguide(e, u, h, w); %calculates kz which confine mode

figure(2);
hold on;

for j=1:length(minz)
    confines(i)=Eplotter_Mod( sqrt(e.*u), h, minz(j), w, active);
end
hold off;
end
```

Code D.2 waveguide.m called from D.1

```
function [ minz ] = waveguide( e, u, h, w )
%solves for the values of kz which solve a given waveguide geometry
%e-----relative permitvity of each layer
%u-----relative permeability of each layer

n=sqrt(e.*u); %calculates the index of each layer
a=200000; %sets up number of divisions to create

kzmin=2*pi*min(n)./(w*1e-6); %min value of kz that needs to be checked
kzmax=2*pi*max(n)./(w*1e-6); %max value of kz that needs to be checked
kzinc=(kzmax-kzmin)/a; %checks a points

k0z=zeros(1, a+1); %sets up matrix of kz points to check
b11=zeros(1,length(k0z)); %sets up empty array of b11
lkz=length(k0z)-1; %length of the kz vector minus 1
for i=1:lkz
    k0z(i)=kzmin+(i-1)*kzinc;
    b11(i)=tmm(e, u, h, k0z(i), w);
end
figure (1);
semilogy(real(k0z),abs(b11)); %plots b11 as a function of k0z
xlim([kzmin kzmax]);


%======Calculates all times where b11 is approximately
zero===============
j=0; %starts with no points
minz=k0z(1);
for i = 2:lkz

    if (abs(b11(i-1))>abs(b11(i)) & abs(b11(i+1))>abs(b11(i)) &
b11(i)<0.01)
        minz(j+1)=k0z(i);
        j=j+1;
    end
end



end
```

Code D.3 tmm.m called from D.2

```
function [ b11 ] = tmm( e, u, h, k0z, w)
%TMM Transfer Matrix Method implementation method for an arbitrary
%number of layers at angle a, and wavelength w

%takes in e-relative permitivity in each layer
%         u-relative permeability in each layer
%         h-thickness of each layer (besides, first & last->assumed
infinite
%         a- angle of incidence
%         w- wavelength- in micrometers
%for TM propagation, switch e and u


%===============checks for how many layers there are,
etc===================
layers=length(e); %number of layers
middle=length(h); %number of sandwiched layers
waves=length(w); %number of wavelengths

%==============calculates constants in each
layer==========================
n=sqrt(e.*u); %defined refractive index of all layers

k0=2*pi.*n(1)./(w*1e-6); %defines wavevector in first layer

c=3e8*1e6; %speed of light in um/s
f=c./w; %frequency in hz
ww=2*pi*f; %angular frequency

kx=sqrt(ww.^2.*n.^2./3e8.^2-k0z.^2); %caculates kx in each layer


%========================sets up starting matrix (identity
matrix)========
AB=eye(2); %returns 2x2 identiy matrix
AB0=AB;

%======calculates propagation through all layers except last
interface=====
if (length(e)~=2) %if there are more than 2 layers
    for i=1:length(e)-2 %for all but the last interface
        P=u(i)*kx(i+1)./u(i+1)./kx(i);
        T12=1/2*[1+P 1-P; 1-P 1+P];
        P2=[exp(-1i.*kx(i+1)*h(i)*1e-6) 0; 0 exp(1i*kx(i+1)*h(i)*1e-6)];
        M=T12*P2;
        AB=AB0*M;
        AB0=AB;

    end
end

%======caculates reflections at the final
interface========================
P=u(layers-1).*kx(layers)./u(layers)./kx(layers-1);
T12=1/2*[1+P 1-P; 1-P 1+P];

AB=AB0*T12;
```

```
%=========================returns the value of
b11=========================
b11=AB(1,1);


end
```

Code D.4 Eplotter_Mod.m called from D.1

```
function [ a ] = Eplotter_Mod( n1, h, min,w, activ )
%Plots electric field profile,
%n1----list of indiciesfor each layer
%h-----list of sandwhiched layer thicknesses
%min---a value of kz solving the waveguide conditions
%w-----wavelength in microns


%===================Constant Calcultions================================

Divisions=20000; %how thick to make each layer when dividing structure
%equal to 1um/Divisions, for example if Divisions=1000=> matlab will
divide
%divisions into 1 nm thick slices.
Cladding=1; %thickness to plot cladding in microns
c=3e8*1e6; %speed of light in um/s
f=c./w; %frequency in hz
ww=2*pi*f; %angular frequency
k0=ww/3e8; %wavevector in free space
neff=abs(min)./k0 %neff given the value of kz and k0
d1= [Divisions*Cladding h*Divisions Divisions*Cladding]; %adds cladding
to list of thickness


%====================Divides struction into many thin layers============
m=0;
for i=1:size(d1,2)
    for j=1:d1(i)
        n(m+1)=n1(i);
        d(m+1)=1e-6/Divisions;
        active(m+1)=activ(i);
        m=m+1;
    end
end

%=================Sets up Boundary Conditions==========================
l=size(d,2);%number of layers (total thickness in nm)
z=1:l;%array of numbers from 1 to l
A=zeros(1,l); %coefficient in positve propagating wavefunction, sets all
to zero
B=A; %coefficient in negatvie propagating wavefunction
phi=A; %wavefunction
phi_d=A; %derivative of the wavefunction
A(1)=1; %sets intial positive to 1
B(1)=0; %sets initial negative to 0
phi(1)=1; %sets E=1 in the first layer

k=k0*sqrt((neff^2-n.^2)); %sets up the wavevector in each layer
phi_d(1)=k(1); %sets up the derivative of phi in each layer


%================Calculates the electric field in each
layer==============
for i=2:l; %start with layer 2, 1st layer is arbitrary set to 1
        A(i)=(phi(i-1)+phi_d(i-1)/k(i))/2; %calculates A from previous
phi
        B(i)=(phi(i-1)-phi_d(i-1)/k(i))/2; %calculates B from previous
phi
        phi(i)=A(i)*exp(k(i)*d(i))+B(i)*exp(-k(i)*d(i)); %calculates E
```

```
        phi_d(i)=A(i)*k(i)*exp(k(i)*d(i))-B(i)*k(i)*exp(-k(i)*d(i));
end


plot((z/Divisions*1000),phi/max(phi)); %plots the electric field mode
profile

%E==energy in the formula below, phi==electric field, sorry for the
%confusing notaion

%Power is equal to electric field squared dived by two times the
impedance
%of that layer------P=E^2./2(eta)
%Since the permeability is equal to 1, eta is proportional to 1/n where
n
%is the index so P is porportional to n*E^2

    QW=0; %energy confined to active region, starts sum at zero for 1st
layer
    for i=2:l
        E(i)=n(i)*phi(i).^2;
        if active(i-1) %if active region, count for confinement factor
            QW=QW+E(i); %add to previous result
        end
    end
    Total=sum(E);
    confinment=QW/Total

a=confinment;
end
```

Code D.5 DBR Code for plotting Reflectivity Spectra

```
lambda=0.630; %wavelength in microns
n2=1.5; %index of material 1 (closest to air)
n1=2.42; %index of material 2 (closest to laser)


pairs=5; %total # of pairs to try


d1=lambda/4/n1;
d2=lambda/4/n2;

na= [n1 n2];
da= [d1 d2];


for j=1:pairs

n= 2.42; %neff, the effective index of the laser
h=[];

for i=1:j
    n=[n na];
    h=[h da];
end

n=[n 1];

e=n.^2;
u=ones(1,length(e));

figure(j)
wavelength(e,u,h,0);
axis([0.3 0.9 0 1]);
end

RwithNoDBRs=((n(1)-1)/(n(1)+1)).^2
```

Code D.6 wavelength.m code called from D.5

```
function [ output_args ] = wavelength( e, u, h, a )
%ANGLE Summary of this function goes here
%   plots reflectivity over all angles, given e, y, h, w


w=0.3:0.001:.9; %enter wavelength range (in microns) here in the format
                  %starting wavelength:increment:ending wavelength
r=zeros(length(w),1);
t=zeros(length(w),1);

for i=1:length(w)
    [r(i) t(i)]= tmm(e, u, h, a, w(i));
end

plot(w, abs(r).^2);

end
```

BIBLIOGRAPHY

[1] O. Nam, *et.al. Phys. Stat. Sol. (a),* **201** (12), 2717 (2004).

[2] H. Ohta, S. DenBaars, and S. Nakamura, *J. Opt. Soc. Am. B.* **27** (11), B45 (2010).

[3] S. Nakamura, M. Senoh, N. Iwasa, and S. Nagahama, *Jpn. J. Appl. Phys.* **34**, L797–L799 (1995).

[4] K. Okamoto, J. Kashiwagi, T. Tanaka, and M. Kubota, *Appl. Phys. Lett.* **94**, 071105, (2009).

[5] U. Strauß, *et. al. Proc. of SPIE* **6894**, 689417 (2008).

[6] Y. Narukawa, Y. Kawakami, M. Funato, S. Fujita, S. Fujita, and S. Nakamura, *Appl. Phys. Lett.* **70**, 981 (1997).

[7] D. Queren, *et. al. Appl. Phys. Lett.* **94**, 081119 (2009).

[8] C. Skierbiszewski, *et. al. Appl. Phys. Lett.* **86**, 011114 (2005).

[9] C. Skierbiszewski, *et. al. J. Vac. Sci. Technol. B* **30**, 02B102 (2012).

[10] C. Huang, *et. al. Appl. Phys. Lett.* **95**, 241115 (2011).

[11] D. Bour, C. Chua, Z. Yang, M. Teepe, and N. Johnson *Phys. Lett.* **94**, 041124 (2009).

[12] S. Nakamura , M. Senoh , S. Nagahama , N. Iwasa , T. Yamada , T. Matsushita , Y. Sugimoto and H. Kiyoku, *Appl. Phys. Lett.* **69**, 4056 (1996).

[13] Y. Enya, Y. Yoshizumi, T. Kyono, K. Akita, M. Ueno, M. Adachi, T. Sumitomo, S. Tokuyama, T. Ikegami, K. Katayama, and T. Nakamura, *Appl. Phys. Exp.*, **2**, 082101 (2009).

[14] D. Sizov, R. Bhat, Fellow, and C.-E. Zah, *J. Llightwave Tech.*, **30**(5), 679 (2012).

[15] J. Piprek, *Phys. Status Solidi A,* 1–9 (2010).

[16] H. Ashi, Y. Kawamura, H. Nagai, *J. Appl. Phys.* **54**, 6058 (1983).

[17] M. Ikeda, Y. Mori, H. Sato, K. Kaneko, and N. Watanabe, *Appl. Phys. Lett.* **47**, 1027 (1985).

[18] J. Rennie, Okajima, M. Watanabe, and G. Hatakoshi, *IEEE J. of Quantum. Electron.* **29** (6), 1857 (1993).

[19] A. Banerjee, T. Frost, E. Stark, and P. Bhattacharya, *Appl. Phys. Lett.* **101**, 041108 (2012).

[20] M. Zhang, M., A. Banerjee, C. Lee, J. Hinckley, and P. Bhattacharya, *Appl. Phys. Lett.,* **98**, 221104 (2011).

[21] [T. Frost, A. Banerjee, K. Sun, S. L. Chuang, and P. Bhattacharya, *IEEE J. Quantum Electron.* **49** (11), 923 (2013).

[22] T. Frost, A. Banerjee, and P. Bhattacharya, *Appl. Phys. Lett.* **103**, 211111 (2013).

[23] T. Frost, A. Banerjee, S. Jahangir, and P. Bhattacharya, *Appl. Phys. Lett.* **104** (8), 081121 (2014).

[24] S. Schulz, S., and E. O'Reilly, *Phys. Rev. B*, **82**, 033411 (2010).

[25] Y. Wu, Y. Lin, H. Huang, and J. Singh, *J. Appl. Phys*. **105**, 013117 (2009).

[26] Y. Xie, http://www.seas.ucla.edu/smrl/GaN.html (2015).

[27] J. M. Phillips, M. E. Coltrin, M. H. Crawford, A. J. Fischer, M. R. Krames, R. Mueller-Mach, G. O. Mueller, Y. Ohno, L. E. S. Rohwer, J. A. Simmons, and J. Y. Tsao, *Laser & Photon. Rev.* **1**, 307 (2007).

[28] US Department of Energy, "Life-Cycle Assessment of Energy and Environmental Impacts of LED Lighting Products," February (2012).

[29] S. Nakamura, M. Senoh, and T. Mukai, *Jpn. J. Appl. Phys.*, **32**, L8 (1993).

[30] S. Nakamura, T. Mukai, M. Senoh, and N. Iwasa, *Jpn. J. Appl. Phys.*, **31**, L139 (1992).

[31] S. D. Burnham, G. Namkoong, D. C. Look, B. Clafin, and W. A. Doolittle, *J. Appl. Phys.* **104**, 024902 (2008).

[32] M. Zhang, P. Bhattacharya, W. Guo, and A. Banerjee, *Appl. Phys. Lett.* **96**, 132103 (2010).

[33] Y. C. Shen, G. O. Mueller, S. Watanabe, N. F. Gardner, A. Munkholm, and M. R. Krames, *Appl. Phys. Lett.*, **91**, 141101 (2007).

[34] M.-H. Kim, M. F. Schubert, Q. Dai, J. K. Kim, E. F. Schubert, J. Piprek, and Y. Park, *Appl. Phys. Lett.*, **91**, 183507 (2007).

[35] Y. Yang, X. A. Cao, and C. Yan, *IEEE Trans. on Elec. Dev.*, **55**, 1771 (2008).

[36] S. F. Chichibu, T. Sota, K. Wada, and S. Nakamura, *J. Vac. Sci. Technol. B* **16**, 2204 (1998).

[37] A. David, M. J. Grundmann, J. F. Kaeding, N. F. Gardner, T. G. Mihopoulos, and M. K. Krames, *Appl. Phys. Lett.,* **92***,* 053502 (2008).

[38] A. D. Dräger, H. Jőnen, C. Netzel, U. Rossow, and A. Hangleiter, *8th Intern. Conf. Nitride Semicon.,* Jeju (2009).

[39] M. Zhang, P. Bhattacharya, J. Singh, and J. Hinckley, *Appl. Phys. Lett.* **95**, 201108 (2009).

[40] A. E. Yunovich, V. E. Kudryashov, A. N. Turkin, A. Kovalev, and F. Manyakhin, *MRS Int. J. Nitride Semicond. Res.* **3**, 44 (1998).

[41] I. V. Rozhansky and D. A. Zakheim, *Phys. Status Solidi A* **204**, 227 (2007).

[42] A. Laubsch, M. Sabathil, W. Bergbauer, M. Strassburg, H. Lugauer, M. Peter, S. Lutgen, N. Linder, K. Streubel, J. Hader, J. V. Moloney, B. Pasenow, and S. W. Koch, *Phys. Status Solidi C* **6**, S913 (2009).

[43] A. Banerjee, Thesis, *III-Nitride Quantum Dot Light Emitting Diodes and Lasers* (2013).

[44] W. Guo, M. Zhang, P. Bhattacharya, and J. Heo, *Nano Lett.* **11** (4), 1434 (2011).

[45] H. Jameson, http://www.satellite-evolution.com/group/site/?p=10909 (2015).

[46] J. Piprek, *Phys. Status Solidi A,* 1–9 (2010).

[47] S. Nakamura, T. Mukai, and M. Senoh, *Appl. Phys. Lett.*, **64**, 1687 (1994).

[48] J. Piprek and S. Li, *Optical and Quantum Electronics* **42**(2), 89 (2010).

[49] N. F. Gardner, G. O. Muller, Y. C. Shen, G. Chen, S. Watanabe, W. Gotz, and M. R. Krames, *Appl. Phys. Lett.* **91**, 243506 (2007).

[50] J. H. Son and J.-L. Lee, *Opt. Express* **18**, 5466 (2010).

[51] S. Jahangir, M. Mandl, M. Strassburg, and P. Bhattacharya, *Appl. Phys. Lett.* **102**, 071101 (2013).

[52] S. Jahagir, T. Frost, A. Hazari, L. Yan, E. Stark, T. LaMountain, J. M. Millunchick, B. S. Ooi, and P. Bhattacharya, *Appl. Phys. Lett.* **106**, 071108 (2015).

[53] S. Fathpour, Z. Mi, and P. Bhattacharya, *J. Phys. D Appl. Phys.* **38**, 2103 (2005).

[54] P. G. Eliseev, H. Li, T. Liu, T. C. Newell, L. F. Lester, and K. J. Malloy, *IEEE J.Selected Topics in Quantum Electron.* **7**, 135 (2001).

[55] D. Bimberg, and U. W. Pohl, *Materials Today* **14** (9), 388 (2011).

[56] S. Nakamura, *Introduction to nitride semiconductor blue lasers and light emitting diodes*. Taylor & Francis, (2000).

[57] A. Usui, H. Sunakawa, A. Sakai, and A. Yamaguchi, *Japan. J. Appl. Phys.* **36** (7B), 899 (1997).

[58] H. Ibach and H. Lueth., *Solid-State Physics.* Springer Verlag, (2003).

[59] N. Newman, J. Cryst. Growth **178**, 102 (1997).

[60] J. G. Amar, and F. Family, *Phys. Rev. Lett.* **74** (11), 2066 (1995).

[61] Z. Chen, D. Lu, H. Yuan, P. Han, X. Liu, Y. Li, X. Wang, Y. Lu, and Z. Wang, *J. Cryst. Growth* **235,** 188 (2002).

[62] H. Hirayama, S. Tanaka, and Y. Aoyagi *Microelectronic Engineering* **49**, 287 (1999).

[63] X. Xiao, A. Fischer, G. Wang, P. Lu, D. Koleske, M. Coltrin, J. Wright, S. Liu, I. Brener, G. Subramania, and J. Tsao, *Nano. Lett.* **14** (10), 5515 (2014).

[64] M. Zhang, P. Bhattacharya, and W. Guo, *Appl. Phys. Lett.* **97**, 011103 (2010).

[65] N. Grandjean and J. Massies, *Appl. Phys. Lett.* **72**, 1078 (1998).

[66] S. Dalmasso, B. Damilano, N. Grandjean, J. Massies, M. Leroux, J. L. Reverchon, J. Y. Duboz, *Thin Solid Films,* **380**, 195 (2000).

[67] K. Tachibana, T. Someya, Y. Arakawa, *Appl. Phys. Lett.* **74**, 383 (1999).

[68] F. C. Frank, and J. H. van der Merwe, *Proceedings of Royal Society of London A*, **198**, 205 (1949).

[69] M. Volmer, and A. Weber, *Z. Phys. Chem.*, **119**, 277 (1926).

[70] S. Deshpande, T. Frost, L. Yan, S. Jahangir, A. Hazari, X. Liu, J. Millunchick, Z. Mi, and P. Bhattacharya, *Nano Lett.* **15** (3), 1647 (2015).

[71] P. Bhattacharya, S. Ghosh, and A. Stiff-Roberts, *Annu. Rev. Mater. Res.* **34** (1), (2004).

[72] O. Dehaese, X. Wallart, and F. Mollot, *Appl. Phys. Lett.* **66** (1), 52 (1995).

[73] S. Deshpande, T. Frost, A Hazari, and P. Bhattacharya, *Appl. Phys. Lett.* **105**, 141109, (2014).

[74] Y. Varshni, *Physica*, **34**, 149, (1967).

[75] S. Feng, *et. al. J. Appl. Phys.* **92** (8), 4441 (2002).

[76] K. Ramaiah, *et. al., Appl. Phys. Lett.* **87** (17), 3307 (2004).

[77] Adelmann, C. *et. al., Appl. Phys. Lett.* **76** (12), 1570 (2000).

[78] Gacevic, Z. *et. al. J. Appl. Phys.* **109**, 103501 (2011).

[79] Damilano, B. *et. al. Appl. Phys. Lett.* **75** (24), pp. 3751 (1999).

[81] K. Itaya, H. Sugawara, and G. Hatakoshi, *J. Crys. Growth,* **138**, 768 (1994).

[82] T. Nishida *et. al.* "*Proc. of SPIE*, **7583**, 758303 (2010).

[83] B. Qiu, S. McGougall, D. Yanson, and J. Marsh *Opt. Quanum. Elecon.* **40**, 1149 (2008).

[84] R. Hülsewede, R. *Proc. of SPIE,* **6456**, 645607 (2007).

[85] G. Erbert *IEEE J. of Select. Topic. Quantum. Electron.* **5** (3), 780 (1999).

[86] N. Morris, J. Connolly, R. Martinelli, J. Abeles, and A. Cook, *IEEE Photon. Tech. Lett.* **7** (5), 455 (1995).

[87] A. Hazari, A. Bhattacharya, T. Frost, S. Zhao, M. Z. Baten, Z. Mi, and P.

Bhattacharya, *Opt. Lett.* **40** (14), 3304 (2015).

[88] G. Su, T. Frost, P. Bhattacharya, and J. Dallesasse, *Opt. Express.* **23** (10), 12850 (2015).

[89] Müller, J. *et. al. Appl. Phys. Lett.* **95**, 051104 (2009).

[90] T. Kyono, *et. al. Appl. Phys. Exps.* **3**, 011003 (2010).

[91] J. Wu, *et. al. Appl. Phys. Lett.* **80**, 4741 (2002).

[92] C. Xia, *et. al. Opt. Quantum. Electron.* **38**, 1077 (2006).

[93] B. Hakki, and T. Paoli, *J. Appl. Phys.* **46**, 1299 (1975).

[94] S. Feng, *et. al. J. Appl. Phys.* **92**, (8), 4441 (2002).

[95] K. Ramaiah, *et. al., Appl. Phys. Lett.* **87** (17), 3307 (2004).

[96] C. Adelmann, *Appl. Phys. Lett.* **76** (12) 1570 (2000).

[97] P. Bhattacharya, "Semiconductor Optoelectronic Devices," 2nd ed. Upper Saddle River, NJ: Prentice Hall, chapter 6 (1996).

[98] M. Yonemura, A. Kawasaki, S. Kato, and M. Kagami, *Opt. Lett.* **30** (17), 2206 (2005).

[99] E. Mester, A. F. Mester, and A. Mester, *Las. Surg. Med.* **5**, 31 (1985).

[100] M. Jansen, G. P. Carey, R. Carico, R. Dato, A. M. Earman, M. J. Finander, G. Giaretta, S. Hallstein, H. Hofler, C. P. Kocot, S. Lim, J. Krueger, A. Mooradian, G. Niven, Y. Okuno, F. G. Patterson, A. Tandon, and A. Umbrasas, *Proc. of SPIE,* **6489**, 648908 (2007).

[101] A. Doshi, S. Y. Cheng, M. Trivedi, *System. Man. and Cybernet.* **39** (1), 85 (2009).

[102] S. Cheng, A. Doshi, and M. Trivedi, *Int. Vehicles. Symposium*, 589 (2007).

[103] W. D. Jones, *IEEE Spectrum* **39** (1), 82 (2002).

[104] H. Yamada (2013)

[105] S. Nakamura, M. Senoh, S.-I. Nagahama, N. Iwasa, T. Yamada, T. Matsushita, H. Kiyoku, Y. Sugimoto, T. Kozaki, H. Umemoto, M. Sano, and K. Chocho, *Appl. Phys. Lett.* **72**, 2014 (1998).

[106] G. Su, T. Frost, P. Bhattacharya, J. Dallesasse, and S. Chuang, *Opt. Express* **22** (19), 22716 (2014).

[107] U. Mishra, and J. Singh, "Semiconductor Device Physics and Design," Springer (2009).

[108] D. Volm, *et. al*. *Phys. Rev. B.* **53**, 16543 (1996).

[109] W. Gotz, N. M. Johnson, J. Walker, D. P. Bour, and R. A. Street, *Appl. Phys. Lett.* **68**, 667 (1996).

[110] P. Kozodoy, H. Xing, S. P. DenBaars, U. K. Mishra, A. Saxler, R. Perrin, S. Elhamri, and W. C. Mitchel, *J. Appl. Phys.* **87**, 1832 (2000).

[111] I. Akasaki, H. Amano, M. Kito, and K. Hiramatsu, *J. Luminescence* **48-49**, 666 (1991).

[112] J. Neugebauer, and C. G. Van de Walle, *Phys. Rev. B* **50**, 8067(R) (1994).

[113] C. G. Van de Walle, *Phys. Rev. B* **56**, R10020(R) (1997).

[114] M. A. Kahn, J. N. Kuznia, J. M. Van Hove, D. T. Olson, S. Krishnankutty, and R. M. Kolbas, *Appl. Phys. Lett.* **58**, 526 (1991).

[115] M. G. Ganchenkova and R. M. Nieminen, *Phys. Rev. Lett.* **96**, 196402 (2006).

[116] M. Kahn, M. Shur, and Q. Chen, *Appl. Phys. Lett.* **68**, 3022 (1996).

[117] Z. Fan, S. N. Mohammad, W. Kim, O Aktas, A. E. Botchkarev, and H. Morkoc, *Appl. Phys. Lett.* **68**, 1672 (1996).

[118] Y.-R. Wu, Y.-Y. Lin, H.-H. Huang, and J. Singh, *J. Appl. Phys.* **105**, 013117 (2009).

[119] W.-G, Jung, J.-M. Jang, and S.-K. Choi, and J.-Y. Kim, *Phys. Stat. Solidi C* **6**(4), 797 (2009).

[120] G. Kamler, J.L. Weyher, I. Grzegory, E. Jezierska, T. Wosiński, *J. Crys. Growth* **246**, 21-24 (2002).

[121] D. Zhuang, J.H. Edgar, *Materials Science and Engineering* **R48**, 1-46 (2005).

[122] J. L. Weyher, *Cryst. Res. Technol.* **47**(3), 333 – 340 (2012).

[123] A. Banerjee, T. Frost, S. Jahangir, and P. Bhattaharya, *IEEE J. Quantum. Electron.* **50** (4), 228 (2014).

[124] P. Bhattacharya, "Semiconductor Optoelectronic Devices," 2nd ed. Upper Saddle River, NJ: Prentice Hall (1996).

[125] Y. C. Shen, G. Mueller, S. Watanabe, N. F. Gardner, A. Munkholm, and M. R. Krames, *Appl. Phys. Lett.* **91**, 141101 (2007).

[126] M. Zhang, P. Bhattacharya, J. Singh, and J. Hinckley, *Appl. Phys. Lett,* **95**, 201108 (2009).

[127] M. Meneghini, N. Trivellin, G. Meneghesso, and E. Zanoni, *J. Appl. Phys*. **106**, 114508 (2009).

[128] A. Laubsch, M. Sabathil, J. Baur, M. Peter, and B. Hahn, *IEEE Trans Electron Devices* **57**, 79 (2010).

[129] S. L. Chuang, "Physics of Photonic Devices," Wiley (2012).

[130] H. Zhao, R. Arif, Y. Ee, and N. Tansu, Opt. Quant. Electron, **40**, 301 (2008).

[131] W. Scheibenzuber, U. T. Schwarz, L. Sulmoni, J. Dorsaz, J.-F. Carlin, and N. Grandjean, J. Appl. Phys. **109**, 093106 (2011).

[132] N. Kirstaedter, O. G. Schmidt, N. N. Ledentsov, D. Bimberg, V. M. Ustinov, A. Y. Egorov, A. E. Zhukov, M. V. Maximov, P. S. Kop'ev, and Z. I. Alferov, Appl. Phys. Lett. **69**, 1226 (1996).

[133] P. Bhattacharya, and S. Ghosh, Appl. Phys. Lett. **80** (19), 3482 (2002).

[134] A. Meneghini, N. Trivellin, G. Meneghesso, E. Zanoni, U. Zehnder, and B. Hahn, J. Appl. Phys. **106**, 114508 (2009).

[135] A. Laubsch, M. Sabathil, J. Baur, M. Peter, and B. Hahn, IEEE Trans. Electron. Devices, **57** (1), 79 (2010).

[136] S. Ghosh, P. Bhattacharya, E. Stoner, J. Singh, H. Jiang, S. Nuttinck, and J. Laskar, Appl. Phys. Lett. **79**, 722 (2001).

[137] M. Zhang, Thesis, *Growth and Characterization of InGaN/GaN Quantum Well and Quantum Dot Light Emitting Diodes and Lasers*, 2011.

[138] J. Nie, S. A. Chevtchenko, J. Xie, X. Ni, and H. Morkoç, Proc. of SPIE, **6894**, 689424 (2008).

[139] E. Kioupakis, P. Rinke, K. Delaney, and C. Van de Walle, Appl. Phys. Lett. **98**, 161107 (2011).

[140] J. Piprek, *Phys. Stat. Solidi A* **207** (10), 2217 (2010).

[141] A. David and M. J. Grundmann, *Appl. Phys. Lett.* **97**, 033501 (2010).

[142] A. David and M. J. Grundmann, Appl. Phys. Lett. **96**, 103504 (2010).

[143] Denso Global News Release: "http://www.globaldenso.com/en/newsreleases/121019-01.html" (2015).